Tools for Improving and Understanding Transcranial Magnetic Stimulation

A DISSERTATION SUBMITTED TO THE FACULTY OF
UNIVERSITY OF MINNESOTA
BY

Seyedsina Shirinpour

IN PARTIAL FULFILLMENT OF THE REQUIREMENTS
FOR THE DEGREE OF
DOCTOR OF PHILOSOPHY

Advisor: Alexander Opitz

October 2020

Acknowledgments

First and foremost, I want to thank my advisor, Prof. Alexander Opitz for accepting me as his first student, and his continued support throughout my PhD. I learned a lot about brain stimulation and how to do research under his guidance. I am grateful that he gave me the liberty to explore a range of topics which allowed me to broaden my knowledge and to gain invaluable skills in this journey.

I appreciate my past and present committee members prof. Theoden Netoff, prof. Zhi Yang, prof. Bernadette Gillick, and prof. Donald Simone for keeping me on the right track with their helpful advice and critical feedback.

I also thank our collaborators, prof. Gillian Queisser, prof. Andreas Vlachos, prof. Peter Jedlicka, and their students, James Rosado, Nicholas Hananeia, Christos Galanis who made the multi-scale modeling project in this dissertation possible with their insight and expertise.

Furthermore, my sincere gratitude also goes to my labmates for creating a supportive and fun atmosphere. Dr. Ivan Alekseichuk and Kathleen Mantell who together with me formed the original three musketeers of the lab. Nipun Perera, Dr. Harry Tran, Estefania Cruz, Dr. Miles Wischnewski, and Aidan Dulaney were the later additions who brought further friendship and intellectual stimulation to the group.

Likewise, I want to thank everyone in my former lab, Biomedical Functional Imaging and Neuroengineering Laboratory (BFINL). I express my gratitude to Prof. Bin He who mentored me and made me interested in neural engineering. I appreciate my dear friends in the “pain group”, Michelle Case, and Vishal Vijayakumar for all their support and advice in my research. I’m also grateful to Abbas Sohrabpour for his unconditional guidance, and the rest of the group members, Dr. Bryan Baxter, Dr. Long Yu, Dr. Abhrajeet Roy, Dr. Nessa Johnson,

Dr. Seyed Amirhossein Hosseini, Shuai Ye, Zhengxiang Cai, Dr. Steve Meng, Dr. Haiteng Jiang, Dr. Brad Edelman, Dr. Chris Cline, Dr. Ting Yang, Dr. Yicun Wang, Daniel Suma, Rachel Niu, Jake Stieger, Colin Smith, John Basil, Chris Coogan, and Dr. Vadim Petruk for their friendship and help.

Additionally, I appreciate the BME department faculty and staff for their academic and administrative support. I specifically want to thank Rachel Jorgenson, and Victor Barocas for continuously advocating for the students and their kindness. Also, many thanks to the National Institute of Health and MnDRIVE for their financial support, enabling years of research.

Last but not least, I am deeply thankful to everyone in my personal life who have been there for me. I am much obliged to my friends in Minnesota, Iran, and the rest of the world who have always been my companions on this voyage. Finally, I am wholeheartedly grateful for my family for paving the road for me and showing love and support all my life.

Unfortunately, I have to be selective here and cannot list many wonderful people who have greatly helped me throughout the years. However, they still have my utmost gratitude.

Abstract

Transcranial magnetic stimulation (TMS) is a non-invasive brain stimulation technique that can modulate brain activity through a time-varying magnetic field which induces an electric field in the brain. TMS has been used extensively in research and clinical applications because of its ability to non-surgically deliver suprathreshold stimulation to the brain in a safe manner. Despite the popularity of TMS, there are still major gaps in our understanding of how TMS modulates brain activity on a fundamental neuroscience level. Therefore, the TMS mechanism of action is still under investigation. Improved stimulation technology and computational tools have promise for bridging this gap in our understanding. In my dissertation, I developed new methodologies and computational models that advance the current state-of-the-art in TMS and can assist researchers in their future investigations. First, I describe a closed-loop TMS system that can deliver the stimulation based on the instantaneous brain state. This allows researchers to investigate the role of the intrinsic neural activity on the brain's responsiveness to TMS. To further provide insights into how TMS modulates brain activity at a large brain-scale and the neuronal level, I developed a multi-scale modeling paradigm. Computational simulations have been used extensively to estimate electric fields induced in the brain by TMS, however, their results still need to be validated. To this end, in the second study here, I utilize analytical solutions to evaluate these numerical simulations. After confirming the accuracy of the electric field models, I

incorporated multi-scale modeling to further investigate how the externally induced electric fields alter the behavior of neurons and their subcellular activity. The subcellular modeling of neurons allows researchers to study the lasting effects of TMS in neurons in a sophisticated multi-scale model for the first time. In summary, the tools developed in my PhD can facilitate answering long-lasting questions about the TMS mechanism of action. This, in turn, will enable developing more effective TMS protocols/equipment which can lead to improved clinical outcomes in the treatment of psychiatric and neurological disorders with TMS.

Table of Contents

List of Tables

List of Figures

List of Abbreviations

ATP	Adenosine Triphosphate
AD	Alzheimer's Disease
ASCII	American Standard Code for Information Interchange
aCSF	artificial Cerebrospinal Fluid
ADHD	Attention Deficit Hyperactivity Disorder
AR	AutoRegressive
Bi-CGSTAB	BiConjugate Gradient Stabilized
CPU	Central Processing Unit
CSF	Cerebrospinal Fluid
CE	Common Era
cTMS	controllable-pulse-parameter TMS
DBS	Deep Brain Stimulation
DLPFC	Dorsolateral Prefrontal Cortex
ETP	Educated Temporal Prediction
ECT	Electroconvulsive Therapy
ECoG	Electrocorticography
EEG	Electroencephalography
EMG	Electromyography
ER	Endoplasmic Reticulum
FFT	Fast Fourier Transform
FEM	Finite Element Method
FIR	Finite Impulse Response
FDA	Food and Drug Administration
fMRI	Functional Magnetic Resonance Imaging
GLME	Generalized Linear Mixed-Effects
HOC	High Order Calculator
iTBS	intermittent Theta Burst Stimulation
iEEG	intracranial Electroencephalography
LSL	Lab Streaming Layer

LTD	Long Term Depression
LTP	Long Term Potentiation
LU	Lower–Upper
MRI	Magnetic Resonance Imaging
MDD	Major Depressive Disorder
MEP	Motor Evoked Potential
NeMo-TMS	Neuron Modeling for TMS
nAChR	nicotinic Acetylcholine Receptor
NIBS	Non-Invasive Brain Stimulation
OCD	Obsessive-Compulsive Disorder
OC	Occipital Cortex
ODE	Ordinary Differential Equation
PM	Plasma Membrane
PMCA	Plasma Membrane Calcium ATPase
NCX	Na^{+}/Ca^{2+} exchanger
PSD	Power Spectral Density
PFC	Prefrontal Cortex
M1	Primary Motor Cortex
RAM	Random Access Memory
rTMS	repetitive Transcranial Magnetic Stimulation
SNR	Signal-to-Noise Ratio
SD	Standard Deviation
SEEG	Stereoelectroencephalography
TBS	Theta Burst Stimulation
TEP	TMS Evoked Potential
tACS	transcranial Alternating Current Stimulation
tDCS	transcranial Direct Current Stimulation
TES	Transcranial Electrical Stimulation
TMS	Transcranial Magnetic Stimulation
TTL	Transistor-Transistor Logic
VDCC	Voltage-Dependent Calcium Channel

Chapter 1: Introduction

"I am a brain, Watson. The rest of me is a mere appendix."

- Arthur Conan Doyle

1.1. Overview

The brain is indeed a magnificent organ. Sensation, motor function, language, emotion, and cognition all come from the brain. The human brain is made up of a staggering number of neurons; estimated close to 100 billion (Azevedo et al., 2009). Neurons are the basic processing units in the brain that receive, integrate, and transmit information electrically in the form of action potentials. When the membrane potential of the neuron reaches a certain threshold, due to the activation of voltage-gated ion channels, the rapid influx of ions generates a strong electrical signal that propagates throughout the cell. When the action potential reaches the axon terminals, the signal is transmitted to other neurons through chemical and electrical junctions called synapses. In humans, each cortical neuron interacts with other neurons by forming thousands of synapses on average (Pakkenberg et al., 2003). Scientists in multiple disciplines have long been fascinated by the brain and have been trying to make sense of this complex organ. To this end, researchers have applied a broad range of methods to study human and animal brains at different scales; from the molecular level, all the way to the system level. We are still at the beginning of the road in untangling this mystery of

the universe—perhaps the most complex one. Nevertheless, we have learned that a remarkable degree of harmony is necessary across the brain for it to function properly. Any pathological deviation from this state can cause neurological or psychiatric disorders.

To address such mental disorders, a spectrum of treatment methods has been utilized throughout history, e.g. medication, brain surgery, and even supernatural rituals. Electrical stimulation is a treatment method that dates back to the early CE when torpedo fish were used to relieve headaches in Rome. About a millennium later, it is reported that Avicenna used shock therapy for the treatment of depression (described as melancholia in original texts) (Zwanzger et al., 2016). Later on, from the 18th to early 20th century, multiple physicians and therapists administered various forms of transcranial electrical stimulation (TES) as a non-conventional treatment method (Kadosh and Elliott, 2013). However, most of these attempts were either unsuccessful or there were serious side effects (e.g. in case of electroconvulsive therapy [ECT]). Later in this century, deep brain stimulation (DBS) was developed by surgically implanting the electrodes in the brain. However, despite its success in treating Parkinson's disease, DBS had limited utilization due to its invasiveness. Therefore, in search of alternative brain stimulation techniques, scientists started experimenting with magnetic stimulation of the brain from the early 20th century. After some technological developments, Anthony Barker and colleagues introduced the first stable transcranial magnetic

stimulation (TMS) system in 1985 (Horvath et al., 2011). In this dissertation, we focus on TMS as a neuromodulation method.

1.2. Transcranial Magnetic Stimulation (TMS)

Non-invasive brain stimulation (NIBS) is a set of non-invasive neuromodulation techniques that have been gaining increasing attention both for research and for clinical applications (Peterchev et al., 2012). Transcranial magnetic stimulation (TMS) is one of the most commonly used NIBS methods that generates a strong, short magnetic field by passing currents through a magnetic coil (Barker et al., 1985). When TMS is applied to the head, the magnetic field passes through the skull, and because the magnetic field is transient, an electric field is induced in the brain, as explained according to Faraday's law. These TMS-induced electric fields in turn stimulate the neurons (Hallett, 2007). Figure 1.1 shows an example of the electric field distribution in the brain under the TMS stimulation of the motor cortex.

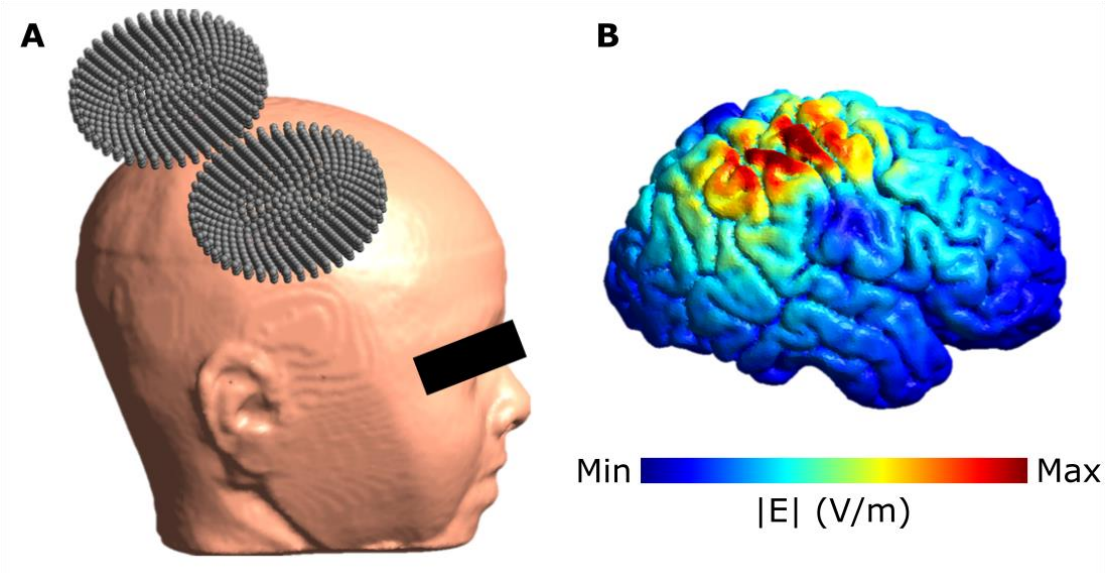

Figure 1.1 Transcranial Magnetic Stimulation. (A) TMS coil placed on top of the motor cortex. **(B)** Spatial distribution of the electric field magnitude induced on the grey matter.

TMS to the motor cortex (M1) can elicit motor evoked potentials (MEP) in the muscles. Such muscle activations can be easily recorded using electromyography (EMG), and therefore used as a direct readout of brain excitability. Since TMS can safely induce suprathreshold activity in the brain with minimal discomfort, it is utilized as a probing tool. Delivering single-pulse TMS has been clinically incorporated to diagnose damage to the motor regions or corticospinal tract, e.g. due to cerebral stroke or motor neuron diseases (Groppa et al., 2012). Furthermore, TMS has been widely used in scientific research to perturb local brain activity as a means to study the causality and functional connectivity in healthy participants and patients (Valero-Cabré et al., 2017). Beyond that, repetitive TMS (rTMS) has been employed for the clinical treatment of psychiatric disorders (Ziemann, 2017). In rTMS protocols, a train of TMS pulses with specific temporal and frequency profiles are delivered to brain regions to induce long-term changes in the brain. Studies suggest rTMS does this by inducing synaptic plasticity involving long-term depression (LTD) and long-term potentiation (LTP) (Hoogendam et al., 2010). Therapeutic rTMS has been commonly used for the treatment of pharmacoresistant Major Depressive Disorder (MDD), (Perera et al., 2016). But, rTMS has also been recently approved by the Food and Drug Administration (FDA) for obsessive-compulsive disorder (OCD), Attention-deficit/hyperactivity disorder (ADHD), and smoking addiction (BrainsWay, 2020;

Commissioner, 2020a, 2020b). Further investigation for rTMS therapy of other psychiatric disorders is currently underway.

Despite the prevalence and practical importance of such brain stimulation methods, there are still major gaps in our understanding of how TMS modulates brain activity at the neuronal level, subcellular level, and at the network level. We know that the external electric fields induced by TMS are responsible for de/hyperpolarizing neurons' membrane potential and therefore affect the neuronal activity (Radman et al., 2009). However, due to the complexity of the brain, there are many open-ended questions such as: Which neurons are activated during TMS and under which conditions? What are the changes in local and large-scale brain networks? What are the long-term effects of (r)TMS? How does (r)TMS induce plasticity, modulate neuron ion channels, and change molecular characteristics of neurons? And how the intrinsic brain state influences the TMS response? Previous studies have tried to tackle these questions using a variety of methods and have greatly broadened our understanding of the TMS field. However, several experimental limitations hinder researchers to answer such fundamental scientific questions. Human experiments are typically limited to non-invasive recordings of the brain, which does not allow direct recording from neurons. Due to ethical reasons, occasional invasive recordings of humans occur only in limited scope among people with underlying neurological pathologies; e.g. Stereoelectroencephalography (SEEG), ECoG (Electrocorticography) or iEEG (intracranial Electroencephalography) for Intracranial Monitoring of seizure

patients. Therefore, invasive studies are mainly limited to animals. However, translating the animal findings to humans is not straightforward and needs careful assessment (Alekseichuk et al., 2019). Furthermore, because of the technological restrictions, current recording devices have a narrow spatio-temporal scope which slows the progress of understanding the TMS mechanism of action. On the other hand, in both animal and human studies, intrinsic brain dynamics are unpredictable. Since the brain state and the local brain connectivity have a major effect on the brain response to TMS (Castrillon et al., 2020; Ozdemir et al., 2020; Pasley et al., 2009; Silvanto and Muggleton, 2008), it complicates making inferences about the TMS mechanism of action. Therefore, despite the significant progress in the field of TMS, further technical developments are necessary to assist researchers in their investigations.

1.3. Summary of Studies

In this dissertation, I will discuss technical developments to address some of the challenges mentioned above.

To address the physiological variability caused by ongoing brain dynamics, I will describe a closed-loop system in chapter 2 and propose a new algorithm that can deliver the TMS based on the state of the brain. This way, the closed-loop approach can potentially reduce the intra-individual variability of TMS responses. From the practical point of view, this method can be used to deliver the TMS at the right time, to induce the maximal response. Furthermore, it allows researchers to

investigate the role of the intrinsic neural activity on the brain's responsiveness to TMS.

Then, to further provide insights into how TMS modulates brain activity on the macro-scale and the neuronal level, I incorporate numerical modeling paradigms. Numerical simulations of electric fields induced by TMS have been extensively used in the field to study the TMS mechanism and for targeting of brain regions. However, despite their success, they still need to be properly validated. Motivated by this need, in chapter 3 of this dissertation, I discuss the derivation of analytical solutions to confirm the numerical simulations of electric fields induced by TMS.

After confirming the accuracy of the models, I extend the electric field simulations to microscopic scales in chapter 4. For this, I incorporate multi-scale modeling to further investigate how the externally induced electric fields alter the behavior of neurons and their subcellular activity. Here, morphologically realistic neurons are solved numerically using the cable equations with proper biophysics to simulate the membrane voltage of the neuron across time under the TMS-induced electric fields. Then, based on these voltage traces, calcium diffusion equations are solved to calculate the calcium concentrations induced by voltage-dependent calcium channels.

Finally, in chapter 5 of this dissertation, I make conclusions about the abovementioned studies and discuss the application of these technical developments for fundamental research and in the clinical domain.

Chapter 2: Real-Time Closed-Loop EEG Phase-Specific Transcranial Magnetic Stimulation

> "Things are going round and round in my head--or maybe my head is going round and round in things."
>
> - Diana Wynne Jones

2.1. Introduction

Large-scale brain activity undergoes ongoing cyclical changes resulting from neural activity interaction of cellular and circuit properties (Buzsáki and Draguhn, 2004). These neural oscillations represent rhythmic alternations between high and low excitability brain states (Schroeder and Lakatos, 2009). Electroencephalography (EEG) enables us to noninvasively record these brain oscillations, which are capturing the synchronous activity of neural ensembles (Buzsáki et al., 2012). The instantaneous phase of brain oscillations is an important feature of neural processing (Alekseichuk et al., 2016; Jacobs et al., 2007; Maris et al., 2016; Sauseng and Klimesch, 2008; Thut et al., 2012). Thus, it can serve as an indicator of brain excitability to inform the timing of brain stimulation delivery such as Transcranial Magnetic Stimulation (TMS).

TMS is a non-invasive brain stimulation method that induces strong short-lasting electric fields in the brain (Barker et al., 1985). A TMS pulse is generated by passing a high-intensity electrical current through an inductive coil to create a magnetic field that penetrates the skull and induces a secondary electric field in the brain, which modulates neural activity (Hallett, 2007; Opitz et al., 2011). TMS is being increasingly explored as a tool to modulate brain activity for the treatment of neurological and psychiatric disorders (Lefaucheur et al., 2014). The combination of TMS with EEG can improve stimulation protocols by tailoring them to the individual's ongoing brain state (Bergmann et al., 2016; Thut et al., 2017).

Numerous studies have assessed the relationship between ongoing EEG oscillations and physiological responses to TMS. For instance, (Romei et al., 2008) reported that for the same TMS stimuli, phosphene induction is increased for lower prestimulus alpha power in posterior brain regions. (Dugué et al., 2011) found a higher probability of TMS-induced phosphenes during the peaks of occipital alpha oscillations. Reports on whether EEG power and/or phase are relevant markers of corticospinal excitability for TMS motor evoked potentials (MEPs) are mixed in the literature e.g. (Berger et al., 2014; Hussain et al., 2019; Keil et al., 2013; Schulz et al., 2014). However, the inferences to be drawn from these studies are limited, as they employed a *post hoc* analysis of EEG data, thus, not allowing a direct causal test of current EEG brain states on TMS responses.

Real-time EEG-TMS methods that deliver stimulation based on the present brain state have the potential to overcome the limitations of previous EEG-TMS studies.

Further, they can potentially deliver more efficient brain stimulation and improve research and clinical outcomes (Karabanov et al., 2016; Polanía et al., 2018; Zrenner et al., 2016). Recent implementations of such real-time EEG-TMS systems delivered TMS based on the phase and power of the EEG mu-rhythm to study MEP corticomotor excitability (Madsen et al., 2019; Zrenner et al., 2018). Further, alpha-synchronized TMS over the dorsolateral prefrontal cortex (DLPFC) has been investigated for depression treatment (Zrenner et al., 2019).

While real-time approaches are a promising technology, they come with a set of technical challenges. In particular, it is difficult to extract the instantaneous phase of the recorded EEG signals accurately in real-time. One main problem of any real-time processing system compared to offline methods is the trade-off between speed and accuracy. Since the data needs to be processed within a limited time window, algorithms have to be computationally fast, even at the cost of accuracy. Another problem is that during real-time computations, we are limited by causality in signal processing, which means that future signal samples are not available for processing such as filtering. In signal processing, band-pass filters extract the frequency bands of interest (e.g. alpha, beta). These filters invariably introduce artifacts around the edges of the available time-series. Since only data recorded up until the current time point are available, filtering inevitably distorts the data and its phase at the current moment. Thus, it is necessary to predict the signal and phase based on the currently available undistorted data from the near past, which can also compensate for any hardware delays.

Multiple methods have been proposed for EEG forward prediction. Since continuous EEG signals to a certain degree are nonsinusoidal and nonstationary (Cole and Voytek, 2017; Mäkinen et al., 2005), this is a challenging problem. Two main methods have been suggested for real-time phase-dependent EEG-TMS: 1) Forward prediction in the time domain. Here, the algorithm uses temporal patterns in a short time window (e.g. the last 0.5 seconds of recorded data) in a frequency band of interest to predict the signal waveform for future time periods. One particular implementation is the autoregression model-based prediction (Chen et al., 2013). 2) Forward prediction in the frequency domain. Here, the signal is projected into the Fourier domain to capture the main sinusoidal (Mansouri et al., 2017) or wavelet component (Madsen et al., 2019) to be used for phase extrapolation.

While these methods have been successfully implemented for real-time phase prediction, they have certain drawbacks. Commonly used autoregressive (AR) predictions in the temporal domain need careful parameter optimizations, have high computational demand, and need high signal power in the frequency band of interest which can lead to the exclusion of participants (Zrenner et al., 2018). Frequency-domain algorithms, like in (Mansouri et al., 2017) are computationally effective and relatively parameter-free, but their accuracy relies on the periodicity and harmonicity of the brain signal.

To overcome existing accuracy-complexity trade-offs, we propose a third, conceptually independent method that is parameter-free, fast, and provides a

similar or higher accuracy compared to the existing methods. This algorithm, named Educated Temporal Prediction (ETP), leverages a short training session before the real-time application to learn each individual's statistical features of the target brain oscillation. Unlike the first two methods that only use data in the current time window for forward prediction, ETP utilizes pre-learned features for faster or more accurate predictions. Since this algorithm is trained on more data (~minutes) than it has access to during real-time processing (~1 second), it can be more robust to compensate for occasional reductions in signal quality. In our current implementation, the ETP algorithm relies on a basic statistical characteristic of phasic data – the central moment of the inter-peak intervals in the time domain. The goal of this study is to compare all algorithms using *in silico* and *in vivo* real-time implementations.

2.2. Material and Methods

2.2.1. Phase Prediction Algorithms

Several different classes of algorithms to detect and predict the EEG phase for TMS closed-loop stimulation have been proposed in the literature. Below we summarize the key principles for (a) Fast Fourier Transform (FFT) based prediction, (b) Autoregressive (AR) forecasting, and (c) newly suggested Educated Temporal Prediction (ETP).

Fast Fourier Transform (FFT) Prediction. The key feature of this algorithm is to use the frequency domain of the EEG signal for forward prediction e.g. (Mansouri

et al., 2017). The specific implementation in our experiment (Figure 2.1A) is as follows: 1) The Laplacian montage for the desired brain region is applied to the signal (Hjorth, 1980) (Figure 2.1E). 2) The signal is zero-phase FIR (Finite Impulse Response) filtered in the frequency band of interest (Alpha: 8-13 Hz, Beta: 14-30 Hz) using the Fieldtrip toolbox (Oostenveld et al., 2010). 3) The FFT of the signal is calculated. 4) The dominant oscillation (maximum amplitude in the frequency spectrum) is detected. 5) The phase of the signal at the dominant frequency is calculated from the angular component of the complex FFT signal. 6) A sine wave of the dominant oscillation with given frequency and phase as calculated in the previous steps is used for forward prediction.

AutoRegressive (AR) Prediction. In this method, the signal is predicted in the time domain. A detailed description can be found in (Zrenner et al., 2018; Chen et al., 2013). In our implementation we perform the following steps (Figure 2.1B): 1) The Laplacian of the electrodes corresponding to the region of interest is calculated. 2) The signal is zero-phase band-pass filtered in the frequency band of interest using an FIR filter. 3) The edges of the signal are trimmed to remove edge artifacts due to filtering. 4) The remaining signal is used to calculate the coefficients for the autoregressive model. 5) Using the AR coefficients, the signal is iteratively forward predicted. 6) The instantaneous phase of the predicted signal is calculated using the Hilbert transform.

Educated Temporal Prediction (ETP). In this method, we propose to include a short training phase to learn the individual statistical properties of the oscillation of

interest. We use a simple and robust method to extract inter-peak intervals and their central moment. Assuming that brain oscillations are quasi-stable over the short measurement periods, one can determine the typical interval between subsequent signal peaks (corresponding to 360° in phase). To predict the time point at which the next target phase, i.e. the peak, will occur, one can add the period between signal peaks to the time of the last peak in the current recorded signal window. Here, we have implemented this algorithm as shown in Figure 2.1C-D: 1) Three minutes of resting-state data is recorded. 2) The Laplacian montage for the region of interest is applied. 3) The data is filtered with a zero-phase FIR filter in the band of interest. This signal is used as the ground truth for later steps. 4) Signal peaks in the first 90 seconds of the training data (learning phase) are identified (T_n). To ensure that found peaks are meaningful and not a result of noise, a criterion of minimum peak distance (i.e. 62.5 ms for alpha oscillations) was introduced. 5) The median of the periods between those peaks was chosen as the interpeak interval (T) to be used for peak prediction. 6) The second 90 seconds of raw resting EEG data are used for the estimation of the accuracy of the phase prediction (validation phase). For this, 250 overlapping windows with a length of 500 ms are selected. 7) The Laplacian montage of the region of interest is applied and the windows are individually filtered in the band of interest using a non-causal sinc filter (brick-wall filter in the Fieldtrip toolbox). 8) The edge (40 ms for alpha) from the end of the window is removed to avoid the edge artifact caused by the filter. 9) The peaks in this window with the criteria

explained in step 4 are detected. 10) The timing of the next peak is predicted by adding T to the last detected peak. 11) The actual phases of the signal at the predicted peaks are measured from the Hilbert transform of the ground truth. 12) In an ideal case, the actual phase of all the predicted peaks should have no deviation from the target phase. However, due to the presence of noise, the achieved phase values may differ. To minimize the potential error in the phase detection, the value of T is increased or decreased incrementally to achieve a zero-mean deviation from the target phase. The adjusted value (T_{adj}) is used for real-time phase estimation. In other words, the bias in phase detection is removed without a change in variance. The calculated phases in this section can also be used as an estimation of the algorithm accuracy in real-time performance. In the real-time segment of the experiment, using T_{adj}, steps 7-10 described above are applied to the current window to predict the next peak (Figure 2.1D). If stimulation at any other phase is desired, we can progress the phase of the signal linearly and calculate the time projection needed from the last peak according to equation (2.1):

$$\boldsymbol{T_{adj*} = \frac{\theta}{2\pi} T_{adj}} \quad \textbf{(2.1)}$$

Where T_{adj*} is the new value of T to be added to the last detected peak in the time window, θ is the target phase for the stimulation.

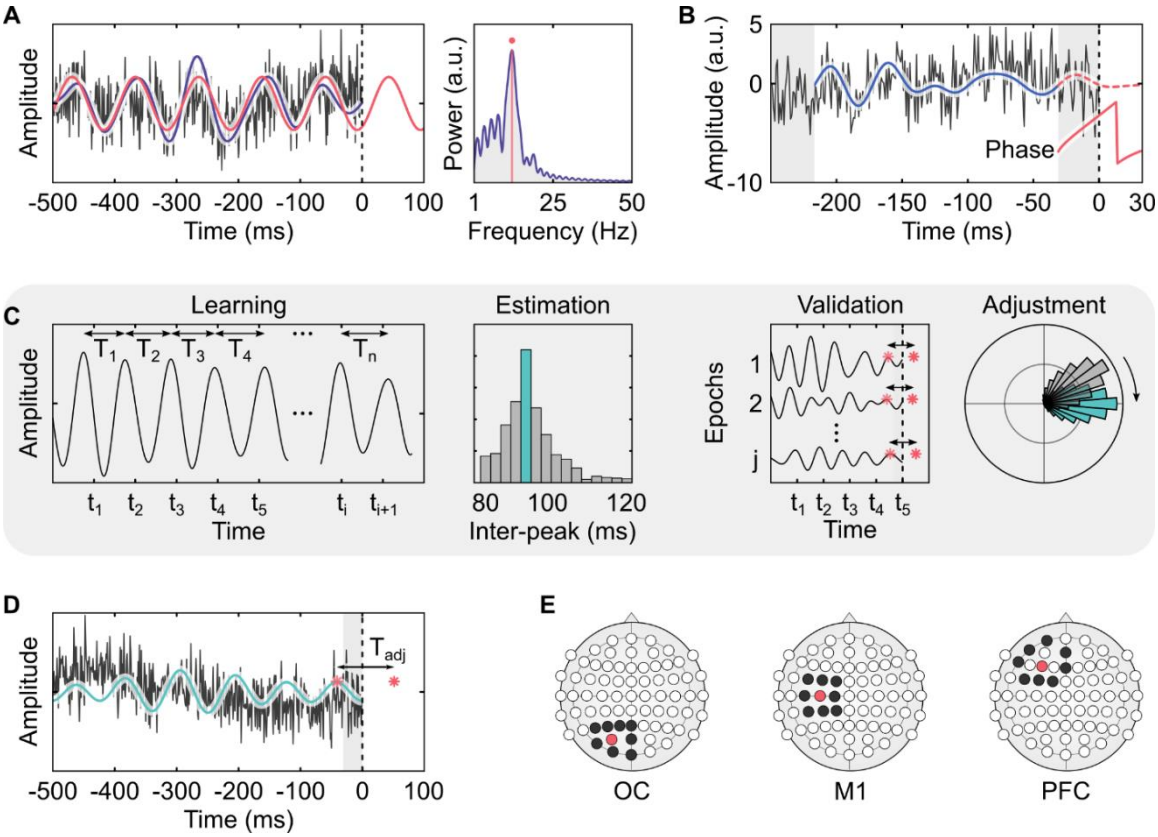

Figure 2.1 Closed-loop algorithm implementation. (A) FFT algorithm. Left panel: The raw data (black) is band-pass filtered (purple). Right panel: the filtered data is Fourier transformed (purple), the frequency and phase of the dominant frequency are calculated (red). A sine wave with the calculated frequency and phase is used for forward prediction (red, left panel). **(B)** AR algorithm. The raw data (black) is band-pass filtered (blue). Signal edges on both sides are removed (gray). The autoregressive model is estimated, and the signal is predicted (dotted red). The phase of the predicted signal is calculated using the Hilbert transform (Solid red). **(C)** ETP training. During the learning phase, the first half of the resting state data is band-pass filtered and the distances between peaks are calculated. The median of the peak periods is calculated as the initial interpeak interval *T*. The second half of the resting-state data is used for the validation phase, the data is segmented into smaller epochs and the peaks are forward projected using *T*. The predicted peaks are compared with the ground truth. Then, *T* is fine-tuned for optimal performance (T_{adj}) **(D)** ETP Real-time application. The raw data (black) is band-pass filtered (green). The edge at the end of the data is removed (gray). The last peak in the time window is projected in the future using T_{adj}. **(E)** Laplacian montages used for the regions of interest. The red electrode is the central electrode. The mean of the surrounding electrodes (black) is removed from the central electrode.

2.2.2. *In Silico* Validation Based on Prerecorded Resting-State EEG

Algorithm Development and Parameter Optimization. We used a separate prerecorded resting-state EEG dataset for the development and initial optimization of the algorithms. For this, data from 25 individuals (13 female) with an average age of 19 years were taken from the Child Mind Institute healthy brain network dataset (Alexander et al., 2017). Phase detection was simulated on segments of resting EEG data which acted as surrogates of the real-time data. In the development process, we optimized parameters such as filter type, filter order, number of samples for edge removal, peak detection. Priority was given to algorithm performance (i.e. phase accuracy) as long as the process was fast enough to run in real-time. In case the performance of two procedures was equivalent, the faster one was chosen.

Algorithm validation. After development, we used another dataset to estimate the accuracy and speed of each algorithm to ensure the generalizability of the results. This dataset included resting-state EEG from 13 healthy adults sampled at 1 kHz with a high number of electrodes (Sockeel et al., 2016). Each individual's data was epoched with a 500 ms window length and a 50% overlap. We used the three algorithms, FFT, AR, and ETP, to predict the phase over three brain regions: left prefrontal cortex (PFC), left motor cortex (M1), and left occipital cortex (OC). These predicted values were compared to the ground truth (continuous EEG data with a two-pass high-order FIR filter and Hilbert transformed to extract phase) to

measure the performance. The computation time needed for each algorithm to process the data was also recorded for each epoch.

2.2.3. *In Vivo* Real-Time Experiments

System Validation. In order to technically validate the closed-loop system, including hardware and software, we created a test scenario using a dummy head model made of a plastic frame and soft fabric soaked with the saline solution and a known electrical input signal (alternating current at 10 Hz) generated with the XCSITE 100 amplifier (Pulvinar Neuro, Chapel Hill, North Carolina, US). Since the signals recorded by all EEG electrodes are perfect oscillations (within technical limits) with a high signal-to-noise ratio (SNR), we expected to detect the phase correctly using all algorithms and confirmed this in the technical test (refer to Figure A.1 for results).

Human Participants Testing. The study protocol was approved by the Institutional Review Board of the University of Minnesota. All volunteers gave written informed consent prior to participation. Eight healthy participants (three female, average age = 27) without a history of neurological disorders took part in the main experiment, where we targeted the alpha oscillations. In one participant, due to a high level of noise during the measurement, the recordings of the motor region for all the methods were removed. In the main experiment, we targeted the alpha band (8 - 13 Hz). To test whether the algorithms can perform well in a different frequency band, four participants (two females) were called back to test

the beta band condition. For this test, we changed the band-pass filter frequency to (14-30 Hz), while keeping all the other parameters the same.

Experimental Protocol. The volunteers were asked to sit in a comfortable chair in a relaxed position throughout the experiment. The participants were instructed to maintain a resting state with eyes open during the recordings. The experimental paradigm is illustrated in Figure 2.2. Five minutes of resting-state were recorded at the beginning and the end of the session. We tested the three algorithms to predict the EEG alpha phase over three brain regions (left PFC, left M1, left OC) in a total of nine blocks, of five minutes each. The order of regions and the order of algorithms within each region was randomized. For the ETP method, there was a separate training block in which three minutes of resting-state data were recorded immediately prior to the real-time block.

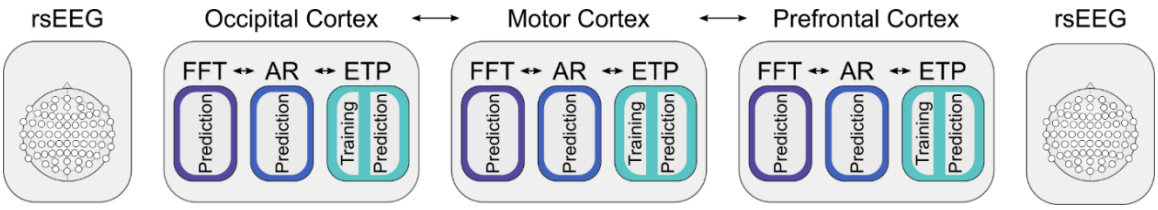

Figure 2.2 Experimental Protocol. Resting-state EEG is recorded at the beginning and end of the experiments. For each three brain regions that are randomized in order, three algorithms are tested in real-time. Before the real-time ETP block, the resting state is recorded, and the algorithm is trained.

Electrophysiological Recordings. Scalp EEG was recorded using a 64-channel EEG amplifier (actiCHamp, Brain Products GmbH, Germany) with active Ag/AgCl electrodes (actiCAP slim, Brain Products GmbH, Germany). The data were

recorded at a sampling rate of 10 kHz with 24 bits resolution. The impedance between the scalp and each electrode was kept below 20 kΩ.

Since we are interested in recording the signal coming from a local brain region, we used the Laplacian montage that subtracts the mean values of the surrounding electrodes from the electrode of interest. This allows for common-mode rejection of signals coming from sources outside of the region of interest. Figure 2.1E illustrates the exact montages that were used for this study.

Real-time Digital Signal Processing. EEG data from the amplifier was streamed to the processing computer (Microsoft Windows 10, 4 cores 3.60 GHz CPU, 16 GB RAM) using the Lab Streaming Layer (LSL, https://github.com/sccn/labstreaminglayer) software in real-time. Custom scripts (https://github.umn.edu/OpitzLab/CL-phase) were used in MATLAB R2017b to receive and process the EEG data and send the triggers to the TMS machine (Magstim Rapid^2, UK). The last 500 ms of the streamed data was selected and fed to the algorithms to perform the phase estimation and prediction. The 500 ms window was updated upon receiving each new sample. In order to perform accurate real-time analysis, it is essential to process the current window of data before the next sample is received. This ensures that the system runs smoothly and sustains real-time performance during the whole session. Thus, the streaming data were downsampled before performing the analysis on each window. Since the ETP and FFT methods are computationally fast, we downsampled the EEG data to 1 kHz. For the AR algorithm, due to high computational demand and

consistency with previous work (Zrenner et al., 2018), the data were downsampled to 500 Hz.

Real-Time Stimulation Triggers. During the real-time phase estimation, a TTL (Transistor-transistor logic) pulse was sent from the parallel port of the computer to trigger the TMS machine. Due to an overall processing delay (~1-2 ms) and a lag of the TMS machine to deliver the magnetic pulse from the time it receives the trigger, there is a total trigger delay one needs to account for. Since this delay is stable over time, it was experimentally measured during the system validation and adjusted in the code. Note that the total delay is system-specific and should be measured for each system separately. In our experiments, triggers were sent when the estimated phase approached the proximity of the desired phase adjusted with the technical delay. Since TMS pulses are very strong compared to the EEG signals, they cause large artifacts that would distort the phase estimation to determine the ground truth in offline processing (Ilmoniemi and Kičić, 2009; Herring et al., 2015). Therefore, in this study, since we are mainly interested in comparing the accuracy of different methods, we did not apply a TMS pulse and only recorded the time at which the triggers were sent. This way, the EEG signal was not distorted, allowing us to estimate the ground truth phase for algorithm comparison.

2.2.4. Data Analysis and Statistics

Algorithm Performance. We quantified the performance of each algorithm calculating its bias, variance, and accuracy. Bias shows the typical difference in the outcome from the target. Here, we used the average difference between the

estimated phase and the target phase. Variance quantifies how spread the outcome distribution is. We used the standard deviation to report to quantify the spread. We defined the accuracy in equation (2.2):

$$Accuracy = 1 - \frac{1}{N \times 180} \sum_{i=1}^{N} |\theta_i - \theta_0| \quad (2.2)$$

Where N is the number of trials for which the phase is estimated, θ_i is the estimated phase (°) for the trial i, and θ_0 (°) is the desired phase. Accuracy of 1 means that the phase has been estimated precisely all the time. Accuracy of 0.5 is a uniformly random phase estimation. Accuracy of 0 means that all phases have been detected as the opposite of the target phase (e.g. troughs instead of peaks).

Statistical Comparison Between the Algorithms. To test whether there is a statistical difference between the algorithm performance, we used a general linear mixed-effects model (GLME) with accuracy as the dependent variable, algorithm type as the fixed effect, and brain region as the random effect variables. In case the result of GLME was significant, we used the Wilcoxon signed-rank test to compare each pair of algorithms.

Signal-to-Noise Ratio (SNR) Measurements and Accuracy Regression. One key factor for closed-loop performance is the signal-to-noise ratio in EEG recordings. Especially the presence or absence of a prominent alpha rhythm has been used as participant selection criteria in previous studies (Zrenner et al., 2018). We hypothesized that phase estimation accuracy will depend on data quality and alpha power. To test this, we calculated the SNR for each experimental

EEG block during post-processing. SNR was measured by calculating the Power Spectral Density (PSD) using Welch's method with 2s epochs and Hamming windows and then dividing the total power in the alpha band by the total power over all frequencies (1-45 Hz). To quantify this relationship, we calculated the linear regression model between the SNR and phase accuracy of each experimental block for the three algorithms separately.

Resting-State Analysis. The ETP algorithm expects that EEG oscillations in the band of interest are quasi-stable over the experiment (in our case, approx. 1 h). To test this, we compared the resting-state data recorded pre-experiment with post-experiment data. Resting-state data were preprocessed to remove noise and artifacts (Delorme and Makeig, 2004; Oostenveld et al., 2010). We calculated the PSD and identified the frequency of maximum PSD for each volunteer in pre and post data. We used the Wilcoxon signed-rank test to evaluate any possible systematic shifts in the alpha peak frequency for all the three brain sites throughout the experiment.

2.3. Results

2.3.1. *In Silico* Validation Based on Prerecorded Resting-State EEG

First, we evaluated the performance of each algorithm *in silico*. Figure 2.3A and Figure A.2 show the polar histograms of the difference between the detected phase and the desired phase in the alpha band for FFT, AR, and ETP methods. Qualitatively, all algorithms target zero degrees correctly; however, ETP shows the

least spread, thus, higher in accuracy, while FFT shows the most spread around the target phase. Additionally, a difference in performance accuracy can be seen between brain regions with the occipital cortex showing the highest accuracy followed by M1 and finally PFC (Figure 2.3B). Table 2.1 summarizes the performance metrics (mean, standard deviation, and accuracy) for all algorithms and brain regions. As can be seen, all methods have a negligible bias in phase estimation; however, AR (mean accuracy = 68%) and ETP (71.8%) algorithms manifest lower spreads and therefore higher accuracies compared to the FFT (57.2%) algorithm (by 10.8% and 14.6% higher accuracy, respectively). ETP performs slightly better than AR by 3.8% in terms of accuracy. The general linear mixed-effect model confirms significant differences between the algorithms accuracy ($F(2,114) = 235$, $p < 1e\text{-}40$). Non-parametric pairwise tests indicate a statistically significant difference between the accuracy of each algorithm pairs (AR vs. ETP: $p < 1.e\text{-}6$, AR vs. FFT: $p < 1e\text{-}7$, ETP vs. FFT: $p < 1e\text{-}7$).

Since computation speed is essential for real-time performance, we also report the median computation times for each method in Table 2.1. ETP works significantly faster than the two other methods. FFT and AR perform at a similar speed, although the AR method runs at a lower sampling rate which means it is inherently slower. Note that the computation times are hardware-specific and, in order to ensure that the system can run in real-time, the processing time should be kept below the sampling frequency.

To test how well the algorithms generalize, we additionally performed phase estimation in the beta band. Since beta oscillations are faster, less stationary, and cover a broader frequency band, all algorithms perform worse compared to the alpha band results (Figure 2.4, Figure A.3, and Table A.1). However, the same pattern between the algorithms still holds. ETP (mean accuracy = 64.7%) shows 3.5% higher accuracy than AR (61.2%), and AR is 5.7% more accurate than FFT (55.5%). The results for computation speeds are comparable to that of the alpha band.

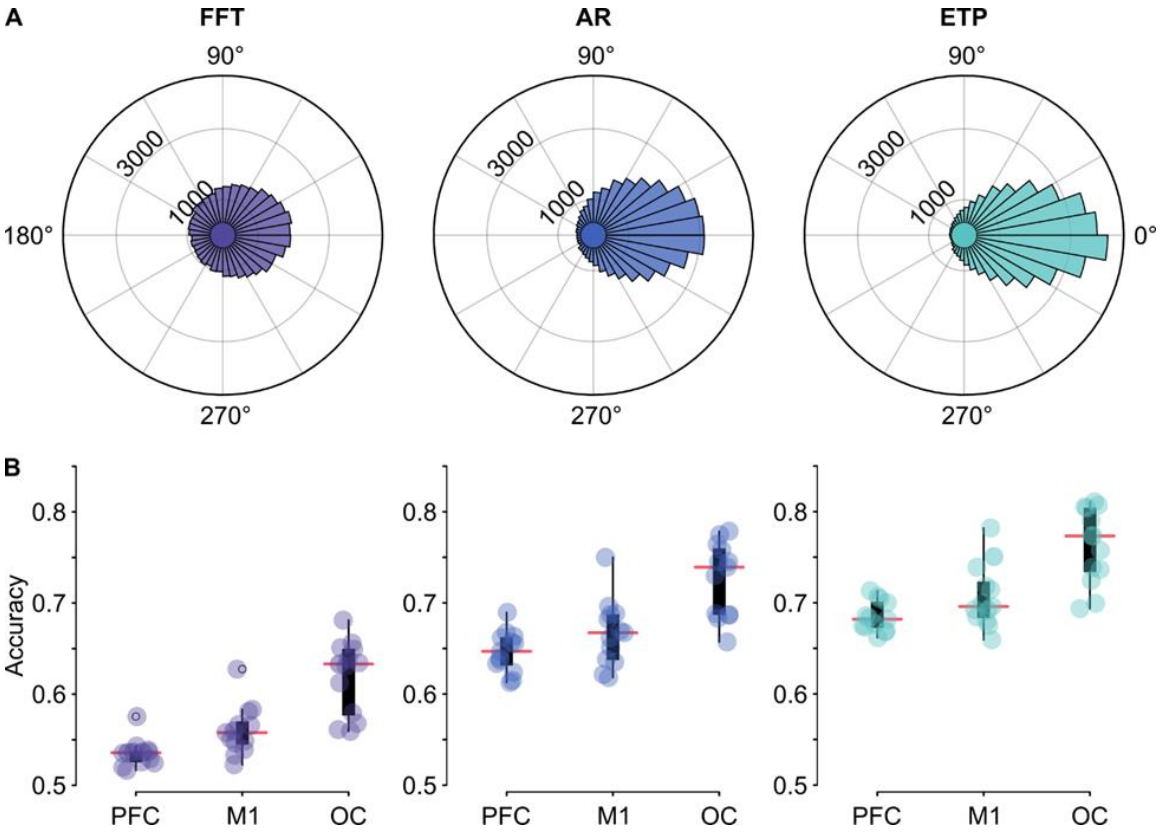

Figure 2.3 Phase estimation results for the *in silico* dataset in the alpha band. (A) Polar histograms of the difference between the estimated phase and ground truth for each algorithm. The phase values are binned into 36 bins. A zero degrees phase would be the ideal outcome since the detected phase matches the desired phase. **(B)** Box plot of the accuracy measurements with the individual datapoints over the three brain sites for each algorithm.

Table 2.1 Alpha band performance and computation times *in silico*

Algorithm	Region	Mean (°)	SD (°)	Accuracy	Median Time (ms)
AR (500 Hz)	All	5.44	73.59	0.68	0.78
	PFC	5.46	79.30	0.65	0.79
	M1	6.37	75.88	0.67	0.81
	OC	4.49	65.59	0.73	0.74
ETP (1000 Hz)	All	0.37	67.35	0.72	0.06
	PFC	0.16	73.54	0.69	0.06
	M1	0.38	69.49	0.71	0.06
	OC	0.56	59.01	0.76	0.06
FFT (1000 Hz)	All	5.55	92.36	0.57	0.82
	PFC	4.91	98.20	0.54	0.82
	M1	5.92	94.33	0.56	0.82
	OC	5.83	84.57	0.62	0.81

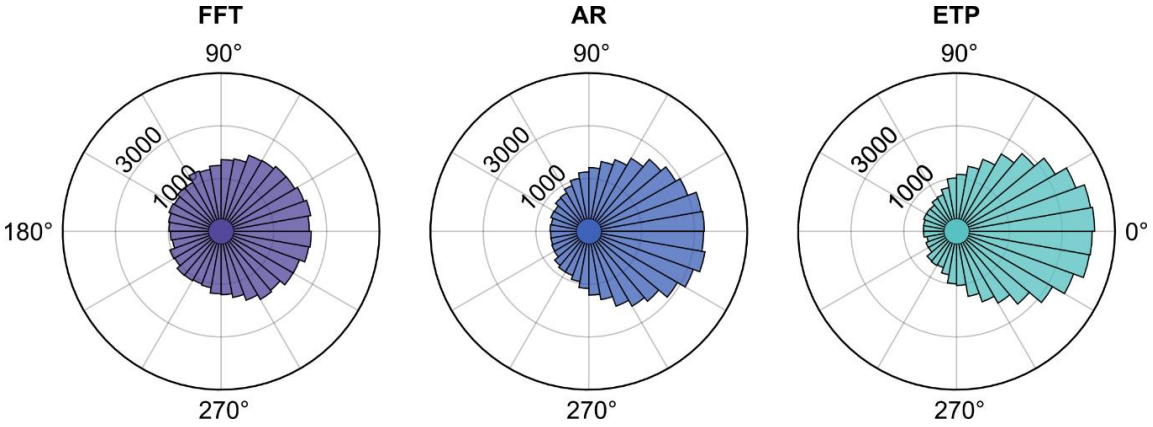

Figure 2.4 Phase estimation results for the *in silico* dataset in the beta band.

2.3.2. *In Vivo* Real-Time Experiments

After comparing the algorithms *in silico* using prerecorded EEG data, we implemented them in the laboratory for true real-time validation. Figure 2.5 shows the laboratory setup we used for this experiment.

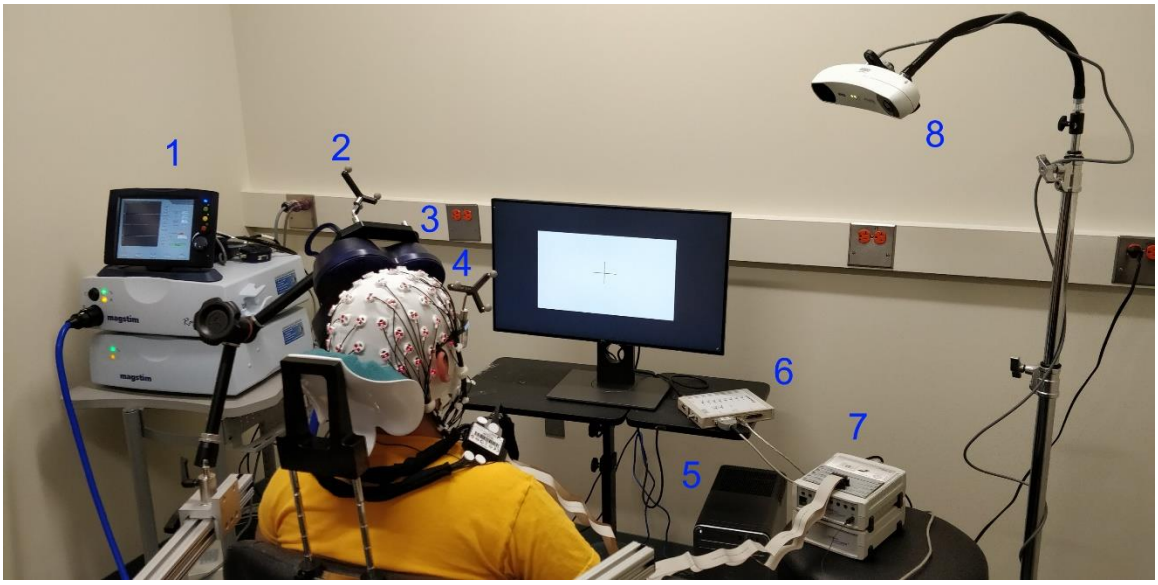

Figure 2.5 Laboratory setup for real-time closed-loop experiment. 1) TMS machine 2) TMS coil tracker 3) TMS coil 4) Participant tracker 5) Processing computer 6) Trigger box 7) EEG amplifier 8) Neuronavigation camera

Similar to the *in silico* validation, for the *in vivo* tests, we targeted the peak (zero phase) of the alpha rhythm. The polar histograms are illustrated in Figure 2.6A and Figure A.4. Figure 2.6B breaks down the accuracy of each algorithm over different regions with box plots. The real-time results further validate the findings reported in the *in silico* results, with ETP (mean accuracy = 70.2%) performing marginally better than AR (66.6%), while ETP and AR perform considerably better than FFT (61.1%). Table 2.2 summarizes the performance metrics of each method in terms of bias, standard deviation, and accuracy for each brain region. As can be seen, ETP shows 3.6% and 9.1% higher accuracy relative to AR and FFT, respectively. Also, AR accuracy is 5.5% higher than FFT. General linear mixed effect model

shows significant differences between the algorithms accuracy ($F(2,66) = 31$, $p < 1e-9$). Non-parametric pairwise tests confirm that there is a statistically significant difference between the accuracy of each algorithm pairs data (AR vs. ETP: $p < 1.e-3$, AR vs. FFT: $p < 1e-4$, ETP vs. FFT: $p < 1e-04$).

We also evaluated a real-time phase estimation in the beta band. The polar histograms for beta phase estimations can be found in Figure 2.7, Figure A.5, and Table A.2. ETP (mean accuracy = 65.4%) performs considerably better in the beta band as opposed to the other methods with 6.7% and 10% higher accuracy than AR (58.7%) and FFT (55.4%), respectively. These results are expected because the FFT method relies on finding the dominant oscillation to predict the signal and the beta band doesn't have such stable narrowband oscillations as the alpha rhythm. For the AR method, optimal parameters such as filter order, edge removal, and autoregressive order are highly dependent on the frequency band of interest. The parameters used here were based on previous research (Zrenner et al., 2018) for the μ-rhythm in the motor cortex and tuned for the frequencies similar to the alpha band. Thus, it is likely that AR will need to be adapted for different frequencies for optimal performance. Our results indicate that ETP, which is a parameter-free method, is readily extendable to different EEG rhythms.

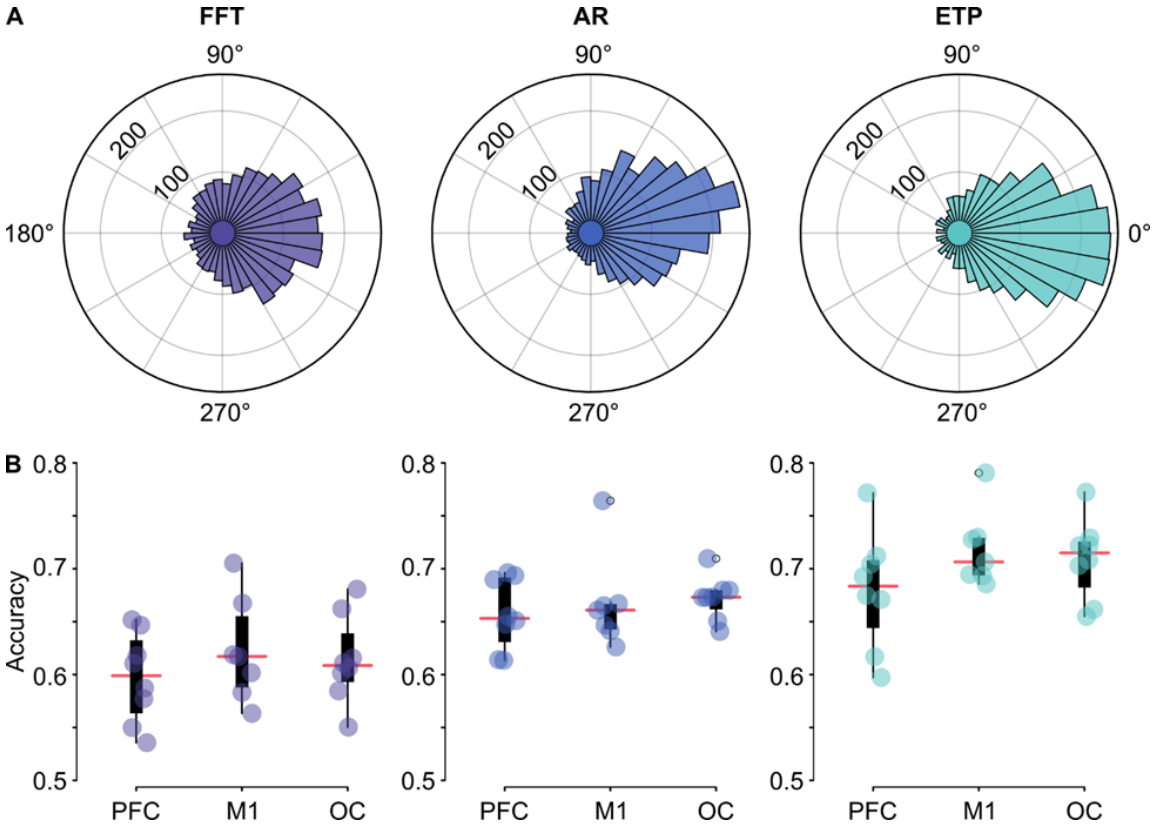

Figure 2.6 Phase estimation results *in vivo* for the alpha band. (A) Polar histograms of the difference between the estimated phase and ground truth for each algorithm. **(B)** Box plot of the accuracy measurements with the individual datapoints over the three brain sites for each algorithm.

Table 2.2 Alpha band performance metrics in the real-time experiment

Algorithm	Region	Mean (°)	SD (°)	Accuracy
AR	All	8.39	76.00	0.67
	PFC	10.66	77.20	0.66
	M1	9.43	75.26	0.67
	OC	5.07	75.54	0.67
ETP	All	0.02	69.87	0.70
	PFC	1.34	73.82	0.68
	M1	-1.10	66.87	0.72
	OC	-0.18	68.91	0.71
FFT	All	1.31	85.63	0.61
	PFC	1.16	87.90	0.60
	M1	-0.47	84.01	0.62
	OC	3.23	84.99	0.61

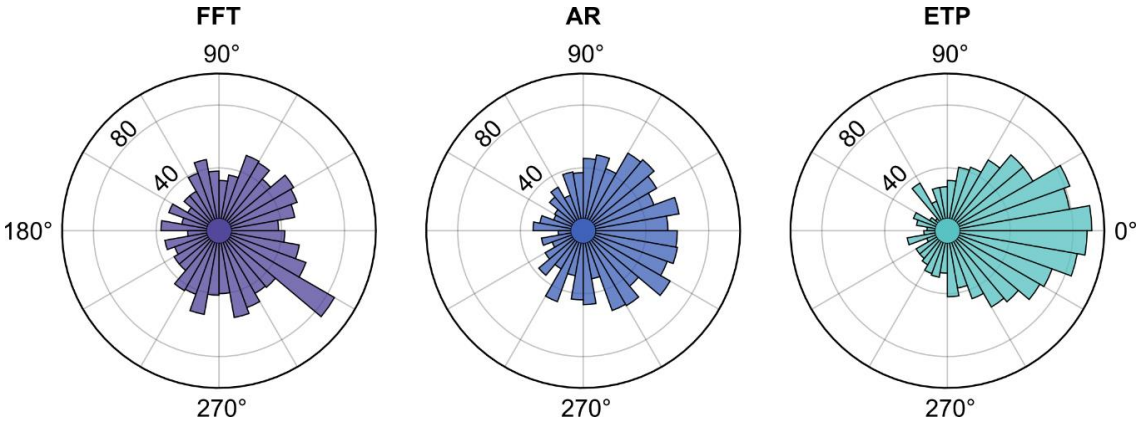

Figure 2.7 Phase estimation results *in vivo* for the beta band.

Signal-to-Noise Ratio (SNR) Measurements and Accuracy Regression. To evaluate the importance of SNR for the phase prediction performance, we applied a linear regression model between the algorithm accuracies and SNR during the

measurement. We defined SNR as the ratio of the alpha power to the total power of the signal. Figure 2.8 illustrates the regression results for each algorithm. In summary, all methods show a statistically significant increase in phase estimation accuracy for higher SNRs (FFT: R^2_{adj} = 0.54, F(21) = 26.3, p < 0.01; AR: R^2_{adj} = 0.41, F(21) = 16.3, p < 0.01; ETP: R^2_{adj} = 0.44, F(21) = 18.4, p < 0.01). The regression slopes are comparable between the methods (0.31 for FFT, 0.28 for AR, and 0.32 for ETP).

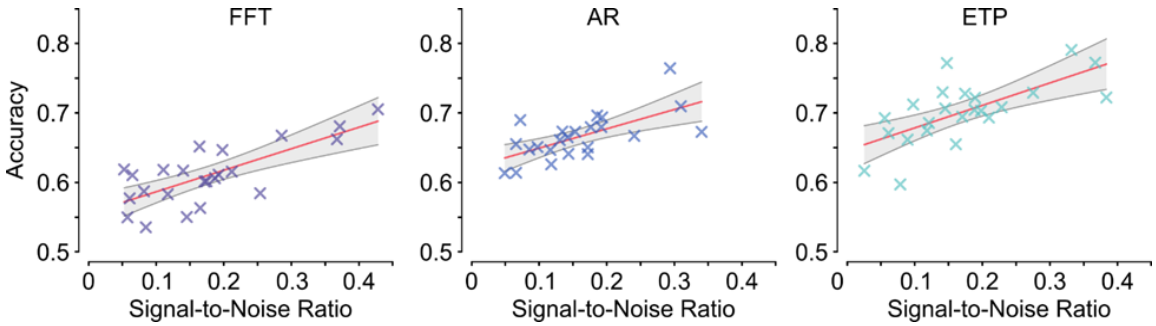

Figure 2.8 Dependence of phase-detection accuracy on the SNR. The linear regression lines are shown in red and the confidence intervals in grey.

Resting-state EEG Analysis. To test whether EEG oscillations are stable throughout the experiment, we compared the frequency of maximum PSD in the alpha band between the pre- and post-experiment resting-state recordings across participants for all three sites using a non-parametric paired test. Figure 2.9 shows the maximum alpha frequency of individuals pre- and post-experiment. We found no systematic differences (Prefrontal region: p-value = 0.53, Motor: p-value = 0.99, Occipital: p-value = 0.58; all degrees of freedom = 22).

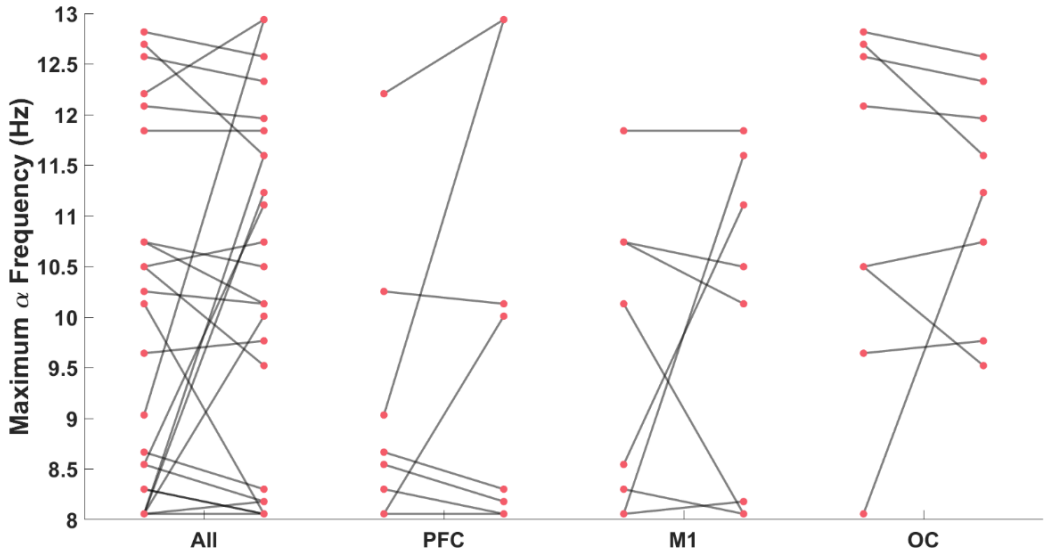

Figure 2.9 Individual's maximum alpha frequency between pre- and post-experiment resting-state EEG over different regions.

2.4. Discussion

Real-time EEG based TMS applications have high potential to develop more precise stimulation protocols tailored to the individual's ongoing brain state. However, optimal technical solutions are still being developed and evaluated. We introduced a new education-based method in which the algorithm learns important features from a short, prerecorded EEG session. We further compared the accuracy of three conceptually distinct algorithms (temporal prediction, frequency domain prediction, and education-based prediction) to target the peaks of the alpha rhythm over three different brain regions. We compared the performance of these algorithms first *in silico* using prerecorded EEG data and second *in vivo* real-time experiments in human participants. We found the FFT method to perform the

least accurately among the three studied algorithms, likely due to reducing the signal to a single-frequency sine wave in the observed time window. Since EEG signals are non-stationary and composed of several frequency components, such simplification can impair forward prediction. Our proposed education-based algorithm (ETP) outperformed the two other methods but was otherwise close in accuracy to the AR method. The performance of the ETP method might be due to the robustness of the algorithm since it learns EEG signal patterns beforehand and doesn't rely only on a short and possibly noisy segment of data that it has access to at the moment of online processing. In addition, we did not exclude any volunteer or data epoch to evaluate performance across a more representative sample. However, as indicated by the found correlation between algorithm accuracy and SNR, higher accuracies could be achieved by excluding participants or time windows with low SNR or oscillatory power.

For real-time applications, computation speed is essential. Hence, we compared the run-time speed of all three algorithms. For a given sampling rate, the AR algorithm is the most computationally demanding. This is due to the heavy calculations needed to compute autoregressive coefficients. On the other hand, because of the simplicity of the ETP method, its computation time is significantly lower than the other two methods. Thus, ETP can run on lower-end hardware and is more accessible to use. Another upside to fast computation time is that it provides more room for future developments in real-time processing. One drawback of using the ETP method is that it needs to be trained on prerecorded

data. However, in our case, three minutes of resting-EEG data were fully sufficient for training, which can be easily integrated into a real-time experiment. Further, the ETP algorithm is computationally robust and does not need to tune several parameters such as the AR method. For example, the order of the autoregressive model used in the AR algorithm is highly dependent on the sampling rate and frequency of interest on each application, and no trivial method for this optimization is available (Krusienski et al., 2006; McFarland and Wolpaw, 2008). For all three algorithms used, filter type and order can strongly affect the performance and careful consideration is essential for their proper optimization along with any algorithm-specific parameters.

Widespread implementation of real-time TMS-EEG has several potential advantages for future research. For example, brain-state dependent EEG-TMS studies can remove the need for *post hoc* analysis since the brain state of interest can be controlled during the experiments. Furthermore, closed-loop systems using neural biomarkers can be investigated in clinical applications to improve brain stimulation treatments. For instance, repetitive TMS (rTMS) to the left DLPFC is widely used for treating medication-resistant major depression (Avery et al., 2006; O'Reardon et al., 2007). Currently, the treatment protocol does not consider the current brain state. However, it is known that EEG oscillations play an important role in major depression which can be utilized for treatment plans (Fingelkurts and Fingelkurts, 2015; Leuchter et al., 2015). Timing TMS to a high-excitability state

might mean that the brain will be more responsive (Zrenner et al., 2019), possibly leading to better treatment outcomes or shorter treatment duration.

Beyond the algorithms evaluated in this study other less common methods to estimate the signal phase exist. (Madsen et al., 2019) used wavelet transforms, which are conceptually similar to the FFT method. Recently, machine learning algorithms have been suggested to estimate the instantaneous phase from unfiltered EEG data (McIntosh and Sajda, 2019). This is similar to the ETP method since it uses prerecorded data to extract features that can inform the real-time application. However, all existing algorithms have room for improvement in accuracy. Due to challenges in implementing real-time phase estimation (such as causality, filtering edge artifact, and system delay), further efforts are needed to improve the performance of such online phase estimation and prediction algorithms. Here, we propose a simple and parameter-free education-based method that only uses easy to access temporal features in the signal (i.e. inter-peak intervals). In the future, more sophisticated algorithms combining temporal, frequency, and spatial features present in resting-state EEG can be developed for more accurate phase prediction in real-time applications. Due to the increasing adoption of brain state-dependent neuromodulation approaches in research and clinical applications, further technical developments can help reach the full potential of this emerging field.

The materials in this chapter are based on the preprint on bioRxiv (Shirinpour et al., 2019)*. The final version of this work is published in the Journal of Neural Engineering* (Shirinpour et al., 2020a)*.*

Chapter 3: Analytical Validation of TMS-Induced Electric Field Models

> "No human investigation can be called real science if it cannot be demonstrated mathematically."
>
> - Leonardo da Vinci

3.1. Introduction

Non-invasive brain stimulation (NIBS) is a promising method to study the causality of brain-behavior relationships in humans as well as for clinical research in neurological and psychiatric disorders (Polanía et al., 2018). Transcranial Magnetic Stimulation (TMS) is one of the most commonly used NIBS methods. TMS affects neural tissue by inducing a short-lasting electric field at sub- or suprathreshold intensities via electromagnetic induction (Valero-Cabré et al., 2017). The induced electric field in the brain is the main actor for TMS effects. However, the electric field is also the most difficult feature to predict as it depends not only on controllable factors, such as current intensity and coil location but also on the individual head anatomy and tissue biophysics (Opitz et al., 2011; Peterchev et al., 2012; Thielscher et al., 2011).

Stimulation-induced electric fields are difficult to directly assess in humans except in cases of intracranial measurements in surgical epilepsy patients. Thus,

modeling approaches are most often used to study NIBS electric field distributions (Miranda et al., 2018). While computational models are clearly useful to guide stimulation protocols and to ensure target engagement (Huang et al., 2017; Opitz et al., 2018, 2016), they still cannot predict the physiological outcome of NIBS studies. This is due to the missing link between the biophysics of stimulation, i.e. electric fields, and the resulting physiological effects. Animal models are crucial to close this knowledge gap because they allow simultaneous measurement of both the biophysics and physiology of NIBS using invasive recordings.

Invasive studies in animal models offer a larger neuroscientific toolset with higher spatial precision than noninvasive evaluations in humans. Thus, animal work is increasingly used to dissect NIBS mechanisms (Kar et al., 2017; Krause et al., 2017; Vöröslakos et al., 2018). However, the translation of results from the animal literature to humans is challenging because it is unclear how to transfer stimulation parameters and dose regimes to achieve comparable conditions. For TMS, the stimulation intensities used are in the same range for the animal (Hoppenrath and Funke, 2013; Mueller et al., 2014; Pasley et al., 2009) and human studies (Rossi et al., 2009). Further, many animal studies use smaller TMS coils, which result in more focal induced electric fields to compensate for the smaller head size (Deng et al., 2013). There is an implicit assumption that the NIBS dose regimens across species are comparable, yet there are limited evidence and a lack of systematic evaluations.

To address some of these issues regarding TMS, we conduct a comparison of electric fields in the brain during TMS with both a 70 or 25 mm figure-8 coil across a range of head sizes. Furthermore, we adopt an analytical approach to confirm the accuracy of the numerical models. This study, therefore, provides a paradigm for translating the invasive animal findings to humans.

3.2. Materials and Methods

3.2.1. General Framework

Since there is no closed-form analytical solution for complex anatomical head models of humans and animals, we incorporated a simplified spherical model to represent the head. Because of the symmetry of the spherical model, it is possible to analytically solve for the electric fields present in the model. First, we derive the equations governing the electric field in the spherical head model. Then, we outline solving the same model using a numerical method. Finally, we compare the analytical and numerical solutions.

3.2.2. Analytical Formulation of TMS-Induced Electric Field

The analytical solution of the TMS-induced electric field follows the method by Eaton derived for a homogeneous spherical volume conductor for an arbitrary TMS coil geometry (Eaton, 1992). Below we summarize the essential equations and their derivation for a single loop figure-8 coil. To simplify the equations, the origin of the spherical coordinate system is set as the center of the model. Time-varying signals have the form $e^{j\omega t}$, where $j = \sqrt{-1}$ and ω is the angular frequency. The

electric field $\boldsymbol{E}$ first depends on the complex vector constant C_{lm} that relates to a given coil geometry and placement:

$$C_{lm} = \oint_{Coil} \frac{Y_{lm}^{*}(\theta', \phi')}{(2l+1){r'}^{l+1}} \boldsymbol{dI'} = C_{lm}^{x}\hat{\mathrm{i}} + C_{lm}^{y}\hat{\mathrm{j}} + C_{lm}^{z}\hat{k} \quad (1)$$

Where * is the complex conjugate; r', θ', ϕ' are radial distance, polar angle, and azimuthal angle of the differential segment of the coil, $Y_{lm}(\theta', \phi')$ are spherical harmonic functions; I is the current in the coil; $\boldsymbol{dI'}$ is the orientation of the current in the coil along the current path. Further, we define D_{lm}, E_{lm}, and F_{lm} to simplify the equations:

$$D_{lm} = \frac{C_{lm}^{x} - jC_{lm}^{y}}{2} \quad (2)$$

$$E_{lm} = \frac{C_{lm}^{x} + jC_{lm}^{y}}{2} \quad (3)$$

$$F_{lm} = \frac{-j\omega\mu_0 I[\sigma_s + j\omega(\varepsilon_s - \varepsilon_0)]}{l(\sigma_s + j\omega\varepsilon_s) + j\omega\varepsilon_0(l+1)}$$

$$\times \left\{ -D_{l-1,m-1}\sqrt{\frac{(l+m-1)(l+m)}{(2l+1)(2l-1)}} + E_{l-1,m+1}\sqrt{\frac{(l-m-1)(l-m)}{(2l+1)(2l-1)}} \right.$$

$$\left. + C_{l-1,m}^{z}\sqrt{\frac{(l-m)(l+m)}{(2l+1)(2l-1)}} \right\} \quad (4)$$

$$For\ l > 0, \qquad F_{00} = 0$$

We assume that the sphere has the permeability of free space μ_0, where ε_s and σ_s are the permittivity and conductivity of the homogenous isotropic sphere, respectively. We used $\varepsilon_s \approx 13000\varepsilon_0$ and $\sigma_s = 0.14\, Sm^{-1}$. Using the equations

above, the electric field at any given point in space (r, θ, ϕ) along three spherical axes is:

$$\boldsymbol{E} \cdot \hat{\boldsymbol{r}} = -\mu_0 I \sum_{l=1}^{N+1} \sum_{m=-l}^{l} \frac{(j\omega)^2 \varepsilon_0 (2l+1)}{j\omega(\varepsilon_s l + \varepsilon_0 l + \varepsilon_0)} r^{l-1} Y_{lm}(\theta, \phi)$$

$$\times \left\{ -D_{l-1,m-1} \sqrt{\frac{(l+m-1)(l+m)}{(2l+1)(2l-1)}} + E_{l-1,m+1} \sqrt{\frac{(l-m-1)(l-m)}{(2l+1)(2l-1)}} \right.$$

$$\left. + C^z_{l-1,m} \sqrt{\frac{(l-m)(l+m)}{(2l+1)(2l-1)}} \right\} \quad (5)$$

$$\boldsymbol{E} \cdot \hat{\boldsymbol{\phi}} = -j\omega\mu_0 I \sum_{l=0}^{N} \sum_{m=-l}^{l} j \times \left(D_{lm} e^{j\phi} - E_{lm} e^{-j\phi} \right) r^l Y_{lm}(\theta, \phi) - \sum_{l=1}^{N+1} \sum_{m=-l}^{l} F_{lm} \frac{jm}{\sin\theta} r^{l-1} Y_{lm}(\theta, \phi) \quad (6)$$

$$\boldsymbol{E} \cdot \hat{\boldsymbol{\theta}} = -j\omega\mu_0 I \sum_{l=0}^{N-1} \sum_{m=-l}^{l} \left\{ -C^z_{l+1,m-1} \times e^{-j\phi} \sqrt{\frac{(l-m+2)(l-m+1)}{(2l+1)(2l+3)}} \right.$$

$$\left. + \sqrt{\frac{(l-m+1)(l+m+1)}{(2l+1)(2l+3)}} \times \left[D_{l+1,m} e^{j\phi} + E_{l+1,m} e^{-j\phi} \right] \right\} r^{l+1} Y_{lm}(\theta, \phi)$$

$$- \sum_{l=1}^{N+1} \sum_{m=-l}^{l} \left\{ j\omega\mu_0 I \left[C^z_{l-1,m-1} e^{-j\phi} \sqrt{\frac{(l+m-1)(l+m)}{(2l-1)(2l+1)}} \right. \right.$$

$$\left. + \sqrt{\frac{(l-m)(l+m)}{(2l-1)(2l+1)}} \left(D_{l-1,m} e^{j\phi} + E_{l-1,m} e^{-j\phi} \right) \right] + \frac{1}{2} F_{l,m-1} e^{-j\phi} \sqrt{(l-m-1)(l+m)}$$

$$\left. - \frac{1}{2} F_{l,m+1} e^{j\phi} \sqrt{(l+m+1)(l-m)} \right\} r^{l-1} Y_{lm}(\theta, \phi) \quad (7)$$

Equations 5-7 are the N[th] order approximations of the analytical solution. The result converges to the exact solution with $N \to \infty$. In our calculations, we used N = 20

which gives sufficient accuracy based on the convergence rate. In what follows, we define C_{lm} for a one-wire loop figure-8 coil (Figure 3.1).

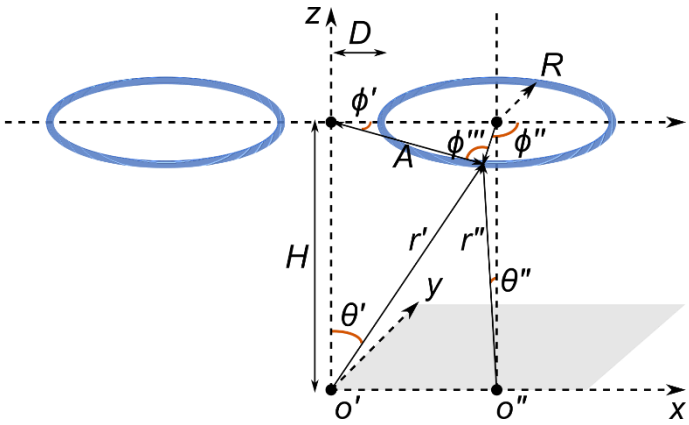

Figure 3.1 One wire loop figure-8 coil in a spherical coordinate system.

The one wire figure-8 coil consists of two loops, each with radius R that are parallel to the x-y plane, with the loops along the x-axis, and the center of the coil being a distance H (in our case, 7 mm) above the head. Both loops have a distance D from the z-axis. C_{lm} is calculated for each loop separately. For the loop on the positive side of the x-axis, to simplify the calculations, we translated the coordinate system in such a way that the center of the loop is directly above the new center of the coordinate system. The old coordinate system relates to the new coordinate system as follows.

Since the sum of the angles in a triangle is π radians,

$$\phi''' = \phi'' - \phi' \quad (8)$$

Using the law of sines in triangles, we have:

$$\frac{\sin\phi'}{R} = \frac{\sin\phi'''}{D+R} = \frac{\sin(\phi''-\phi')}{D+R} = \frac{\sin\phi''\cos\phi' - \cos\phi''\sin\phi'}{D+R} \quad (9)$$

And by simplification we get:

$$\phi' = \tan^{-1}\left(\frac{R\sin\phi''}{D+R+R\cos\phi''}\right) \quad (10)$$

According to the law of cosines in triangles, we have:

$$A = \sqrt{(D+R)^2 + R^2 - 2(D+R)Rcos(\pi-\phi'')} \quad (11)$$

$$\theta' = \tan^{-1}\left(\frac{A}{H}\right) = tan^{-1}\left(\frac{\sqrt{(D+R)^2 + R^2 - 2(D+R)Rcos(\pi-\phi'')}}{H}\right) \quad (12)$$

$$r' = \sqrt{H^2 + A^2} = \sqrt{H^2 + (D+R)^2 + R^2 - 2(D+R)Rcos(\pi-\phi'')} \quad (13)$$

Given such coordinate translation and assuming a counterclockwise direction for the loop current, the integral can be written as:

$$C_{lm} = \oint_{Coil} \frac{Y_{lm}^*(\theta',\phi')}{(2l+1)r'^{l+1}}\boldsymbol{dl}' = \int_{\phi"=-\pi}^{\pi} G_{lm}(\phi'')\boldsymbol{dl}' \quad (14)$$

where

$$G_{lm}(\phi'') = \frac{Y_{lm}^*\left(tan^{-1}\left(\frac{\sqrt{(D+R)^2 + R^2 - 2(D+R)Rcos(\pi-\phi'')}}{H}\right), \tan^{-1}\left(\frac{R\sin\phi''}{D+R+R\cos\phi''}\right)\right)}{(2l+1)\left(\sqrt{H^2 + (D+R)^2 + R^2 - 2(D+R)Rcos(\pi-\phi'')}\right)^{l+1}} \quad (15)$$

Therefore, by expanding the integral over x, y, and z orientations, we arrive at:

$$C_{lm} = C_{lm}^x\hat{\imath} + C_{lm}^y\hat{\jmath} + C_{lm}^z\hat{k}$$

Additionally, we know that in the new coordinate system

$$x = D + Rcos(\phi'')\,, \qquad y = Rsin(\phi''), \qquad z = H$$

Then,

$$C_{lm}^{x} = \int_{\phi"=-\pi}^{\pi} G_{lm}(\phi'')dx = \int_{\phi"=-\pi}^{\pi} -G_{lm}(\phi'')Rsin(\phi'')d\phi'' \quad (16)$$

$$C_{lm}^{y} = \int_{\phi"=-\pi}^{\pi} G_{lm}(\phi'')dy = \int_{\phi"=-\pi}^{\pi} G_{lm}(\phi'')Rcos(\phi'')d\phi'' \quad (17)$$

$$C_{lm}^{z} = \int_{\phi"=-\pi}^{\pi} G_{lm}(\phi'')dz'' = 0 \quad (18)$$

All the above steps can be repeated for the other loop with the opposite current direction. The only change will be:

$$G_{lm}(\phi'') = \frac{Y_{lm}^{*}\left(tan^{-1}\left(\frac{\sqrt{(D+R)^2+R^2-2(D+R)Rcos(\pi-\phi'')}}{H}\right), \pi + \tan^{-1}\left(\frac{R\sin\phi''}{D+R+R\cos\phi''}\right)\right)}{(2l+1)\left(\sqrt{H^2+(D+R)^2+R^2-2(D+R)Rcos(\pi-\phi'')}\right)^{l+1}} \quad (19)$$

Finally, both integral results are added together to calculate C_{lm} for the whole one wire figure-8 coil. However, the real coils often have multiple wire bindings. We implemented 9 nested concentric loops according to the specifications explained in the ‘3.2.4. Transcranial Magnetic Stimulation (TMS)’ section. We solved these equations in MATLAB (Mathworks, Inc., Natick, MA, USA) to obtain the electric fields induced in the spherical models.

3.2.3. Computational Modeling

We created tetrahedral models for 13 six-layer spherical models with an outer radius of 0.5 cm and 1–12 cm with 1 cm steps. Each model was linearly scaled

from the standard spherical model as included in SimNIBS 2.1 (Saturnino et al., 2019b) and originally created in Gmsh (Geuzaine and Remacle, 2009) with the following layers: “ventricles with CSF” (r = 25 mm, σ = 1.654 S/m), “white matter” (r = 75 mm, σ = 0.126 S/m), “grey matter” (r = 80 mm, σ = 0.275 S/m), “CSF” (r = 83 mm, σ = 1.654 S/m), “skull” (r = 89 mm, σ = 0.01 S/m), and “skin” (r = 95 mm, σ = 0.465 S/m). Each model has ~480 thousand tetrahedral elements. To ensure that found results for differing radii were not due to differences in tetrahedral element size, we also confirmed the results in high resolution spherical models (~8 million elements) for r = 8–12 cm. Then, these models were solved using Finite Element Method (FEM) in SimNIBS 2.1 to numerically calculate the electric field.

3.2.4. Transcranial Magnetic Stimulation (TMS)

We simulated the electric field for realistic 70 mm and 25 mm figure-8 coils. Both coils have 9 wire loops and were modeled in the FEM model using the magnetic dipole method as described and validated before (Thielscher and Kammer, 2004, 2002). The coil center was placed 4 mm above the sphere surface in all models. The input intensity dI/dt was 100 A/μs in every simulation as commonly used in human experiments (Rossi et al., 2009).

3.3. Results

3.3.1. Analytical Calculation of Electric Fields

The electric fields in the spherical model of different sizes stimulated by two TMS coil types were calculated using the analytical method. Figure 3.2 shows the

electric fields on the grey matter surface over a 2500-point grid for a spherical model with a 12 cm outer radius. The electric fields are strongest under the center of the coil and become weaker at farther locations. Overall, the electric fields follow the current flows in the TMS coil but in the opposite direction (as expected from the Lenz law). Furthermore, we observe that the electric field is more focal and lower in magnitude for the 25 mm TMS coil compared to the 70 mm TMS coil.

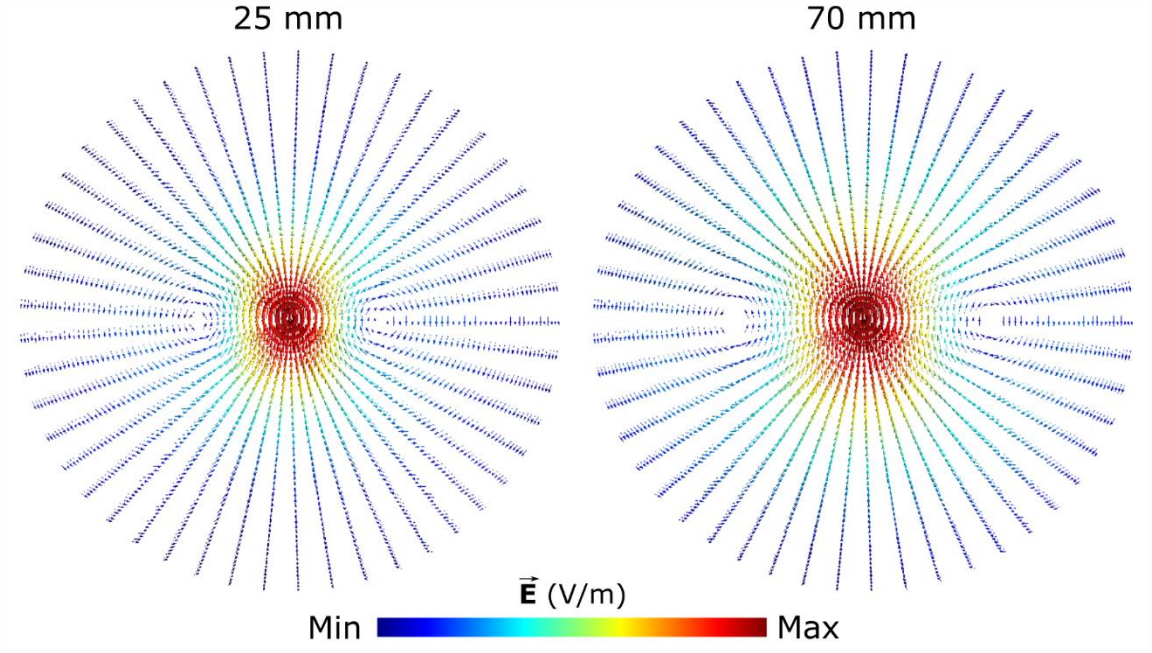

Figure 3.2 Analytical solutions for TMS-induced electric fields. Electric fields are shown on the grey matter surface in the spherical model with the outer radius of 12 cm stimulated by 25 mm (left) or 70 mm (right) figure-8 coil.

3.3.2. Numerical Solution of Electric Fields

Similarly, using FEM, we numerically calculated the electric fields induced for the spherical models of different sizes and two TMS coil types. Figure 3.3 depicts the electric fields on the grey matter surface of the model with the outer radius of 12

cm. The same pattern for the electric field distribution is observed as in the analytical solutions in Figure 3.2.

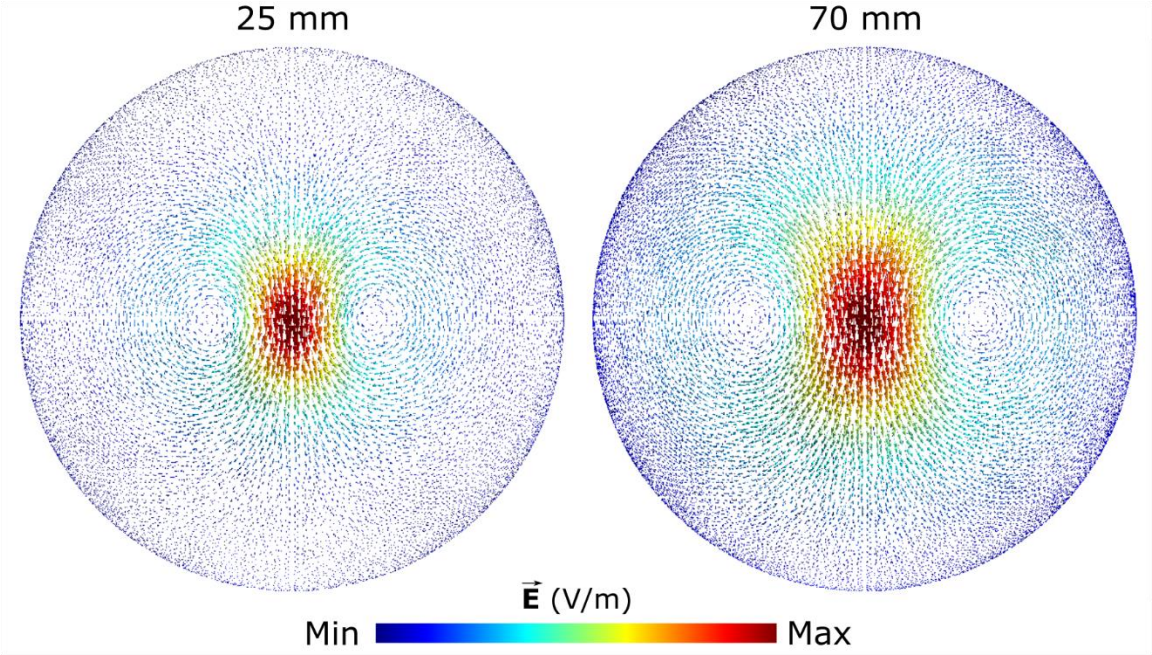

Figure 3.3 Numerical solutions for TMS-induced electric fields. Electric fields are shown on the grey matter surface in the spherical model with the outer radius of 12 cm stimulated by 25 mm (left) or 70 mm (right) figure-8 coil.

3.3.3. Comparison of Analytical and Numerical Methods

To systematically assess the electric field results for the analytical and numerical methods, we compared the maximum electric fields induced by TMS across different head sizes. We calculated the robust maximum (99.9th percentile) of the electric fields in each condition and plotted them in Figure 3.4 for comparison. The robust maximum of the electric fields in the FEM models closely matches the analytical solutions across head sizes and for both TMS coil types. This validates

the accuracy of the FEM models we used. Furthermore, our results indicate a two-term exponential relationship between the electric field and brain size. With increasing head volume, the TMS-induced electric field in the brain first gets stronger and then weaker following an exponential function. The inflection point occurs earlier for a smaller, 25 mm figure-8 coil than for the bigger 70 mm figure-8 coil. For the latter, both monkey and human head sizes are near the peak of the function.

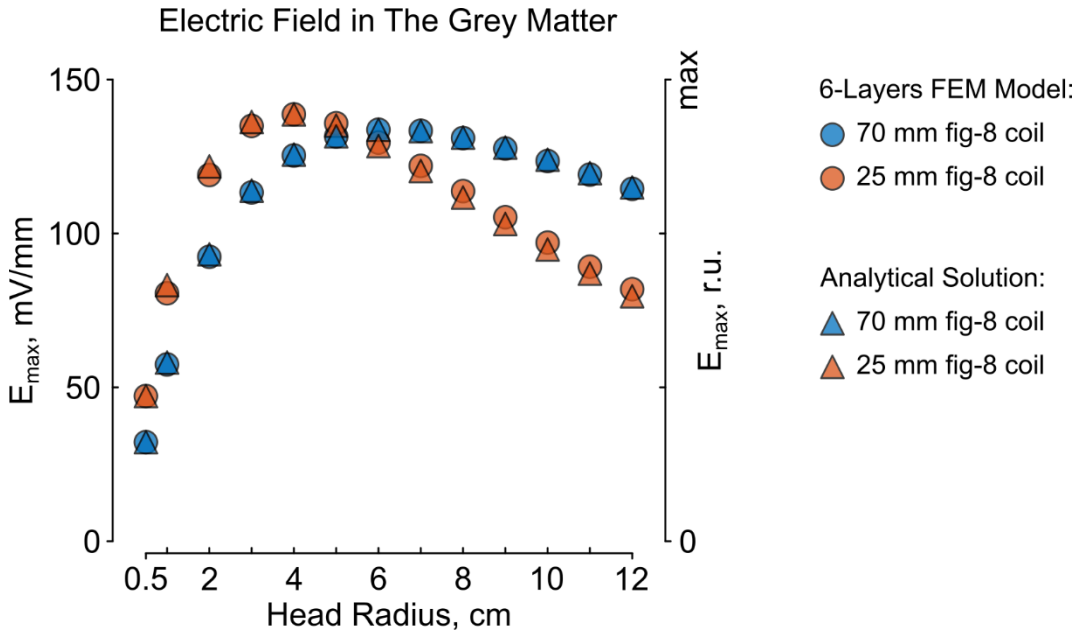

Figure 3.4 TMS-induced electric field strength as a function of head size. Results are shown in the grey matter for the FEM simulation approach (depicted with circles, left-side scale) and an analytical solution (depicted with triangles, right-side scale) in 6-layers spherical models.

3.4. Discussion

In this chapter, we derived the analytical equations governing the electric fields induced by TMS in a spherical model. Using these equations, we analytically

calculated the exact electric fields for spherical models of varying sizes stimulated by two figure-8 coils (25 mm and 70 mm). Moreover, we numerically computed the electric fields using the finite element method in SimNIBS and confirmed that the FEM results are highly comparable with the exact analytical solutions across all sphere sizes and coil types.

Furthermore, we found two key findings regarding TMS in spherical head models: (i) the electric field strength first increases with increasing head size and then decreases; (ii) the inflection point of this function depends on the coil size with the smaller coil showing a decrease in electric field strength starting at a smaller head size.

A possible mechanism for this effect is that the head underneath the TMS coil captures a fraction of the total magnetic flux. This fraction increases with increasing head size; thus, the induced electric field gets stronger (Weissman et al., 1992). However, once the head reaches a certain dimension relative to the coil size, the captured energy is maximized, but the induced electric current is spread through a larger conductive volume and thus creates a weaker electric field. For a smaller TMS coil, the maximum magnetic flux captured occurs at a smaller head volume, which results in an earlier decrease. The function of the induced electric field with increasing head size should reach an asymptote for much larger head sizes relative to the TMS coil (e.g. for micro coils) where the exact head size will not matter anymore, and coil characteristics will dominate the behavior. Our results also indicate that specific properties of the induced electric fields in the human

brain are better captured in monkeys than in mice due to a more comparable electric field strength in the brain and affected brain volume.

In summary, our findings validate and expand on previous modeling efforts and offer insight for translating the results of animal studies to humans.

The FEM models in this chapter were simulated by Kathleen Mantell, University of Minnesota, USA.

The materials in this chapter are published in NeuroImage (Alekseichuk et al., 2019)*.*

Chapter 4: Multi-scale Modeling Toolbox for Single Neuron and Subcellular Activity under (repetitive) Transcranial Magnetic Stimulation

> "Conscious and unconscious experiences do not belong to different compartments of the mind; they form a continuous scale of gradations, of degrees of awareness."
>
> - Arthur Koestler

4.1. Introduction

Transcranial Magnetic Stimulation (TMS) is a popular noninvasive brain stimulation method to safely modulate brain activity in the human brain. TMS generates a strong magnetic field by passing a transient current through a magnetic coil (Barker et al., 1985). This time-varying magnetic field crosses the skull and induces an electric field which can depolarize neurons in underlying brain areas (Hallett, 2007). TMS is used both in research and clinical applications for neuropsychiatric and neurological disorders (Lefaucheur et al., 2014). Despite the growing use of TMS, there is still a lack of understanding of its mechanism of action. There are several gaps in our understanding of how TMS influences the

brain at the network level, neuronal level, and subcellular scale. Such knowledge is essential to design more effective stimulation protocols and tailor its application to specific brain states. However, experimental difficulties and technology limitations for human recordings slow this progress. Non-invasive measurements of human brain activity such as electroencephalography (EEG) and functional magnetic resonance imaging (fMRI) cannot record TMS evoked activity at the single-neuron level. Thus, *in vivo* measurements of neuronal activity are typically limited to invasive animal studies. Direct recordings of neural activity in rodents and non-human primates have led to key insights into TMS mechanisms (Allen et al., 2007; Mueller et al., 2014; Romero et al., 2019). However, due to differences in brain structure and functional neuroanatomy compared to humans, great care has to be taken when translating findings across species (Alekseichuk et al., 2019). Besides *in vivo* animal studies, *in vitro* experiments in hippocampal slice cultures have been instrumental for our understanding of cellular and molecular mechanisms of TMS (Lenz et al., 2015; Tang et al., 2015; Tokay et al., 2009; Vlachos et al., 2012). *In vitro* preparations allow studying the effects of TMS on a single neuron basis in detail, however, as for animal studies, great care has to be taken for translating findings to humans.

Computational modeling is a key tool to complement experimental studies to investigate TMS mechanisms. Computational models can provide a framework to understand experimental results as well as allow efficient screening of a large range of stimulation parameters. Most TMS modeling studies have focused on the

spatial distribution of TMS-induced electric fields in the brain (Laakso et al., 2013; Opitz et al., 2013, 2011). These studies have been successful in predicting TMS stimulation regions and to guide TMS targeting for human experiments. However, they are limited in expanding our understanding of the TMS physiological response, since the relationship between the TMS electric field and the neural response depends on a variety of factors such as neuron type, electric field orientation, and ongoing activity (Di Lazzaro et al., 2018; Hannah and Rothwell, 2017). Moreover, physiological responses can vary nonlinearly with TMS intensity (Hanakawa et al., 2009; Komssi et al., 2004). Consequently, there has been a growing interest in developing neuron models to predict the physiological outcome of TMS. In such multi-scale modeling paradigms, initially, the TMS-induced electric field in the brain is computed at the macroscopic and mesoscopic scale. Then, the electric field is coupled with neuron models at the microscopic scale to estimate the neuronal response due to TMS.

Most modeling studies have used the cable equation (Rall, 1989) to model the neuronal responses. In earlier work, (Basser and Roth, 1991; Nagarajan and Durand, 1996; Salvador et al., 2011) studied the effects of magnetic stimulation on elongated cables that represent the axonal tracts of pyramidal neurons. More recent work (Goodwin and Butson, 2015; Kamitani et al., 2001; Pashut et al., 2011; Seo and Jun, 2019) have used sophisticated neuronal geometries. (Aberra et al., 2020) highlighted the need to include realistic axonal reconstructions and myelination to more accurately predict TMS thresholds and action potential

initiation. There are two fundamental limitations of hitherto existing TMS models. First, common to all these modeling studies has been their focus on single-pulse TMS. However, for clinical applications, TMS is applied repeatedly in specific temporal patterns (repetitive TMS [rTMS]). Second, these rTMS protocols are designed to induce neural plasticity that is guided by several subcellular processes including somatic and dendritic calcium accumulation (Eilers et al., 1995; Limbäck-Stokin et al., 2004; Shoop et al., 2001). However, although experimental data indicates that the rTMS-induced plasticity of excitatory and inhibitory synapses is strongly dependent on intracellular calcium signaling pathways (Lenz et al., 2016, 2015; Vlachos et al., 2012), subcellular calcium-dependent processes have been so far neglected in current computational models of TMS.

Calcium signals have been shown to be involved in a multitude of cellular processes that are involved in learning, development, and cell survival (Bezprozvanny, 2009; Bezprozvanny and Hayden, 2004). Furthermore, disruption of the calcium code is implicated in various neurodegenerative diseases, such as Alzheimer's or Parkinson's disease (Chan et al., 2009; Cheung et al., 2008; Green and LaFerla, 2008; Mattson et al., 1992; Stutzmann et al., 2006). In the context of rTMS, experimental data indicates that the rTMS-induced reduction in dendritic inhibition, as well as plasticity of excitatory synapses, are strongly dependent on intracellular Ca^{2+} signaling pathways (Lenz et al., 2016, 2015; Vlachos et al., 2012). Changes at the synapse level could potentially integrate into changes in synapse-to-nucleus calcium signaling pathways, which are responsible for long-

term learning, memory formation, and survival (Bezprozvanny, 2009; Bezprozvanny and Hayden, 2004). The effect of morphological reorganization in spines has previously been shown to affect spine-to-dendrite calcium signaling (Breit et al., 2018; Breit and Queisser, 2018). Moreover, spatio-temporal changes in synaptic activity can alter the robustness of calcium waves in dendrites towards the nucleus (Breit and Queisser, 2018).

Therefore, biophysical realistic models of calcium signaling processes in response to rTMS have the promise to predict plasticity processes for TMS and further our understanding of TMS-evoked subcellular responses.

To address these two limitations of available TMS models, here, we develop a multi-scale modeling toolbox coupling TMS electric fields with anatomically and biophysically realistic neuron models, and their intracellular calcium signaling. TMS multi-scale modeling requires the detailed knowledge of a broad range of computational tools, and so far, no easy-to-use toolboxes exist. This has impeded both experimental and computational researchers from using these methods. Below we describe a newly developed *Neuron Modeling for TMS* (*NeMo-TMS*) pipeline that allows developing realistic multi-scale models from neuronal reconstructions (https://github.com/OpitzLab/NeMo-TMS). Users can simulate TMS multi-scale models with minimal technical expertise. Additionally, we provide functionality for visualization and post-processing of results. Our modeling toolbox will allow researchers to computationally explore TMS mechanisms and embed

experimental findings in a theoretical framework that can facilitate our understanding of TMS mechanisms across scales.

4.2. Results

4.2.1. Overview of Multi-Scale Modeling Paradigm

We give an overview of the concept of multi-scale modeling to study the effects of TMS on neurons at the cellular and subcellular levels as shown in Figure 4.1. First, we use the Finite Element Method (FEM) to numerically calculate the electric fields induced in the geometry of interest (e.g. *in vitro* model or head model, Figure 4.1A). However, the resulting electric fields at the macroscopic and mesoscopic scale cannot directly predict the physiological outcome. Therefore, we model the neuron membrane response to these external electric fields. To this end, we reconstruct CA1 pyramidal neurons based on microscopic images of enthorhino-hippocampal tissue cultures prepared from mice (Figure 4.1B). Based on the neuron morphology, we then generate a discretized numerical model of the neuron. Then, to couple the electric fields from the FEM model to the neuron model, we calculate quasipotentials (Figure 4.1C) across all the neuron compartments (Wang et al., 2018). Afterward, the neuron model is numerically solved to estimate the membrane potential across the whole neuron over time (Figure 4.1D). Based on the calculated voltage traces, we solve the equations governing the calcium dynamics to calculate the calcium concentrations in the neuron over time at the subcellular level (Figure 4.1E).

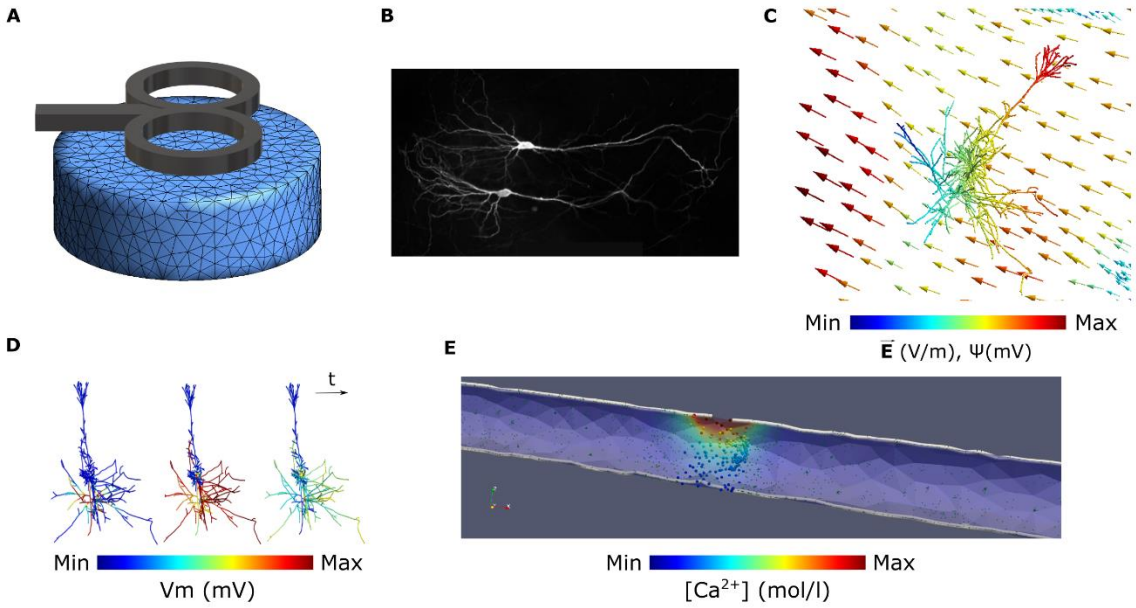

Figure 4.1 Overview of the multiscale modeling paradigm. (A) Electric field calculation in the FEM model of interest. **(B)** Neuron reconstruction of CA1 pyramidal cells from microscopic images. **(C)** Coupling the electric fields ($\vec{E}$) to the morphologically accurate neuron model by calculating quasipotentials (ψ). **(D)** Simulating the membrane voltage (Vm) using the quasipotentials and computing the voltage traces of the neuron compartments over time. **(E)** Simulating the release of calcium ions from the voltage-dependent calcium channels (VDCC) over time by solving the calcium diffusion equations.

4.2.2. *Neuron Modeling for TMS* (*NeMo-TMS*) Toolbox

To facilitate the process of multi-scale modeling, we have developed a new toolbox (*NeMo-TMS*) and share it as an open-source resource with instructions (https://github.com/OpitzLab/NeMo-TMS) accessible to the research community. We tested the toolbox on Microsoft Windows and Ubuntu. Here, we outline the toolbox functionality and the steps to perform multi-scale simulations. Furthermore, we provide examples to show how it can be used to investigate TMS-related research questions.

As shown in Figure 4.2, the pipeline is comprised of multiple steps that allow the user to run multi-scale models. We have shared all the necessary codes and instructions to run multiscale models with minimal prerequisites from the user. Below we summarize typical steps in the modeling process:

1. Neuron models are generated from realistic neuron reconstructions and the biophysics of CA1 pyramidal cells are automatically added to these models.
2. Coordinates of the neuron model compartments are exported to be used in later steps.
3. The macroscopic electric fields are numerically calculated in the geometry of interest (e.g. *in vitro* model, head model). This accounts for the spatial distribution of the electric fields.
4. The electric fields computed in step 3 are coupled to the neuron model by calculating the quasipotentials at the coordinates exported in step 2.
5. Desired rTMS waveforms are generated in this step. This accounts for the temporal pattern of the electric fields.
6. The membrane voltage of the neuron is simulated based on the spatial and temporal distribution of the TMS electric fields calculated in the previous steps. Alternatively, the user can also run this step under the assumption of a spatially uniform electric field (in this case, steps 2 to 4 can be skipped).
7. The membrane voltage data are exported in formats compatible with calcium modeling.

8. The calcium concentration is simulated based on solving the calcium diffusion-reaction equations with voltage-dependent calcium channels.
9. The results from the simulations are visualized.

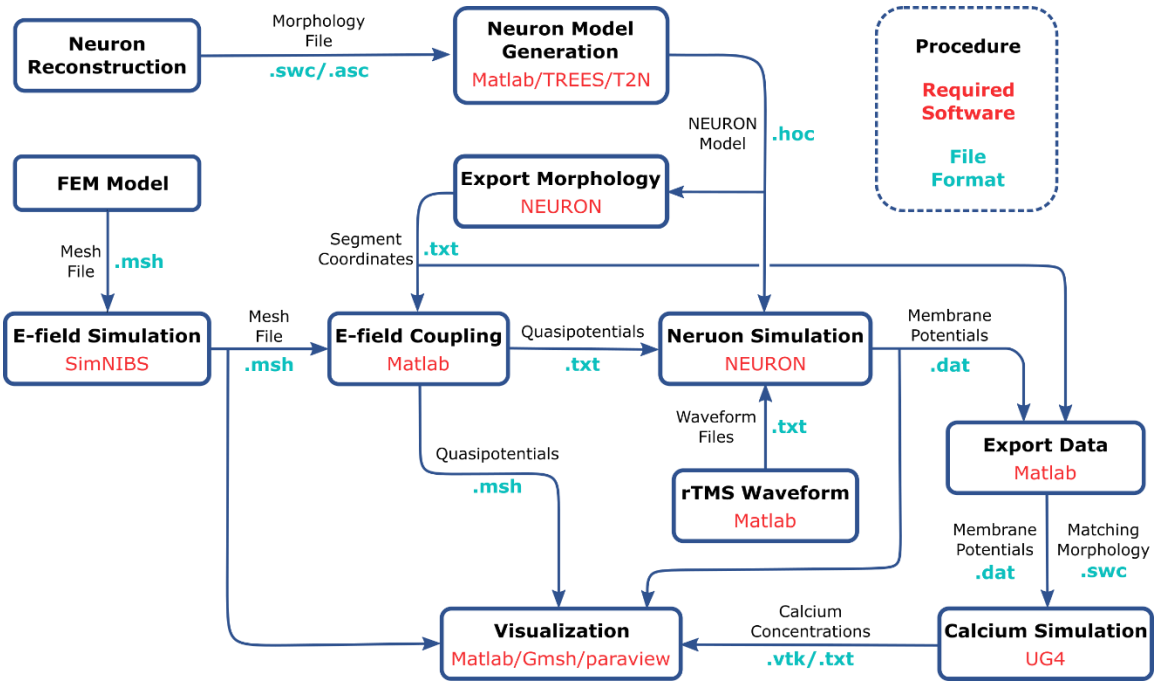

Figure 4.2 Pipeline overview. Each step of the procedure is represented in a box. The software used for each step are shown in red. The file formats of the input and output files are shown in blue.

This toolbox is developed by utilizing multiple software packages, methods, and algorithms. Because of this and to make the toolbox accessible to a broad range of researchers with varying computational skills, we have simplified and automated the process to a great degree. For all the steps described above, the user can run the simulations using either graphical interfaces or through scripting. This feature is useful as it makes the computational workflow reproducible and gives advanced users the ability to run multiple simulations programmatically. With the *NeMo-TMS*,

we provide a set of ten morphologically accurate neuron reconstructions from young Wistar rats with detailed dendritic and axonal branches to run example simulations. The morphology of these neurons is shown in Figure 4.3. For further technical details on the pipeline procedure, refer to the ‘methods’ section.

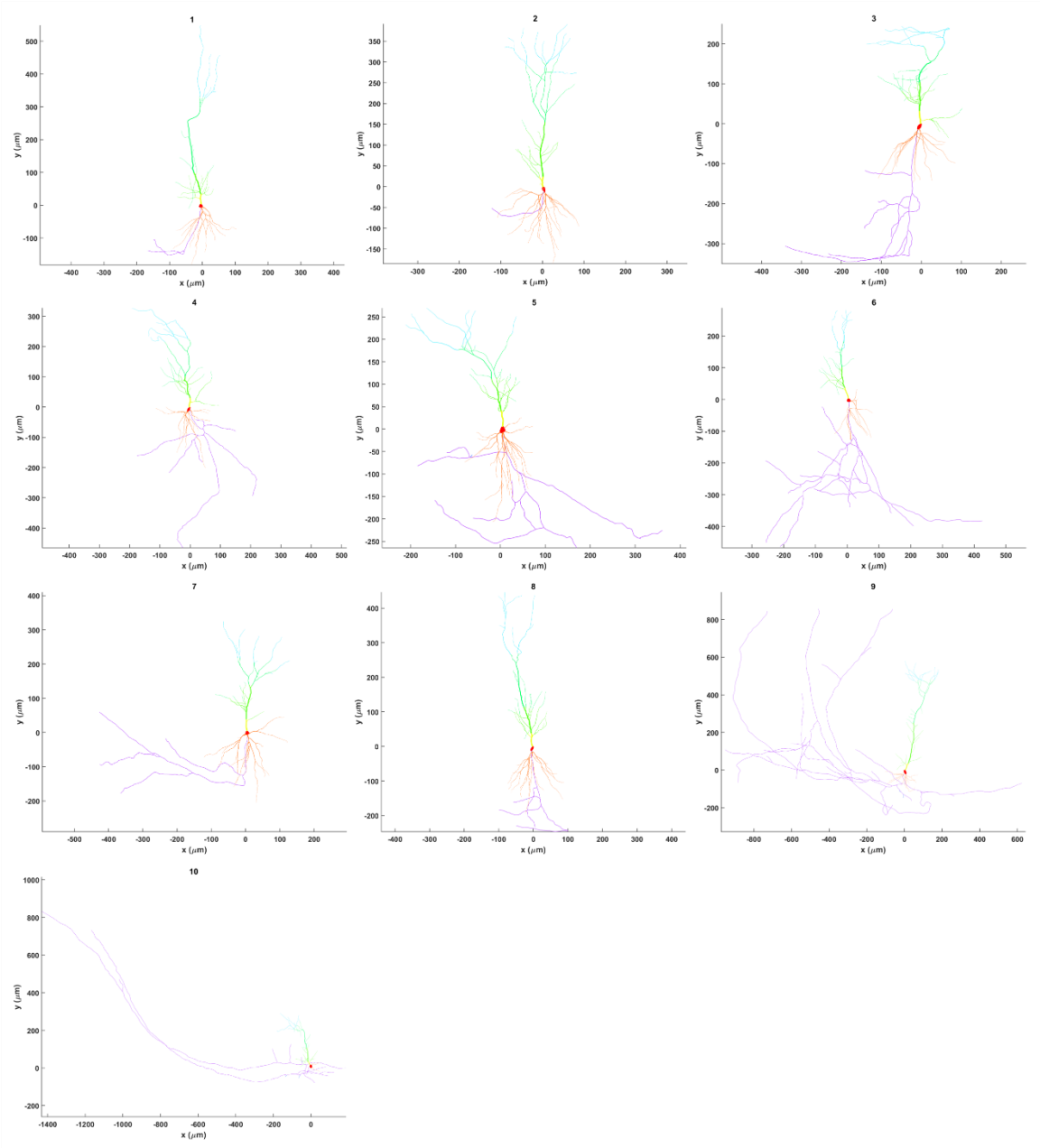

Figure 4.3 Morphological reconstruction of the ten rat CA1 pyramidal cells. Red, orange, yellow, green, blue, and purple branches respectively represent soma, basal dendrites, proximal apical, distal apical, apical tufts, and axon.

4.2.3. Example 1: Effects of TMS on the membrane potential and calcium concentration for an *in vitro* neuron model

In this example, we run a full multi-scale simulation on an *in vitro* model and show the membrane potential and calcium activity of the neuron when a TMS pulse is delivered. As shown in Figure 4.4A, the *in vitro* model consists of a tissue culture placed inside a Petri dish surrounded by artificial cerebrospinal fluid (aCSF). The Petri dish is modeled as a cylinder with 30 mm in diameter and 10 mm in height. The tissue culture is 2 x 1.5 x 0.3 mm in size and is placed at the center of the Petri dish 8 mm above the bottom surface. The mesh file for this model is available for download (Alekseichuk et al., 2020). The electrical conductivity of the aCSF and the tissue culture are set to those of CSF (1.654 S/m) and grey matter (0.275 S/m) respectively (Wagner et al., 2004). A dipole-equivalent model of a Magstim 70 mm figure-8 coil (Magstim Co., UK) was placed 4 mm above the center of the Petri dish. We ran the FEM electric field simulation with a stimulator output of dI/dt = 220 A/μs. The resulting electric fields are strongest at the top center of the model since these regions are closest to the center of the TMS coil (Figure 4.4B). Electric fields are aligned unidirectionally in the probe (Figure 4.4C). Due to a conductivity difference between grey matter and CSF, an increase in the electric field occurs at these border walls (Opitz et al., 2015). The morphology of the reconstructed neuron is shown in Figure 4.4D. We placed the neuron model inside the tissue

culture at the edge of the wall and oriented it in a way that the electric fields are in the direction of the neuron somatodendritic axis (Figure 4.4E). Then, we coupled the electric fields to the neuron by calculating the quasipotentials across the neuron (Figure 4.4F). A gradient of quasipotentials occurs in the direction of the electric field.

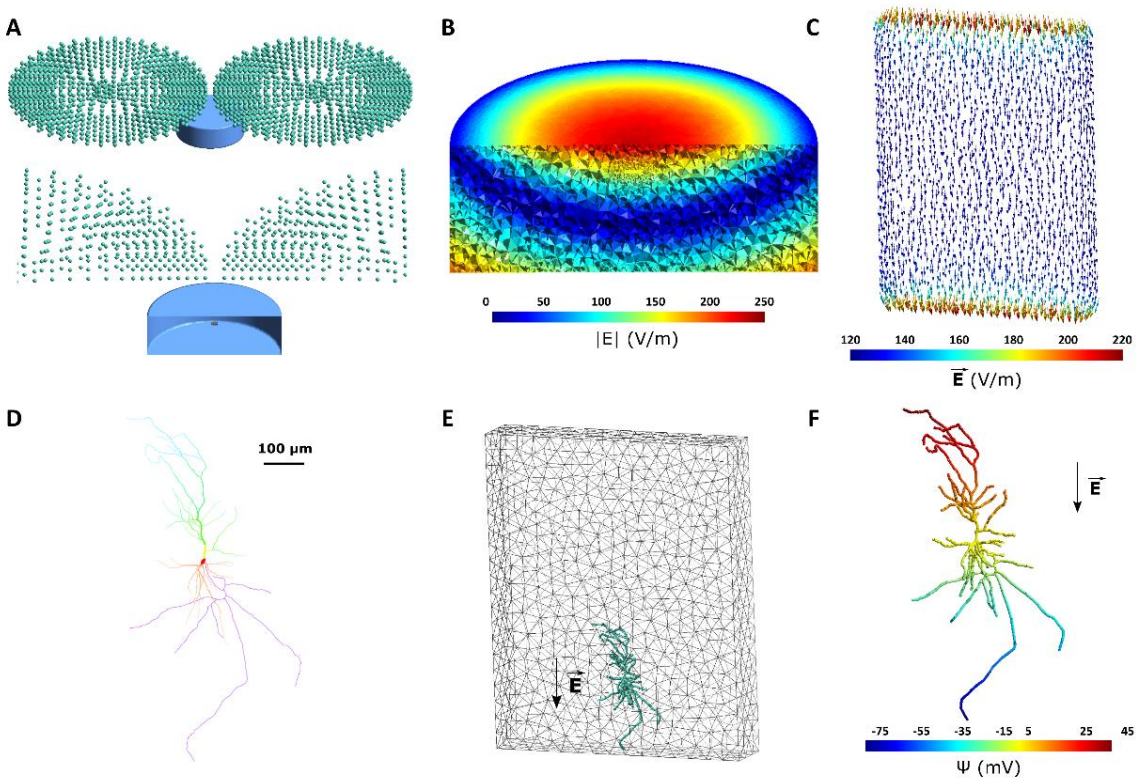

Figure 4.4 In vitro model of tissue culture in a Petri dish. (A) Geometry of the *in vitro* model. Top: TMS coil is represented through green magnetic dipoles. The Petri dish, shown in blue, is 30 mm in diameter with a height of 10 mm and is filled with aCSF. The figure-8 coil is placed 4 mm above the center of the Petri dish. Bottom: A cut-through image of the TMS coil and Petri dish is shown. The tissue culture with a size of 2 x 1.5 x 0.3 mm is placed at the center of the Petri dish 8 mm above the bottom surface. The tissue culture is modeled with grey matter conductivity. **(B)** Electric field magnitude induced in the *in vitro* model for a TMS stimulator output of dI/dt = 220 A/µs. **(C)** Electric field vector induced in the tissue culture. Electric fields are aligned unidirectionally along the handle of the figure-8 coil. Due to the conductivity mismatch between the culture and aCSF in the Petri dish, the electric field is enhanced at the borders along the electric field direction. **(D)** Reconstructed neuron morphology. Red, orange, yellow, green, blue, and purple respectively denote soma, basal dendrites, proximal apical, distal apical, apical tufts, and axon. **(E)** Neuron (green) placement inside the tissue culture (grey mesh). **(F)** The quasipotential distribution across

the neuron compartments. In this model, the electric field is applied along the somatodendritic axis, thus a gradient can be seen from the apical dendrites to the axon.

Subsequently, we simulated the membrane dynamics of the neuron compartmental model using the CA1 pyramidal cell biophysics (Jarsky et al., 2005) in response to the applied electric field with the quasipotential mechanism. The resulting membrane voltage traces are then used as input to the simulation of the calcium dynamics for this neuron. While action potential initiation occurs on a millisecond timescale, calcium accumulation in the soma occurs with a delay which can be in the range of seconds in the case of rTMS. Figure 4.5 shows the membrane potential of the neuron and its corresponding calcium concentrations over time during a single biphasic TMS pulse. Before the TMS pulse delivery, the neuron is at resting membrane voltage all across the cell (-70 mV). At time 0, the TMS pulse is delivered. Immediately after the TMS pulse, the axon terminal at the bottom of the cell is depolarized enough to induce an action potential. Since the axon is myelinated, the action potential quickly travels across all axonal branches and reaches the soma around 1 ms later. Afterward, the dendrites slowly depolarize as a result of ionic diffusion. Since basal dendrites are shorter, they depolarize faster than the apical dendrites. Over time (approximately 4 ms), the neuron gradually recovers back to the resting potential. Apical and tuft dendrites are the last neurites to depolarize and therefore the last ones to return to rest. The bottom panel shows the calcium densities across the neuron for the same neuron spike. Once the action potential reaches the soma at around 1 ms after the TMS

pulse, with a short delay of about 0.5 ms, calcium accumulation is initiated in the soma. Then, the calcium levels start to rise slowly at the basal and apical dendrites. For these simulations, calcium exchange and release mechanisms are not considered in the axon region of the neuron; therefore, the calcium concentration remains constant in the axon of the cell. Afterward, the calcium densities in the rest of the neuron decrease and approach the resting values again (~5 ms). However, it takes longer for the calcium in the soma to fully restore to the baseline.

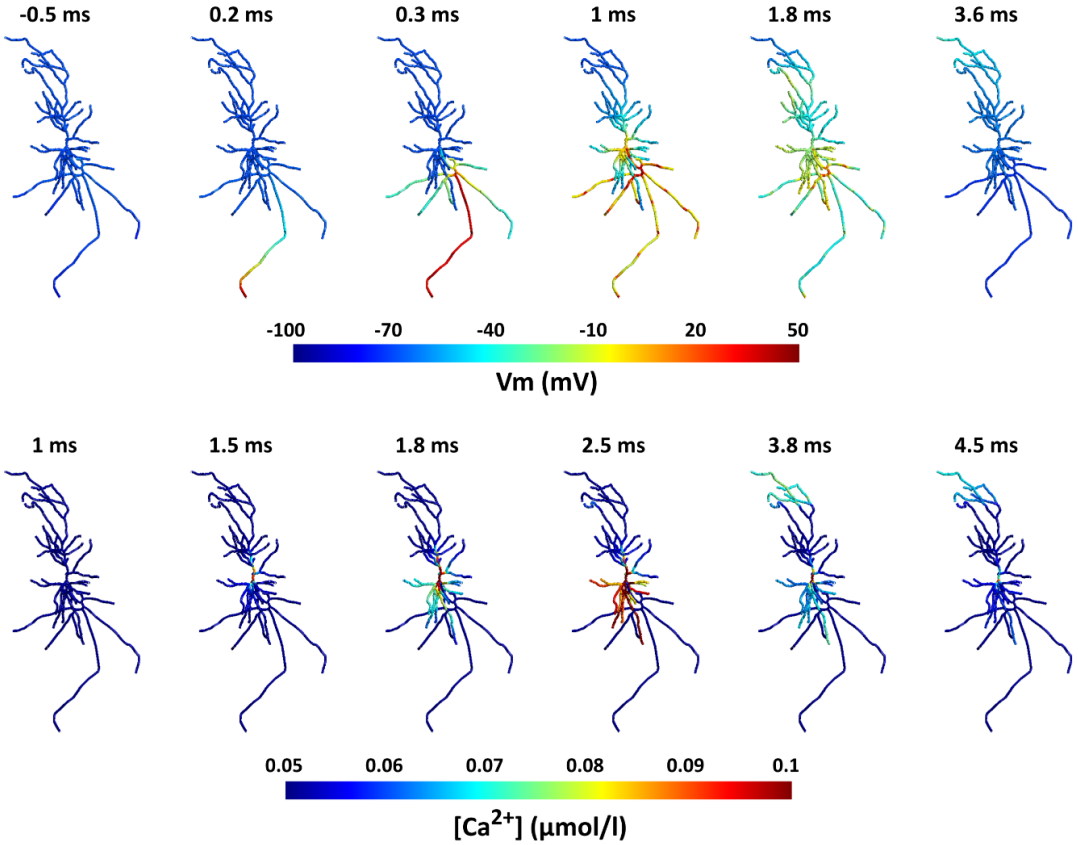

Figure 4.5 Action potential and calcium density propagation over time for the *in vitro* model. Note that time scales of membrane potentials and calcium dynamics differ between the upper and lower panel. Top: Spatial distribution of membrane potentials over time. The action potential starts at the axon terminal immediately after the TMS pulse (t = 0) and quickly propagates to the rest of the neuron. In the following ~4 ms, the neuron recovers back to its resting potential. Bottom: Distribution of the calcium concentrations displayed for the same TMS action potential. After the

action potential reaches the soma ~1 ms after the TMS pulse, shortly after (~0.5 ms), the calcium concentration increases in the soma and then propagates to the dendrites. After several ms calcium levels resort to baseline. The range of the color bar for the calcium concentrations was adjusted for improved visualization and does not represent the maximum values.

4.2.4. Example 2: Effect of rTMS pulse parameters on calcium dynamics

In this example, we examine the effect of rTMS pulse parameters on calcium accumulation. For this, we keep all single-pulse parameters as in example 1 and only change the rTMS protocol. We compare a 10 Hz rTMS protocol with a Theta Burst Stimulation (TBS) protocol (Huang et al., 2005). In the TBS protocol, a burst of three TMS pulses is delivered at 50 Hz repeated at 5 Hz (200 ms delay between bursts). In Figure 4.6, the membrane potential and the calcium concentration in the soma are shown over several TMS pulses for both protocols. After each TMS pulse, the neuron spikes, and therefore calcium accumulation in the soma follows. For the 10 Hz rTMS protocol, after each neuron spike, there is a rapid increase and then a decrease in the calcium level in the soma. However, after this initial activity, the decay rate slows dramatically. Since the calcium concentration does not completely recover to baseline before the subsequent pulse, there is a gradual increase in the overall calcium level. On the other hand, for the TBS protocol, since TMS pulses are very close together in each burst, calcium reaches higher concentrations after each burst but also decays quicker than the 10 Hz protocol. Although, because the bursts are fairly close together, the calcium level stays higher than the baseline. (Figure 4.6D). Overall, a buildup of calcium occurs in the soma over time in both rTMS protocols, but the temporal patterns are different.

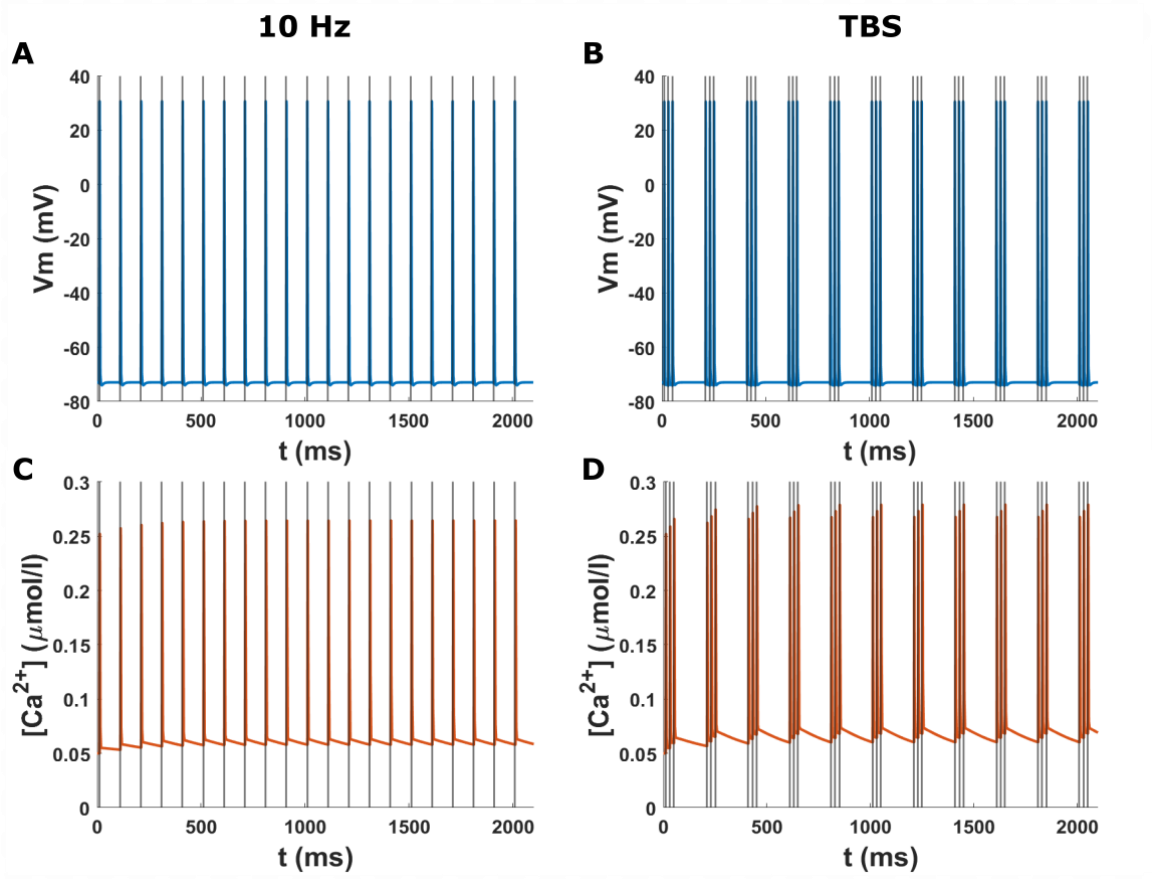

Figure 4.6 Time course of the membrane potential and calcium concentration at the soma in the in vitro model for two rTMS protocols. The grey lines indicate the TMS pulses. **(A)** Membrane potential at the soma for the 10 Hz biphasic rTMS protocol. The neuron spikes immediately after each TMS pulse. **(B)** Membrane potential at the soma for the TBS protocol with a biphasic TMS pulse. **(C)** Calcium concentration at the soma for the 10 Hz rTMS protocol corresponding to (A). Calcium levels rise after each spike and then slowly recover. Over time, there is a buildup of calcium. **(D)** Calcium concentration at the soma for the TBS protocol corresponding to (B). The calcium levels rise after each burst of pulses and then subside. The calcium levels stay higher than the baseline.

4.2.5. Example 3: Effect of the electric field orientation on neural activation

In this example, we show how the orientation of the TMS electric field can change how it affects the neural activation site and subsequently calcium dynamics. Since the spatial distribution of the electric field plays a key role in TMS effects (Opitz et al., 2013), we compared two different electric field directions and their effects on

the neuron TMS response. For this, we used one of the features of the pipeline to apply a spatially uniform electric field rather than from FEM modeling. We applied a monophasic TMS pulse in two different orientations: *i*) along the somatodendritic axis from the apical dendrite to the longest axon branch, *ii*) At 45° relative to the somatodendritic axis, along the second-longest axon branch. The neuron activation pattern is shown for these scenarios respectively in Figure 4.7. In the first case, since the electric field is aligned with the long axon branch, the action potential is initiated in the terminal of the long axon branch. However, in the second scenario, the action potential is initiated in the terminal of the second-longest axon since it is more suitably aligned to the electric field. Additionally, the threshold of the electric field strength for generating the action potential differs in both cases. In the first scenario the neuron fires at an electric field strength of 170 V/m, while in the second case, a 30% higher field strength is needed for the neuron to fire. Also, there is a time shift (~0.2 ms) between the action potential initiation and propagation between these electric field orientations. This time shift causes a delay in calcium accumulation between these conditions. This example shows that the electric field orientation plays a role not only in the activation thresholds but also in the neuron firing pattern, and calcium dynamics timing.

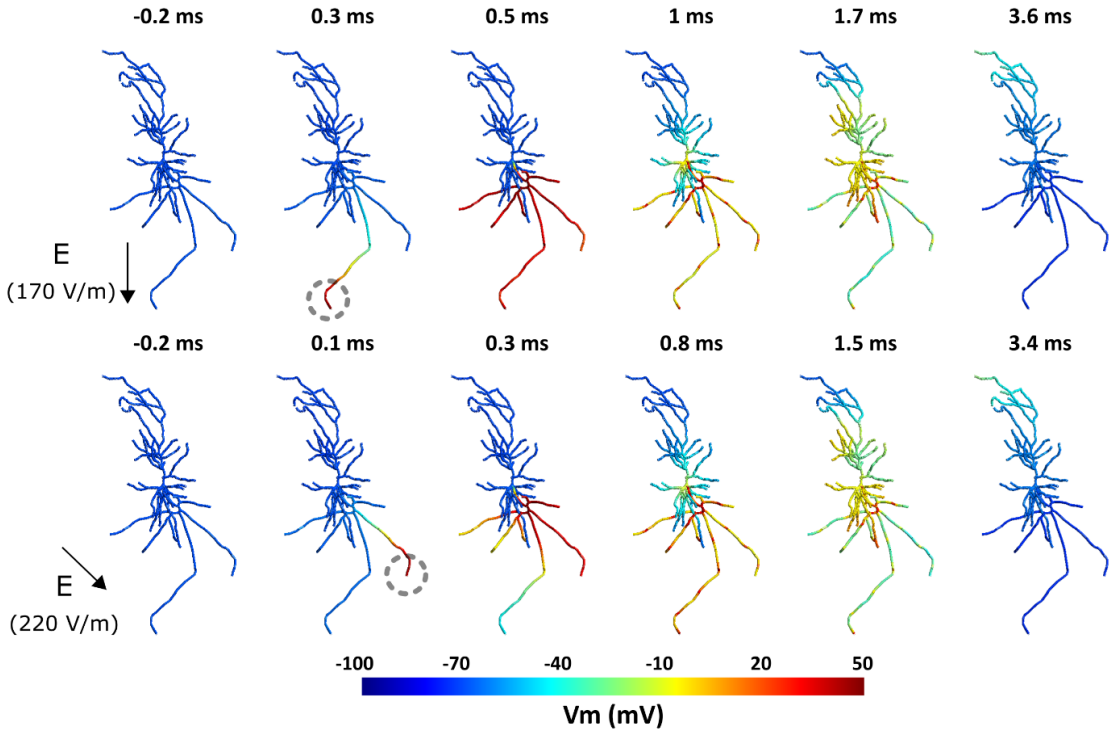

Figure 4.7 Effect of the TMS electric field orientation on membrane dynamics and spiking threshold. Top: Spiking activity in the neuron for a 170 V/m intensity uniform electric field with a monophasic TMS pulse oriented along the somatodendritic axis. The action potential initiates at the bottom-most axon terminal indicated with a grey dashed circle. Bottom: Spiking activity for a 220 V/m intensity uniform electric field with a monophasic TMS pulse oriented at 45° relative to the somatodendritic axis. The action potential starts at the axon terminal on the right.

4.3. Materials and Methods

4.3.1. Neuron Model Generation

We integrated a series of software tools into an automated pipeline for generating NEURON compartmental models (Hines and Carnevale, 1997) for modeling the effect of TMS on single brain cells. This pipeline is capable of generating models from commonly used file formats, i.e., SWC and Neurolucida ASCII files. Note that it is up to the user to ensure the input morphologies are correct, high-quality and

without artifacts, otherwise the model generation may fail in the process or the simulation results would not be reliable. We tested the pipeline on the ten reconstructions of rat CA1 pyramidal cells provided here, as well as other morphology files.

Since the axonal reconstructions do not include myelination, this pipeline allows the user to myelinate the axon automatically, or to leave the neuron unmyelinated. For this, we implemented a modified variant of the myelination algorithm used in (Aberra et al., 2018). Nodes of Ranvier were placed at all bifurcation points in the axon arbor, as well as regularly at 100μm intervals. All internodal segments except terminal segments shorter than 20μm were myelinated. As most publicly available reconstructions of CA1 pyramidal neurons do not have an axon, the pipeline also features a provision for potential automatic addition of a straight artificial axon; in this case, the axon is a straight line emanating from the basal region of the soma with the first 10um a hillock segment, the next 15μm the axon initial segment, followed by six 100μm long myelinated internodal segments with regularly spaced 1μm long nodes of Ranvier.

Biophysics

The NEURON compartmental models were generated using the T2N extension of the TREES Toolbox (Beining et al., 2017), which translates the TREES Toolbox morphological data into NEURON's HOC format and endows the model with biophysics in the MATLAB environment (Mathworks, Inc., Natick, MA, USA). Our models implement a generalized version of the Jarsky model of the CA1 pyramidal

cell (Jarsky et al., 2005). This includes the passive properties: C_m = 0.75 μF/cm^2, R_a = 200 Ω-cm, Rm = 40000 Ω/cm^2. Additionally, axon myelinated segments had a significantly reduced C_m of 0.01 μF/cm^2, while axon nodes had R_m of 50 Ω/cm^2. The models included three voltage-gated conductances: a Na^+ conductance, a delayed rectifier K^+ conductance, and two A-type K^+ conductances. The values of these conductances are assigned according to distance from the soma as described in (Jarsky et al., 2005). While the Na^+ and K_{DR}^+ conductances are fixed at 0.04 S/cm2, the value of the K_A^+ conductances steadily increases from 0.05 S/cm2 at the soma to 0.3 S/cm2 at 500μm from the soma. There is a crossover point between the two different K_A^+ conductances at 100μm from the soma. Furthermore, the extracellular mechanism (Hines and Carnevale, 1997), which allows for injection of extracellular electric potentials was inserted into the models by T2N simultaneously with the other biophysics. Following the generation of the model files by T2N, other necessary files for the next steps are also generated and automatically placed in the correct location.

4.3.2. FEM Modeling of the TMS induced Electric field

To study the behavior of neurons under non-invasive brain stimulation, the first step is to calculate the electric field generated at the macro- and mesoscopic scale. This includes computing the spatial distribution and time course of the TMS electric field. Since the stimulation frequency is relatively low, we can use the quasi-static approximation to separate the spatial and temporal components of the electric field (Plonsey, 1969, p. 203; Plonsey and Heppner, 1967; Windhoff et al., 2013). For

the spatial component, Maxwell's equations need to be solved for the model of interest. Exact analytical solutions can be determined for simple geometries such as concentric spheres with homogenous electromagnetic properties (Eaton, 1992). However, for more complex geometries such as the human brain, numerical simulations are used to calculate the electric field distribution. Several methods exist to perform these simulations such as the boundary element method (Nummenmaa et al., 2013; Salinas et al., 2009) and the finite element method (Miranda et al., 2003; Wagner et al., 2004; Weiping Wang and Eisenberg, 1994). Here we calculate TMS-induced electric fields using FEM models implemented in the open-source software SimNIBS v3.1 (Saturnino et al., 2019a). SimNIBS is a versatile simulation platform that can simulate TMS electric fields for various geometries and a variety of TMS coils.

Under the quasi-static assumption, the time course of the TMS electric field is the same as that of the TMS stimulation output (rate of change (dI/dt) of the coil current). Therefore, after determining the spatial distribution of the electric field, we can find the electric field at any time point by scaling the spatial distribution to the TMS waveform. For further details about the TMS waveform, refer to the 'Stimulation Waveform Generation' section below.

4.3.3. Electric field Coupling to Neuron Models

After calculating the macroscopic TMS electric fields induced in the FEM model of interest, these external fields need to be coupled with the neuron models. In this pipeline, this is performed following: 1) Coordinates of the neuron compartments

from the neuron model in the NEURON environment are exported to a text file. 2) The FEM model including the electric fields and the neuron coordinate files are imported to MATLAB. 3) The user enters the desired location and depth (relative to the grey matter surface) of the neuron. 4) Based on the values provided in step 3, the neuron is translated to the desired location. Additionally, the neuron is automatically orientated normal to the grey matter surface as this orientation represents the columnar cytostructure of major neurons (Amunts and Zilles, 2015; DeFelipe et al., 1990; Mountcastle, 1997). However, different preferred orientations can be set if desired. The new neuron compartmental coordinates are calculated based on this coordinate transformation. 5) The electric field at the location of neuronal compartments is interpolated from the macroscopic TMS electric fields calculated in the FEM model. 6) In this step, the user can scale the electric field strength if needed. Since the electric field strength scales linearly with the stimulation intensity, one can easily scale the electric fields instead of rerunning the FEM simulations at different intensities. This allows expediting the simulations e.g. for simulating multiple TMS intensities. Note that this is only true for the stimulus intensity and not applicable if the coil location/orientation, or the FEM model is changed. 7) The quasipotentials are computed over all compartments as described in (Wang et al., 2018). This allows us to convert all necessary information needed to incorporate the external TMS-induced electric fields into a single scalar input at each coordinate of the neuron model. 8) The quasipotentials are written in a file that will be used later in the pipeline for the NEURON

simulations. Additionally, the neuron (transformed to the desired location) and the FEM model are exported as mesh files for visualization.

To simplify the multi-scale modeling process, we have also enabled an alternative method to skip the FEM electric field modeling and the corresponding coupling step. In this case, the electric field is assumed to be spatially uniform over the extent of the neuron. This allows us to specify the TMS-induced electric field everywhere using a single scalar for the amplitude and a vector for orientation. Typically, since neurons are considerably smaller than the TMS coil and the head model, the electric field distribution confined to a single neuron region is mostly uniform. Therefore, the uniform electric field approximation provides sufficiently accurate results in the majority of cases. However, note that the uniform electric field approximation does not always hold. This occurs mainly in the following cases: 1) The neuron crosses a tissue boundary e.g. between Grey matter and white matter (Opitz et al., 2011). Due to the difference in electrical conductivities between tissues, a difference in the electric fields can arise between tissues. 2) The neuron is spatially extended (e.g. neurons with long axonal projections) that the homogeneity of the electric field over small scales does not apply anymore. 3) The tissue surrounding the neuron is highly inhomogeneous. Although this is a rare scenario since usually the tissues are assumed to be homogenous in FEM models for the purpose of estimating electric fields under non-invasive brain stimulation.

In the case of a uniform electric field, the quasipotentials equation can be simplified to the following expression:

$$\psi = -\int \vec{\boldsymbol{E}}.d\vec{\boldsymbol{s}} = -\vec{\boldsymbol{E}}.\vec{\boldsymbol{s}} = -(E_x x + E_y y + E_z z) \quad (1)$$

Where $\vec{\boldsymbol{E}}$ is the electric field, $\vec{\boldsymbol{s}}$ is the displacement vector, E_x, E_y, and E_z stand for the Cartesian components of the electric field, and x, y, and z denote the Cartesian coordinates of each compartment. Due to the simplicity of this equation, this step is computed in the NEURON environment.

Regardless of whether the electric field is uniform or based on the FEM model, the quasipotentials are calculated at each neuron segments (as exported from the NEURON model) and applied to the neuron simulations by using the extracellular mechanism available in the NEURON environment (Aberra et al., 2018; Hines and Carnevale, 1997). This process accounts for the exogenous fields induced by TMS.

4.3.4. Stimulation Waveform Generation

As mentioned above, the time course of the TMS electric field follows the first temporal derivative of the stimulation waveform. It is thus very important to accurately represent the TMS waveform to investigate the temporal interaction of the external electric fields with neurons. For repetitive TMS (rTMS) a TMS pulse train is generated based on the parameters of the rTMS protocol. The user has the option to choose the TMS pulse type, inter-pulse interval, and the number of pulses. We included TMS pulse types commonly used in commercial TMS

machines i.e. monophasic, and biphasic pulses (Kammer et al., 2001). For the monophasic pulse, we created the waveform based on the equations outlined in (Roth and Basser, 1990). The biphasic pulse was created by using the electrophysiological recording of the TMS pulse induced by MagPro X100 TMS machine (MagVenture, Lucernemarken, Denmark). Based on the specified parameters, the pulses are concatenated to generate a pulse train and then written in a file that is used later in the neuron simulation. Note that advanced users can create custom- waveforms e.g. TBS and cTMS (Peterchev et al., 2010) as long as they follow the same format for existing waveforms.

4.3.5. Neuron Model Simulations

In this step, the simulation is run based on the generated NEURON model and the files corresponding to the TMS waveform. During this stage, the user is prompted to choose to use the quasipotentials file calculated previously or to proceed with a uniform electric field. In the latter case, the user should enter the intensity of the electric field and its orientation, either in spherical or Cartesian coordinates. Then, after running the simulation, the output files are automatically created. This includes voltage traces of all neuron segments over time and the coordinates of the segments and their connections. If the user intends to continue the pipeline with modeling calcium dynamics, a MATLAB script converts the NEURON results into file formats that are compatible with the next step.

4.3.6. Calcium Simulations

All necessary components were implemented in the simulation toolbox NeuroBox (Breit et al., 2016). NeuroBox is a simulation toolbox that combines models of electrical and biochemical signaling on one- to three-dimensional computational domains. NeuroBox allows the definition of model equations, typically formulated as ordinary and partial differential equations, of the cellular computational domain and specification of the mathematical discretization methods and solvers (Reiter et al., 2013; Vogel et al., 2013). Built with VRL-Studio (Stepniewski et al., 2019), NeuroBox offers user interface workflow canvases to control the simulation workflow and all biological and numerical parameters. The user can specify simulation parameters for the end time, refinement level, and load the geometry and specify an output location.

Calcium Model Equations

Calcium mobility in the cytosol is described by the diffusion equation

$$\frac{\partial \boldsymbol{u}}{\partial \boldsymbol{t}} = \boldsymbol{\nabla} \cdot (\boldsymbol{D}\boldsymbol{\nabla}\boldsymbol{u}), \quad (2)$$

where $u(x,t)$ is the vector quantity of calcium concentration in the cytosol *[Ca^{2+}]* and *calbindin-D28k*. The diffusion constants *D* are defined using data from (4). The interaction between cytosolic calcium and calbindin-D28k are described by

$$Ca^{2+} + CalB \underset{k_b^-}{\overset{k_b^+}{\leftrightharpoons}} [CalBCa^{2+}] \quad (3)$$

The rate constants k_b^+ and k_b^- are defined in (Breit et al., 2018). The calcium dynamics are modeled by a system of diffusion-reaction equations on a one-dimensional tree geometry with three spatial coordinates, the equations are as follows:

$$\frac{\partial[Ca^{2+}]}{\partial t} = \nabla \cdot (D\nabla[Ca^{2+}]) + k_b^- (b^{tot} - b) - k_b^+ b[Ca^{2+}] \quad (4)$$

$$\frac{\partial[CalB]}{\partial t} = \nabla \cdot (D\nabla[CalB]) + k_b^- (b^{tot} - b) - k_b^+ b[CalB] \quad (5)$$

where the concentration of the CalB-Ca^{2+} compound is expressed by the difference of the total concentration of CalB present in the cytosol (b^{tot}) and free CalB, the former of which is assumed to be constant in space and time (this amounts to the assumption that free calcium and CalB have the same diffusive properties). The parameters used in this study are taken from (Breit et al., 2018).

In order to study the influence of the intracellular organization on Ca^{2+} signals, we include Ca^{2+} exchange mechanisms on the plasma membrane (PM). For the plasma membrane, we consider plasma membrane Ca^{2+} -ATPase pumps (PMCA), Na+/Ca^{2+} exchangers (NCX), calcium release due to voltage-dependent calcium channels (VDCC), and a leakage term. This amounts to the flux equations (number of ions per membrane area and time)

$$j_{pm} = -j_{PMCA} - j_{NCX} + j_l + j_{vdcc} \quad (6)$$

With the Hill equations

$$j_{PMCA} = \rho_{PMCA} \cdot \frac{I_{PMCA} {c_{cyt}}^2}{{K_{PMCA}}^2 + {c_{cyt}}^2} \text{ (7)}$$

$$j_{NCX} = \rho_{NCX} \cdot \frac{I_{NCX} c_{cyt}}{K_{NCX} + c_{cyt}} \text{ (8)}$$

The flux equations for the voltage-dependent calcium channels are given by

$$j_{vdcc} = G(V,t)F(V, \Delta[Ca^{2+}]) \text{ (9)}$$

where *G* is the gating function and *F* is the flux function (Borg-Graham, 1999). Both depend on the voltage at the channel at a particular time *t*. For *F,* $\Delta[Ca^{2+}]$is the difference in the internal and external ion concentration

$$\Delta[Ca^{2+}] \ = \ [Ca^{2+}]_i - [Ca^{2+}]_o \text{ (10)}$$

And

$$f(V, \Delta[Ca^{2+}]) = \bar{p}_{[Ca^{2+}]} \frac{{V_z}^2 F^2}{RT} \cdot \frac{[Ca^{2+}]_i - [Ca^{2+}]_o exp(-zFV/RT)}{1 - exp(-zFV/RT)} \text{ (11)}$$

Where R is the gas constant, F is Faraday's constant, T is in Kelvin, $\bar{p}_{[Ca^{2+}]}$is the permeability of the calcium channel, and z is the valence of the ion (Borg-Graham, 1999).

The gating function *g* is described by a finite product

$$g(V,t) = \sum {x_i}^n (V,t) \text{ (12)}$$

Where $x_i$is the open probability of the gating particle, in this case, it is only calcium, and n is the number of particles. The open probability is described by the ODE

$$\frac{dx}{dt} = \frac{x_\infty(V) - x}{\tau_x(V)} \quad (13)$$

Where x_∞ is the steady-state value of x, and τ_x is the time constant for the particular particle x, formulas are given in (Borg-Graham, 1999).

Numerical Methods for Calcium Simulations

For numerical simulations, the equations are discretized in space using a finite volumes method. Current densities, across the plasma membranes, can be incorporated into the reaction-diffusion process very naturally and easily this way. Time discretization is realized using a backward Euler scheme, i.e., for each point in time t, the term $\frac{\partial \boldsymbol{u}}{\partial \boldsymbol{t}}$ is approximated by

$$\frac{\partial \boldsymbol{u}}{\partial \boldsymbol{t}} \approx \frac{\boldsymbol{u}(\boldsymbol{t}) - \boldsymbol{u}(\boldsymbol{t} - \boldsymbol{\tau})}{\boldsymbol{\tau}} \quad (14)$$

Where τ is the time step size. For the results we present here, the emerging linearized problems were solved using a Bi-CGSTAB (Breit et al., 2018) linear solver preconditioned by an incomplete LU decomposition.

4.3.7. Visualization

Additionally, we have provided a sample script that can generate a video visualizing the 3D distribution of the membrane potentials and the calcium concentrations based on the simulated data from the previous steps. In this procedure, the snapshot of voltage/calcium spatial distribution at each time step is displayed in Gmsh (Geuzaine and Remacle, 2009) and then captured as a video frame. In the end, by concatenating these frames together, a video is created. This

script is capable of visualizing the voltage traces and calcium concentrations separately or next to each other in a single video file for easier comparison. Alternatively, users can visualize the data with Paraview (Ahrens et al., 2005).

4.4. Discussion

We developed an open-source multi-scale modeling toolbox to enable researchers to model the effects of (r)TMS on single neurons and study their cellular and subcellular behavior. *NeMo-TMS* toolbox allows users to simulate the TMS-induced electric fields in geometries of interest (such as an *in vitro* model or a head model), to couple the TMS electric fields to morphologically accurate neuron models, and to simulate the membrane voltage and calcium concentration in the neurons. Our pipeline provides a graphical user interface, as well as an interface to run the process through scripts that will allow researchers with different computational skill sets to efficiently use our software.

To our knowledge, *NeMo-TMS* is the first modeling toolbox that enables studying single neuron behavior under TMS at macro-/mesoscopic, microscopic, and subcellular levels at the same time. Additionally, our toolbox can incorporate sophisticated neuron geometries and morphologies. Complementing modeling results with experimental studies can help to improve our understanding of the basic mechanisms of TMS.

Besides the technical implementation of the pipeline, we discuss several examples to showcase some of its capabilities. In the first example, we simulated the effect

of single-pulse TMS on a morphologically reconstructed neuron embedded inside a tissue culture as an *in vitro* model. We show how the action potential is initiated at the axon terminal from which it propagates to the rest of the neuron. The voltage-dependent calcium concentrations increase after the action potential reaches the soma from which they spread into the dendrites. Both processes occur at different timescales with the calcium propagation following the action potential. In the second example, we compare the neuron response to two classical plasticity-inducing rTMS protocols: a 10 Hz rTMS protocol and a TBS protocol. We show that calcium induction varies between the protocols and that TBS results in a build-up of calcium levels. In the final example, we examine how the neuron response to TMS depends on the orientation of the electric field. For this, we applied a spatially uniform electric field at two orientations and show that the initiation site of the action potential changes as a result as well as the activation threshold. The site of the action potential initiation and the overall field intensity to initiate action potentials are in line with a recent study using morphologically accurate neuron models (Aberra et al., 2020). The differences in action potential initiation also resulted in slight delays in calcium accumulation in the soma. The exact timing between pre- and postsynaptic activity has a major impact on synaptic plasticity (Brzosko et al., 2019; Feldman, 2012; Lenz et al., 2015). It is thus conceivable that in the context of rTMS these effects may add up over the course of several hundred pulses. However, further work is required to test this prediction. Although these examples demonstrate some of the capabilities of this toolbox, its use is not limited

to the examples discussed and researchers have the freedom to apply it to questions of their interest.

While our toolbox significantly advances the field of TMS multi-scale modeling, several further developments can be envisioned. Currently, our pipeline simulates the neuron at rest without spontaneous network-driven or intrinsic activity. Additionally, neurons vary drastically in terms of their biophysics depending on their type. Here, we focused on implementing the biophysics for CA1 pyramidal neurons. Currently, the calcium simulations do not take into account internal calcium stores from the endoplasmic reticulum (ER) and only simulate the calcium release from voltage-dependent calcium channels (VDCCs), sodium-calcium exchangers (NCX), and plasma membrane Ca^{2+} ATPase (PMCA). Future versions of our pipeline can incorporate intrinsic synaptic activity, provide biophysics for more diverse neurons such as cortical neurons, and allow users to define their own biophysics. Further developments can also be implemented to incorporate modeling of the calcium in the ER. Additionally, our toolbox can be expanded to include other non-invasive or invasive brain stimulation techniques such as transcranial Alternating Current Stimulation (tACS), transcranial Direct Current Stimulation (tDCS), or Deep Brain Stimulation (DBS) in the future. Another promising avenue for future developments is modeling the effects of brain stimulation on a network of neurons. One way to achieve this is by combining *NeMo-TMS* with other neuron network modeling frameworks such as the human neocortical neurosolver (Neymotin et al., 2020).

In conclusion, *NeMo-TMS* is a unique tool that provides an easy-to-use platform for multi-scale TMS modeling and enables researchers to incorporate sophisticated modeling approaches into their research.

The neuron model generation codes were implemented by Nicholas Hananeia, Justus-Liebig-University, Germany. The calcium simulation codes were developed by James Rosado, Temple University, USA. The neuron reconstructions were performed by Christos Galanis, University of Freiburg, Freiburg, Germany.

The materials in this chapter are published in the bioRxiv preprint (Shirinpour et al., 2020b).

Chapter 5: Conclusions and Perspectives

> “People do not like to think. If one thinks, one must reach conclusions.”
>
> - Helen Keller

5.1. Conclusions

In chapter 1 of this dissertation, I introduced transcranial magnetic stimulation (TMS) and its significance in the research community and as an alternative therapeutic method for treating psychiatric disorders. Furthermore, I mentioned some of the uncertainties regarding the TMS mechanism of action and why it is difficult to resolve them. Specifically, I focused on the following fundamental questions:

- How does the ongoing neural activity affect the brain’s response to TMS?
- What is the influence of TMS on single neurons?
- Which neurons respond to TMS? Under what circumstances and parameters?
- What is the long-term effect of TMS on neurons?
- What is the role of neuronal subcellular activity on this long-term effect?

In the subsequent chapters, I covered my technical advancements and studies in detail aiming to address these questions.

In chapter 2, a closed-loop TMS-EEG system was developed that is able to record and process the participant's brain activity in real-time and deliver TMS pulses at the desired phase. Since previous studies have suggested that the phase of the alpha oscillation, is a biomarker of local excitability in the brain, we introduced educated temporal prediction (ETP) algorithm that can detect the instantaneous phase of the alpha band from the EEG signal in real-time. We benchmarked the accuracy and computational speed of ETP with the important algorithms proposed previously; autoregressive (AR) and fast Fourier transform (FFT). Results of both *in silico* assessments based on prerecorded EEG datasets and real-time *In vivo* experiments showed that ETP in superior in terms of its accuracy and robustness compared to AR and FFT. Additionally, we reported that ETP is about an order of magnitude faster than the other two methods. Overall, our findings suggest that ETP can be used as a reliable technique to account for the intrinsic neural activity (at least in terms of phase). This allows researchers to study the effects of ongoing brain states on TMS response in the brain. After identifying these dynamics in further detail, closed-loop paradigms can then be incorporated in clinical domains to deliver TMS at the correct brain state in order to maximize the TMS outcome.

Because of the difficulties and limitations inherent to experimental work, In the next studies, I pursued a computational modeling approach. Recent advancements in hardware and software have allowed computational modeling to become a promising tool complementing experimental work. However, it is essential to validate the models and results to ensure reliable findings. Therefore, in chapter

3, I discussed the analytical validation of numerical solutions for TMS-induced electric fields. In the past two decades, great effort has been made to numerically solve the electric fields induced in the geometry of interest by non-invasive brain stimulation. These methods are capable of generating and simulating sophisticated head models based on accurate anatomical images. There have been a few empirical attempts to validate such models, e.g. (Nieminen et al., 2015; Opitz et al., 2014; Petrov et al., 2017), but due to the experimental difficulties, alternative methods of validation are necessary. Due to this motivation, I derived the equations governing the electric fields induced by TMS inside a spherical model. Due to the symmetry of spherical models, the equations can be solved analytically and therefore yield the exact solution. In this study, we compared the analytical solutions to the numerical results of the spherical model solved using the finite element method (FEM). We found similar electric field distributions in both cases. Furthermore, we reported the same pattern for the electric field intensity across spherical models of multiple sizes. In summary, using analytical methods, we validated the accuracy of FEM numerical results for the electric field.

After confirming the accuracy of electric field modeling, in chapter 4 of this dissertation, we extended the modeling framework to investigate the behavior of single neurons and their subcellular activity under TMS. In this study, we combined the state-of-the-art modeling paradigms and developed a novel multi-scale modeling toolbox called Neuron Modeling for TMS (*NeMo-TMS*). This toolbox, allows users to compute the macroscopic/mesoscopic TMS-induced electric fields

in a head model or an *in vitro* model, generate realistic models from morphological reconstructions of neurons, couple the electric fields to the neurons, simulate the membrane voltage of the neurons with the accurate biophysics across time and to calculate the calcium concentrations induced in the neuron induced by voltage-dependent calcium channels. To our knowledge, this study is the first to use a realistic multi-scale modeling pipeline to simulate neuron's behavior at the subcellular scale. Since calcium plays a vital role in synaptic plasticity and long-lasting adaptation of the neuron, our framework facilitates studying the long-term behavior of neurons under TMS fields. Moreover, NeMo-TMS is the first publicly available toolbox capable of multi-scale modeling. Furthermore, our new toolbox provides graphical user interfaces as well as scripting abilities. Therefore, NeMo-TMS can have a major impact on the TMS research due to the novelty, accessibility, and ease of use. Researchers with various expertise can now use our pipeline to explore how neurons react to different parameters, to facilitate their experimental design, and to find explanations for their hypotheses.

Overall, in this dissertation, aiming to address some of the fundamental challenges in the TMS field, I introduced multiple technical developments, mentioned the motivations behind them, provided details of their implementation, and discussed their significance.

5.2. Perspectives

In this section, we discuss some of the limitations of the studies in this dissertation and how future work can improve the findings here.

In the closed-loop TMS-EEG project, we focused on detecting the instantaneous phase of the EEG band of interest as the neural biomarker in real-time. It is expected that novel algorithms and better hardware technologies can enhance the performance of real-time phase detection setups. In addition, many other EEG metrics can be utilized to inform the brain state, such as EEG band powers, TMS evoked potential (TEP) amplitudes, connectivity between brain regions, etc.; or a combination of them. These metrics can be used as biomarkers in a range of neurological disorders including but not limited to epilepsy, depression, Alzheimer's disease (AD), and stroke (de Aguiar Neto and Rosa, 2019; Pitkänen et al., 2016; Stinear, 2017; Tremblay et al., 2019). Furthermore, it is expected that after sufficient advances in our knowledge and technology, brain state-dependent TMS-EEG will become a common treatment method for psychiatric conditions which will improve the performance and the success rate and shorten the treatment duration in patients.

In the multi-scale modeling project, we provided a realistic neuron modeling platform for TMS and extended the modeling paradigm to the subcellular scale for the first time. Yet, many simplifications were made in the first version of NeMo-TMS toolbox. We mainly focused on the activity of single neurons with pyramidal

cell biophysics. Currently, the neurons are silent, since they do not receive synaptic inputs. Furthermore, here we only included calcium concentration as a result of voltage-dependent calcium channels. However, in reality, the biophysics of neurons vary depending on their type, neurons receive input from other neurons, and calcium signaling is mediated by multiple calcium sources, e.g. ionotropic glutamate receptors, nicotinic acetylcholine receptors (nAChR), and internal stores (mostly in the endoplasmic reticulum [ER]) (Grienberger and Konnerth, 2012). Moreover, NeMo-TMS does not account for neural behavior on the network level. Future versions of this toolbox, in combination with upcoming developments in the modeling field, will resolve these shortcomings. It is anticipated that prospective studies will model the detailed physiological behavior of neurons under accurate intrinsic conditions on the single-cell, and the network/system levels. Additionally, future research will model the subcellular activity of the neurons under TMS more accurately and expand our understanding of the long-term changes in the neuronal behavior under the electric fields induced by TMS.

Bibliography

Aberra, A.S., Peterchev, A.V., Grill, W.M., 2018. Biophysically realistic neuron models for simulation of cortical stimulation. J. Neural Eng. 15, 066023. https://doi.org/10.1088/1741-2552/aadbb1

Aberra, A.S., Wang, B., Grill, W.M., Peterchev, A.V., 2020. Simulation of transcranial magnetic stimulation in head model with morphologically-realistic cortical neurons. Brain Stimulation 13, 175–189. https://doi.org/10.1016/j.brs.2019.10.002

Ahrens, J., Geveci, B., Law, C., 2005. 36 - ParaView: An End-User Tool for Large-Data Visualization, in: Hansen, C.D., Johnson, C.R. (Eds.), Visualization Handbook. Butterworth-Heinemann, Burlington, pp. 717–731. https://doi.org/10.1016/B978-012387582-2/50038-1

Alekseichuk, I., Mantell, K., Shirinpour, S., Opitz, A., 2019. Comparative modeling of transcranial magnetic and electric stimulation in mouse, monkey, and human. NeuroImage 194, 136–148. https://doi.org/10.1016/j.neuroimage.2019.03.044

Alekseichuk, I., Shirinpour, S., Opitz, A., 2020. Finite element method (FEM) models for translational research in non-invasive brain stimulation. https://doi.org/10.5281/zenodo.3857041

Alekseichuk, I., Turi, Z., Amador de Lara, G., Antal, A., Paulus, W., 2016. Spatial Working Memory in Humans Depends on Theta and High Gamma Synchronization in the Prefrontal Cortex. Current Biology 26, 1513–1521. https://doi.org/10.1016/j.cub.2016.04.035

Alexander, L.M., Escalera, J., Ai, L., Andreotti, C., Febre, K., Mangone, A., Vega-Potler, N., Langer, N., Alexander, A., Kovacs, M., Litke, S., O'Hagan, B., Andersen, J., Bronstein, B., Bui, A., Bushey, M., Butler, H., Castagna, V., Camacho, N., Chan, E., Citera, D., Clucas, J., Cohen, S., Dufek, S., Eaves, M., Fradera, B., Gardner, J., Grant-Villegas, N., Green, G., Gregory, C., Hart, E., Harris, S., Horton, M., Kahn, D., Kabotyanski, K., Karmel, B., Kelly, S.P., Kleinman, K., Koo, B., Kramer, E., Lennon, E., Lord, C., Mantello, G., Margolis, A., Merikangas, K.R., Milham, J., Minniti, G., Neuhaus, R., Levine, A., Osman, Y., Parra, L.C., Pugh, K.R., Racanello, A., Restrepo, A., Saltzman, T., Septimus, B., Tobe, R., Waltz, R., Williams, A., Yeo, A., Castellanos, F.X., Klein, A., Paus, T., Leventhal, B.L., Craddock, R.C., Koplewicz, H.S., Milham, M.P., 2017. An open resource for transdiagnostic research in pediatric mental health and learning disorders. Scientific Data 4, 170181. https://doi.org/10.1038/sdata.2017.181

Allen, E.A., Pasley, B.N., Duong, T., Freeman, R.D., 2007. Transcranial Magnetic Stimulation Elicits Coupled Neural and Hemodynamic Consequences. Science 317, 1918–1921. https://doi.org/10.1126/science.1146426

Amunts, K., Zilles, K., 2015. Architectonic Mapping of the Human Brain beyond Brodmann. Neuron 88, 1086–1107. https://doi.org/10.1016/j.neuron.2015.12.001

Avery, D.H., Holtzheimer, P.E., Fawaz, W., Russo, J., Neumaier, J., Dunner, D.L., Haynor, D.R., Claypoole, K.H., Wajdik, C., Roy-Byrne, P., 2006. A Controlled Study of Repetitive Transcranial Magnetic Stimulation in Medication-Resistant Major Depression. Biological Psychiatry 59, 187–194. https://doi.org/10.1016/j.biopsych.2005.07.003

Azevedo, F.A.C., Carvalho, L.R.B., Grinberg, L.T., Farfel, J.M., Ferretti, R.E.L., Leite, R.E.P., Filho, W.J., Lent, R., Herculano-Houzel, S., 2009. Equal numbers of neuronal and nonneuronal cells make the human brain an isometrically scaled-up primate brain. Journal of Comparative Neurology 513, 532–541. https://doi.org/10.1002/cne.21974

Barker, A.T., Jalinous, R., Freeston, I.L., 1985. NON-INVASIVE MAGNETIC STIMULATION OF HUMAN MOTOR CORTEX. The Lancet, Originally published as Volume 1, Issue 8437 325, 1106–1107. https://doi.org/10.1016/S0140-6736(85)92413-4

Basser, P.J., Roth, B.J., 1991. Stimulation of a myelinated nerve axon by electromagnetic induction. Med. Biol. Eng. Comput. 29, 261–268. https://doi.org/10.1007/BF02446708

Beining, M., Mongiat, L.A., Schwarzacher, S.W., Cuntz, H., Jedlicka, P., 2017. T2N as a new tool for robust electrophysiological modeling demonstrated for mature and adult-born dentate granule cells. eLife 6, e26517. https://doi.org/10.7554/eLife.26517

Berger, B., Minarik, T., Liuzzi, G., Hummel, F.C., Sauseng, P., 2014. EEG Oscillatory Phase-Dependent Markers of Corticospinal Excitability in the Resting Brain [WWW Document]. BioMed Research International. https://doi.org/10.1155/2014/936096

Bergmann, T.O., Karabanov, A., Hartwigsen, G., Thielscher, A., Siebner, H.R., 2016. Combining non-invasive transcranial brain stimulation with neuroimaging and electrophysiology: Current approaches and future perspectives. NeuroImage, Transcranial electric stimulation (tES) and Neuroimaging 140, 4–19. https://doi.org/10.1016/j.neuroimage.2016.02.012

Bezprozvanny, I., 2009. Calcium signaling and neurodegenerative diseases. Trends in Molecular Medicine 15, 89–100. https://doi.org/10.1016/j.molmed.2009.01.001

Bezprozvanny, I., Hayden, M.R., 2004. Deranged neuronal calcium signaling and Huntington disease. Biochemical and Biophysical Research Communications 322, 1310–1317. https://doi.org/10.1016/j.bbrc.2004.08.035

Borg-Graham, L.J., 1999. Interpretations of Data and Mechanisms for Hippocampal Pyramidal Cell Models, in: Ulinski, P.S., Jones, E.G., Peters,

A. (Eds.), Models of Cortical Circuits, Cerebral Cortex. Springer US, Boston, MA, pp. 19–138. https://doi.org/10.1007/978-1-4615-4903-1_2

BrainsWay, 2020. BrainsWay Receives FDA Clearance for Smoking Addiction in Adults [WWW Document]. BrainsWay. URL https://www.brainsway.com/news_events/brainsway-receives-fda-clearance-for-smoking-addiction-in-adults/ (accessed 9.19.20).

Breit, M., Kessler, M., Stepniewski, M., Vlachos, A., Queisser, G., 2018. Spine-to-Dendrite Calcium Modeling Discloses Relevance for Precise Positioning of Ryanodine Receptor-Containing Spine Endoplasmic Reticulum. Scientific Reports 8, 15624. https://doi.org/10.1038/s41598-018-33343-9

Breit, M., Queisser, G., 2018. What Is Required for Neuronal Calcium Waves? A Numerical Parameter Study. The Journal of Mathematical Neuroscience 8, 9. https://doi.org/10.1186/s13408-018-0064-x

Breit, M., Stepniewski, M., Grein, S., Gottmann, P., Reinhardt, L., Queisser, G., 2016. Anatomically Detailed and Large-Scale Simulations Studying Synapse Loss and Synchrony Using NeuroBox. Front. Neuroanat. 10. https://doi.org/10.3389/fnana.2016.00008

Brzosko, Z., Mierau, S.B., Paulsen, O., 2019. Neuromodulation of Spike-Timing-Dependent Plasticity: Past, Present, and Future. Neuron 103, 563–581. https://doi.org/10.1016/j.neuron.2019.05.041

Buzsáki, G., Anastassiou, C.A., Koch, C., 2012. The origin of extracellular fields and currents — EEG, ECoG, LFP and spikes. Nature Reviews Neuroscience 13, 407–420. https://doi.org/10.1038/nrn3241

Buzsáki, G., Draguhn, A., 2004. Neuronal Oscillations in Cortical Networks. Science 304, 1926–1929. https://doi.org/10.1126/science.1099745

Castrillon, G., Sollmann, N., Kurcyus, K., Razi, A., Krieg, S.M., Riedl, V., 2020. The physiological effects of noninvasive brain stimulation fundamentally differ across the human cortex. Science Advances 6, eaay2739. https://doi.org/10.1126/sciadv.aay2739

Chan, C.S., Gertler, T.S., Surmeier, D.J., 2009. Calcium homeostasis, selective vulnerability and Parkinson's disease. Trends in Neurosciences 32, 249–256. https://doi.org/10.1016/j.tins.2009.01.006

Chen, L.L., Madhavan, R., Rapoport, B.I., Anderson, W.S., 2013. Real-time brain oscillation detection and phase-locked stimulation using autoregressive spectral estimation and time-series forward prediction. IEEE Transactions on Biomedical Engineering 60, 753–762. https://doi.org/10.1109/TBME.2011.2109715

Cheung, K.-H., Shineman, D., Müller, M., Cárdenas, C., Mei, L., Yang, J., Tomita, T., Iwatsubo, T., Lee, V.M.-Y., Foskett, J.K., 2008. Mechanism of Ca2+ Disruption in Alzheimer's Disease by Presenilin Regulation of InsP3 Receptor Channel Gating. Neuron 58, 871–883. https://doi.org/10.1016/j.neuron.2008.04.015

Cole, S.R., Voytek, B., 2017. Brain Oscillations and the Importance of Waveform Shape. Trends in Cognitive Sciences 21, 137–149. https://doi.org/10.1016/j.tics.2016.12.008

Commissioner, O. of the, 2020a. FDA permits marketing of first medical device for treatment of ADHD [WWW Document]. FDA. URL https://www.fda.gov/news-events/press-announcements/fda-permits-marketing-first-medical-device-treatment-adhd (accessed 9.19.20).

Commissioner, O. of the, 2020b. FDA permits marketing of transcranial magnetic stimulation for treatment of obsessive compulsive disorder [WWW Document]. FDA. URL https://www.fda.gov/news-events/press-announcements/fda-permits-marketing-transcranial-magnetic-stimulation-treatment-obsessive-compulsive-disorder (accessed 9.19.20).

de Aguiar Neto, F.S., Rosa, J.L.G., 2019. Depression biomarkers using non-invasive EEG: A review. Neuroscience & Biobehavioral Reviews 105, 83–93. https://doi.org/10.1016/j.neubiorev.2019.07.021

DeFelipe, J., Hendry, S.H.C., Hashikawa, T., Molinari, M., Jones, E.G., 1990. A microcolumnar structure of monkey cerebral cortex revealed by immunocytochemical studies of double bouquet cell axons. Neuroscience 37, 655–673. https://doi.org/10.1016/0306-4522(90)90097-N

Delorme, A., Makeig, S., 2004. EEGLAB: an open source toolbox for analysis of single-trial EEG dynamics including independent component analysis. Journal of Neuroscience Methods 134, 9–21. https://doi.org/10.1016/j.jneumeth.2003.10.009

Deng, Z.-D., Lisanby, S.H., Peterchev, A.V., 2013. Electric field depth–focality tradeoff in transcranial magnetic stimulation: Simulation comparison of 50 coil designs. Brain Stimulation 6, 1–13. https://doi.org/10.1016/j.brs.2012.02.005

Di Lazzaro, V., Rothwell, J., Capogna, M., 2018. Noninvasive Stimulation of the Human Brain: Activation of Multiple Cortical Circuits. Neuroscientist 24, 246–260. https://doi.org/10.1177/1073858417717660

Dugué, L., Marque, P., VanRullen, R., 2011. The Phase of Ongoing Oscillations Mediates the Causal Relation between Brain Excitation and Visual Perception. J. Neurosci. 31, 11889–11893. https://doi.org/10.1523/JNEUROSCI.1161-11.2011

Eaton, H., 1992. Electric field induced in a spherical volume conductor from arbitrary coils: application to magnetic stimulation and MEG. Medical & biological engineering & computing 30, 433–40. https://doi.org/10.1007/BF02446182

Eilers, J., Callewaert, G., Armstrong, C., Konnerth, A., 1995. Calcium signaling in a narrow somatic submembrane shell during synaptic activity in cerebellar Purkinje neurons. PNAS 92, 10272–10276. https://doi.org/10.1073/pnas.92.22.10272

Feldman, D.E., 2012. The Spike-Timing Dependence of Plasticity. Neuron 75, 556–571. https://doi.org/10.1016/j.neuron.2012.08.001

Fingelkurts, Alexander A., Fingelkurts, Andrew A., 2015. Altered Structure of Dynamic Electroencephalogram Oscillatory Pattern in Major Depression. Biological Psychiatry, Cortical Oscillations for Cognitive/Circuit Dysfunction in Psychiatric Disorders 77, 1050–1060. https://doi.org/10.1016/j.biopsych.2014.12.011

Geuzaine, C., Remacle, J.-F., 2009. Gmsh: A 3-D finite element mesh generator with built-in pre- and post-processing facilities. International Journal for Numerical Methods in Engineering 79, 1309–1331. https://doi.org/10.1002/nme.2579

Goodwin, B.D., Butson, C.R., 2015. Subject-Specific Multiscale Modeling to Investigate Effects of Transcranial Magnetic Stimulation. Neuromodulation: Technology at the Neural Interface 18, 694–704. https://doi.org/10.1111/ner.12296

Green, K.N., LaFerla, F.M., 2008. Linking Calcium to Aβ and Alzheimer's Disease. Neuron 59, 190–194. https://doi.org/10.1016/j.neuron.2008.07.013

Grienberger, C., Konnerth, A., 2012. Imaging Calcium in Neurons. Neuron 73, 862–885. https://doi.org/10.1016/j.neuron.2012.02.011

Groppa, S., Oliviero, A., Eisen, A., Quartarone, A., Cohen, L.G., Mall, V., Kaelin-Lang, A., Mima, T., Rossi, S., Thickbroom, G.W., Rossini, P.M., Ziemann, U., Valls-Solé, J., Siebner, H.R., 2012. A practical guide to diagnostic transcranial magnetic stimulation: Report of an IFCN committee. Clin Neurophysiol 123, 858–882. https://doi.org/10.1016/j.clinph.2012.01.010

Hallett, M., 2007. Transcranial Magnetic Stimulation: A Primer. Neuron 55, 187–199. https://doi.org/10.1016/j.neuron.2007.06.026

Hanakawa, T., Mima, T., Matsumoto, R., Abe, M., Inouchi, M., Urayama, S., Anami, K., Honda, M., Fukuyama, H., 2009. Stimulus–Response Profile during Single-Pulse Transcranial Magnetic Stimulation to the Primary Motor Cortex. Cereb Cortex 19, 2605–2615. https://doi.org/10.1093/cercor/bhp013

Hannah, R., Rothwell, J.C., 2017. Pulse Duration as Well as Current Direction Determines the Specificity of Transcranial Magnetic Stimulation of Motor Cortex during Contraction. Brain Stimulation 10, 106–115. https://doi.org/10.1016/j.brs.2016.09.008

Herring, J.D., Thut, G., Jensen, O., Bergmann, T.O., 2015. Attention Modulates TMS-Locked Alpha Oscillations in the Visual Cortex. J. Neurosci. 35, 14435–14447. https://doi.org/10.1523/JNEUROSCI.1833-15.2015

Hines, M.L., Carnevale, N.T., 1997. The NEURON Simulation Environment. Neural Computation 9, 1179–1209. https://doi.org/10.1162/neco.1997.9.6.1179

Hjorth, B., 1980. Source Derivation Simplifies Topographical EEG Interpretation. American Journal of EEG Technology 20, 121–132. https://doi.org/10.1080/00029238.1980.11080015

Hoogendam, J.M., Ramakers, G.M.J., Di Lazzaro, V., 2010. Physiology of repetitive transcranial magnetic stimulation of the human brain. Brain Stimulation 3, 95–118. https://doi.org/10.1016/j.brs.2009.10.005

Hoppenrath, K., Funke, K., 2013. Time-course of changes in neuronal activity markers following iTBS-TMS of the rat neocortex. Neuroscience Letters 536, 19–23. https://doi.org/10.1016/j.neulet.2013.01.003

Horvath, J.C., Perez, J.M., Forrow, L., Fregni, F., Pascual-Leone, A., 2011. Transcranial magnetic stimulation: a historical evaluation and future prognosis of therapeutically relevant ethical concerns. Journal of Medical Ethics 37, 137–143. https://doi.org/10.1136/jme.2010.039966

Huang, Y., Liu, A.A., Lafon, B., Friedman, D., Dayan, M., Wang, X., Bikson, M., Doyle, W.K., Devinsky, O., Parra, L.C., 2017. Measurements and models of electric fields in the in vivo human brain during transcranial electric stimulation. eLife 6, e18834. https://doi.org/10.7554/eLife.18834

Huang, Y.-Z., Edwards, M.J., Rounis, E., Bhatia, K.P., Rothwell, J.C., 2005. Theta Burst Stimulation of the Human Motor Cortex. Neuron 45, 201–206. https://doi.org/10.1016/j.neuron.2004.12.033

Hussain, S.J., Claudino, L., Bönstrup, M., Norato, G., Cruciani, G., Thompson, R., Zrenner, C., Ziemann, U., Buch, E., Cohen, L.G., 2019. Sensorimotor Oscillatory Phase–Power Interaction Gates Resting Human Corticospinal Output. Cereb Cortex 29, 3766–3777. https://doi.org/10.1093/cercor/bhy255

Ilmoniemi, R.J., Kičić, D., 2009. Methodology for Combined TMS and EEG. Brain Topogr 22, 233. https://doi.org/10.1007/s10548-009-0123-4

Jacobs, J., Kahana, M.J., Ekstrom, A.D., Fried, I., 2007. Brain Oscillations Control Timing of Single-Neuron Activity in Humans. J. Neurosci. 27, 3839–3844. https://doi.org/10.1523/JNEUROSCI.4636-06.2007

Jarsky, T., Roxin, A., Kath, W.L., Spruston, N., 2005. Conditional dendritic spike propagation following distal synaptic activation of hippocampal CA1 pyramidal neurons. Nature Neuroscience 8, 1667–1676. https://doi.org/10.1038/nn1599

Kadosh, R.C., Elliott, P., 2013. Brain stimulation has a long history. Nature 500, 529–529. https://doi.org/10.1038/500529d

Kamitani, Y., Bhalodia, V.M., Kubota, Y., Shimojo, S., 2001. A model of magnetic stimulation of neocortical neurons. Neurocomputing, Computational Neuroscience: Trends in Research 2001 38–40, 697–703. https://doi.org/10.1016/S0925-2312(01)00447-7

Kammer, T., Beck, S., Thielscher, A., Laubis-Herrmann, U., Topka, H., 2001. Motor thresholds in humans: a transcranial magnetic stimulation study comparing different pulse waveforms, current directions and stimulator types. Clinical Neurophysiology 112, 250–258. https://doi.org/10.1016/S1388-2457(00)00513-7

Kar, K., Duijnhouwer, J., Krekelberg, B., 2017. Transcranial Alternating Current Stimulation Attenuates Neuronal Adaptation. J. Neurosci. 37, 2325–2335. https://doi.org/10.1523/JNEUROSCI.2266-16.2016

Karabanov, A., Thielscher, A., Siebner, H.R., 2016. Transcranial brain stimulation: closing the loop between brain and stimulation. Current Opinion in Neurology 29, 397. https://doi.org/10.1097/WCO.0000000000000342

Keil, J., Timm, J., SanMiguel, I., Schulz, H., Obleser, J., Schönwiesner, M., 2013. Cortical brain states and corticospinal synchronization influence TMS-evoked motor potentials. Journal of Neurophysiology 111, 513–519. https://doi.org/10.1152/jn.00387.2013

Komssi, S., Kähkönen, S., Ilmoniemi, R.J., 2004. The effect of stimulus intensity on brain responses evoked by transcranial magnetic stimulation. Human Brain Mapping 21, 154–164. https://doi.org/10.1002/hbm.10159

Krause, M.R., Zanos, T.P., Csorba, B.A., Pilly, P.K., Choe, J., Phillips, M.E., Datta, A., Pack, C.C., 2017. Transcranial Direct Current Stimulation Facilitates Associative Learning and Alters Functional Connectivity in the Primate Brain. Current Biology 27, 3086-3096.e3. https://doi.org/10.1016/j.cub.2017.09.020

Krusienski, D.J., McFarland, D.J., Wolpaw, J.R., 2006. An Evaluation of Autoregressive Spectral Estimation Model Order for Brain-Computer Interface Applications, in: 2006 International Conference of the IEEE Engineering in Medicine and Biology Society. Presented at the 2006 International Conference of the IEEE Engineering in Medicine and Biology Society, pp. 1323–1326. https://doi.org/10.1109/IEMBS.2006.259822

Laakso, I., Hirata, A., Ugawa, Y., 2013. Effects of coil orientation on the electric field induced by TMS over the hand motor area. Phys. Med. Biol. 59, 203–218. https://doi.org/10.1088/0031-9155/59/1/203

Lefaucheur, J.-P., André-Obadia, N., Antal, A., Ayache, S.S., Baeken, C., Benninger, D.H., Cantello, R.M., Cincotta, M., de Carvalho, M., De Ridder, D., Devanne, H., Di Lazzaro, V., Filipović, S.R., Hummel, F.C., Jääskeläinen, S.K., Kimiskidis, V.K., Koch, G., Langguth, B., Nyffeler, T., Oliviero, A., Padberg, F., Poulet, E., Rossi, S., Rossini, P.M., Rothwell, J.C., Schönfeldt-Lecuona, C., Siebner, H.R., Slotema, C.W., Stagg, C.J., Valls-Sole, J., Ziemann, U., Paulus, W., Garcia-Larrea, L., 2014. Evidence-based guidelines on the therapeutic use of repetitive transcranial magnetic stimulation (rTMS). Clinical Neurophysiology 125, 2150–2206. https://doi.org/10.1016/j.clinph.2014.05.021

Lenz, M., Galanis, C., Müller-Dahlhaus, F., Opitz, A., Wierenga, C.J., Szabó, G., Ziemann, U., Deller, T., Funke, K., Vlachos, A., 2016. Repetitive magnetic stimulation induces plasticity of inhibitory synapses. Nature Communications 7, 10020. https://doi.org/10.1038/ncomms10020

Lenz, M., Platschek, S., Priesemann, V., Becker, D., Willems, L.M., Ziemann, U., Deller, T., Müller-Dahlhaus, F., Jedlicka, P., Vlachos, A., 2015. Repetitive magnetic stimulation induces plasticity of excitatory postsynapses on

proximal dendrites of cultured mouse CA1 pyramidal neurons. Brain Struct Funct 220, 3323–3337. https://doi.org/10.1007/s00429-014-0859-9
Leuchter, A.F., Hunter, A.M., Krantz, D.E., Cook, I.A., 2015. Rhythms and blues: modulation of oscillatory synchrony and the mechanism of action of antidepressant treatments. Annals of the New York Academy of Sciences 1344, 78–91. https://doi.org/10.1111/nyas.12742
Limbäck-Stokin, K., Korzus, E., Nagaoka-Yasuda, R., Mayford, M., 2004. Nuclear Calcium/Calmodulin Regulates Memory Consolidation. J. Neurosci. 24, 10858–10867. https://doi.org/10.1523/JNEUROSCI.1022-04.2004
Madsen, K.H., Karabanov, A.N., Krohne, L.G., Safeldt, M.G., Tomasevic, L., Siebner, H.R., 2019. No trace of phase: Corticomotor excitability is not tuned by phase of pericentral mu-rhythm. Brain Stimulation 12, 1261–1270. https://doi.org/10.1016/j.brs.2019.05.005
Mäkinen, V.T., May, P.J.C., Tiitinen, H., 2005. The use of stationarity and nonstationarity in the detection and analysis of neural oscillations. NeuroImage 28, 389–400. https://doi.org/10.1016/j.neuroimage.2005.06.004
Mansouri, F., Dunlop, K., Giacobbe, P., Downar, J., Zariffa, J., 2017. A Fast EEG Forecasting Algorithm for Phase-Locked Transcranial Electrical Stimulation of the Human Brain. Front. Neurosci. 11. https://doi.org/10.3389/fnins.2017.00401
Maris, E., Fries, P., van Ede, F., 2016. Diverse Phase Relations among Neuronal Rhythms and Their Potential Function. Trends in Neurosciences 39, 86–99. https://doi.org/10.1016/j.tins.2015.12.004
Mattson, M.P., Cheng, B., Davis, D., Bryant, K., Lieberburg, I., Rydel, R.E., 1992. beta-Amyloid peptides destabilize calcium homeostasis and render human cortical neurons vulnerable to excitotoxicity. J. Neurosci. 12, 376–389. https://doi.org/10.1523/JNEUROSCI.12-02-00376.1992
McFarland, D.J., Wolpaw, J.R., 2008. Sensorimotor rhythm-based brain–computer interface (BCI): model order selection for autoregressive spectral analysis. J. Neural Eng. 5, 155–162. https://doi.org/10.1088/1741-2560/5/2/006
McIntosh, J.R., Sajda, P., 2019. Estimation of phase in EEG rhythms for real-time applications. arXiv:1910.08784 [eess, q-bio].
Miranda, P.C., Callejón-Leblic, M.A., Salvador, R., Ruffini, G., 2018. Realistic modeling of transcranial current stimulation: The electric field in the brain. Current Opinion in Biomedical Engineering, Neural Engineering/ Novel Biomedical Technologies: Neuromodulation 8, 20–27. https://doi.org/10.1016/j.cobme.2018.09.002
Miranda, P.C., Hallett, M., Basser, P.J., 2003. The electric field induced in the brain by magnetic stimulation: a 3-D finite-element analysis of the effect of tissue heterogeneity and anisotropy. IEEE Transactions on Biomedical Engineering 50, 1074–1085. https://doi.org/10.1109/TBME.2003.816079
Mountcastle, V.B., 1997. The columnar organization of the neocortex. Brain 120, 701–722. https://doi.org/10.1093/brain/120.4.701

Mueller, J.K., Grigsby, E.M., Prevosto, V., Petraglia, F.W., Rao, H., Deng, Z.-D., Peterchev, A.V., Sommer, M.A., Egner, T., Platt, M.L., Grill, W.M., 2014. Simultaneous transcranial magnetic stimulation and single-neuron recording in alert non-human primates. Nature Neuroscience 17, 1130–1136. https://doi.org/10.1038/nn.3751

Nagarajan, S.S., Durand, D.M., 1996. A generalized cable equation for magnetic stimulation of axons. IEEE Transactions on Biomedical Engineering 43, 304–312. https://doi.org/10.1109/10.486288

Neymotin, S.A., Daniels, D.S., Caldwell, B., McDougal, R.A., Carnevale, N.T., Jas, M., Moore, C.I., Hines, M.L., Hämäläinen, M., Jones, S.R., 2020. Human Neocortical Neurosolver (HNN), a new software tool for interpreting the cellular and network origin of human MEG/EEG data. eLife 9, e51214. https://doi.org/10.7554/eLife.51214

Nieminen, J.O., Koponen, L.M., Ilmoniemi, R.J., 2015. Experimental Characterization of the Electric Field Distribution Induced by TMS Devices. Brain Stimulation 8, 582–589. https://doi.org/10.1016/j.brs.2015.01.004

Nummenmaa, A., Stenroos, M., Ilmoniemi, R.J., Okada, Y.C., Hämäläinen, M.S., Raij, T., 2013. Comparison of spherical and realistically shaped boundary element head models for transcranial magnetic stimulation navigation. Clinical Neurophysiology 124, 1995–2007. https://doi.org/10.1016/j.clinph.2013.04.019

Oostenveld, R., Fries, P., Maris, E., Schoffelen, J.-M., 2010. FieldTrip: Open Source Software for Advanced Analysis of MEG, EEG, and Invasive Electrophysiological Data. Computational Intelligence and Neuroscience 2011, e156869. https://doi.org/10.1155/2011/156869

Opitz, A., Falchier, A., Yan, C.-G., Yeagle, E.M., Linn, G.S., Megevand, P., Thielscher, A., A, R.D., Milham, M.P., Mehta, A.D., Schroeder, C.E., 2016. Spatiotemporal structure of intracranial electric fields induced by transcranial electric stimulation in humans and nonhuman primates. Scientific Reports 6, 31236. https://doi.org/10.1038/srep31236

Opitz, A., Legon, W., Rowlands, A., Bickel, W.K., Paulus, W., Tyler, W.J., 2013. Physiological observations validate finite element models for estimating subject-specific electric field distributions induced by transcranial magnetic stimulation of the human motor cortex. NeuroImage 81, 253–264. https://doi.org/10.1016/j.neuroimage.2013.04.067

Opitz, A., Paulus, W., Will, S., Antunes, A., Thielscher, A., 2015. Determinants of the electric field during transcranial direct current stimulation. NeuroImage 109, 140–150. https://doi.org/10.1016/j.neuroimage.2015.01.033

Opitz, A., Windhoff, M., Heidemann, R.M., Turner, R., Thielscher, A., 2011. How the brain tissue shapes the electric field induced by transcranial magnetic stimulation. NeuroImage 58, 849–859. https://doi.org/10.1016/j.neuroimage.2011.06.069

Opitz, A., Yeagle, E., Thielscher, A., Schroeder, C., Mehta, A.D., Milham, M.P., 2018. On the importance of precise electrode placement for targeted

transcranial electric stimulation. NeuroImage 181, 560–567. https://doi.org/10.1016/j.neuroimage.2018.07.027

Opitz, A., Zafar, N., Bockermann, V., Rohde, V., Paulus, W., 2014. Validating computationally predicted TMS stimulation areas using direct electrical stimulation in patients with brain tumors near precentral regions. NeuroImage: Clinical 4, 500–507. https://doi.org/10.1016/j.nicl.2014.03.004

O'Reardon, J.P., Solvason, H.B., Janicak, P.G., Sampson, S., Isenberg, K.E., Nahas, Z., McDonald, W.M., Avery, D., Fitzgerald, P.B., Loo, C., Demitrack, M.A., George, M.S., Sackeim, H.A., 2007. Efficacy and Safety of Transcranial Magnetic Stimulation in the Acute Treatment of Major Depression: A Multisite Randomized Controlled Trial. Biological Psychiatry, Depression: New Perspectives on Treatment and Etiology 62, 1208–1216. https://doi.org/10.1016/j.biopsych.2007.01.018

Ozdemir, R.A., Tadayon, E., Boucher, P., Momi, D., Karakhanyan, K.A., Fox, M.D., Halko, M.A., Pascual-Leone, A., Shafi, M.M., Santarnecchi, E., 2020. Individualized perturbation of the human connectome reveals reproducible biomarkers of network dynamics relevant to cognition. Proc Natl Acad Sci USA 201911240. https://doi.org/10.1073/pnas.1911240117

Pakkenberg, B., Pelvig, D., Marner, L., Bundgaard, M.J., Gundersen, H.J.G., Nyengaard, J.R., Regeur, L., 2003. Aging and the human neocortex. Experimental Gerontology, Proceedings of the 6th International Symposium on the Neurobiology and Neuroendocrinology of Aging 38, 95–99. https://doi.org/10.1016/S0531-5565(02)00151-1

Pashut, T., Wolfus, S., Friedman, A., Lavidor, M., Bar-Gad, I., Yeshurun, Y., Korngreen, A., 2011. Mechanisms of Magnetic Stimulation of Central Nervous System Neurons. PLOS Computational Biology 7, e1002022. https://doi.org/10.1371/journal.pcbi.1002022

Pasley, B.N., Allen, E.A., Freeman, R.D., 2009. State-Dependent Variability of Neuronal Responses to Transcranial Magnetic Stimulation of the Visual Cortex. Neuron 62, 291–303. https://doi.org/10.1016/j.neuron.2009.03.012

Perera, T., George, M.S., Grammer, G., Janicak, P.G., Pascual-Leone, A., Wirecki, T.S., 2016. The Clinical TMS Society Consensus Review and Treatment Recommendations for TMS Therapy for Major Depressive Disorder. Brain Stimulation 9, 336–346. https://doi.org/10.1016/j.brs.2016.03.010

Peterchev, A.V., Murphy, D.L., Lisanby, S.H., 2010. Repetitive transcranial magnetic stimulator with controllable pulse parameters (cTMS), in: 2010 Annual International Conference of the IEEE Engineering in Medicine and Biology. Presented at the 2010 Annual International Conference of the IEEE Engineering in Medicine and Biology, pp. 2922–2926. https://doi.org/10.1109/IEMBS.2010.5626287

Peterchev, A.V., Wagner, T.A., Miranda, P.C., Nitsche, M.A., Paulus, W., Lisanby, S.H., Pascual-Leone, A., Bikson, M., 2012. Fundamentals of transcranial electric and magnetic stimulation dose: Definition, selection, and reporting

practices. Brain Stimulation 5, 435–453. https://doi.org/10.1016/j.brs.2011.10.001
Petrov, P.I., Mandija, S., Sommer, I.E.C., Berg, C.A.T. van den, Neggers, S.F.W., 2017. How much detail is needed in modeling a transcranial magnetic stimulation figure-8 coil: Measurements and brain simulations. PLOS ONE 12, e0178952. https://doi.org/10.1371/journal.pone.0178952
Pitkänen, A., Löscher, W., Vezzani, A., Becker, A.J., Simonato, M., Lukasiuk, K., Gröhn, O., Bankstahl, J.P., Friedman, A., Aronica, E., Gorter, J.A., Ravizza, T., Sisodiya, S.M., Kokaia, M., Beck, H., 2016. Advances in the development of biomarkers for epilepsy. The Lancet Neurology 15, 843–856. https://doi.org/10.1016/S1474-4422(16)00112-5
Plonsey, R., 1969. Bioelectric Phenomena. McGraw-Hill, New York, NY.
Plonsey, R., Heppner, D.B., 1967. Considerations of quasi-stationarity in electrophysiological systems. Bulletin of Mathematical Biophysics 29, 657–664. https://doi.org/10.1007/BF02476917
Polanía, R., Nitsche, M.A., Ruff, C.C., 2018. Studying and modifying brain function with non-invasive brain stimulation. Nature Neuroscience 21, 174–187. https://doi.org/10.1038/s41593-017-0054-4
Radman, T., Ramos, R.L., Brumberg, J.C., Bikson, M., 2009. Role of cortical cell type and morphology in subthreshold and suprathreshold uniform electric field stimulation in vitro. Brain Stimulation 2, 215-228.e3. https://doi.org/10.1016/j.brs.2009.03.007
Rall, W., 1989. Cable theory for dendritic neurons, in: Methods in Neuronal Modeling. MIT Press, Cambridge, MA, pp. 8–62.
Reiter, S., Vogel, A., Heppner, I., Rupp, M., Wittum, G., 2013. A massively parallel geometric multigrid solver on hierarchically distributed grids. Comput. Visual Sci. 16, 151–164. https://doi.org/10.1007/s00791-014-0231-x
Romei, V., Brodbeck, V., Michel, C., Amedi, A., Pascual-Leone, A., Thut, G., 2008. Spontaneous Fluctuations in Posterior α-Band EEG Activity Reflect Variability in Excitability of Human Visual Areas. Cereb Cortex 18, 2010–2018. https://doi.org/10.1093/cercor/bhm229
Romero, M.C., Davare, M., Armendariz, M., Janssen, P., 2019. Neural effects of transcranial magnetic stimulation at the single-cell level. Nature Communications 10, 2642. https://doi.org/10.1038/s41467-019-10638-7
Rossi, S., Hallett, M., Rossini, P.M., Pascual-Leone, A., Safety of TMS Consensus Group, 2009. Safety, ethical considerations, and application guidelines for the use of transcranial magnetic stimulation in clinical practice and research. Clin Neurophysiol 120, 2008–2039. https://doi.org/10.1016/j.clinph.2009.08.016
Roth, B.J., Basser, P.J., 1990. A model of the stimulation of a nerve fiber by electromagnetic induction. IEEE Transactions on Biomedical Engineering 37, 588–597. https://doi.org/10.1109/10.55662
Salinas, F.S., Lancaster, J.L., Fox, P.T., 2009. 3D modeling of the total electric field induced by transcranial magnetic stimulation using the boundary

element method. Phys. Med. Biol. 54, 3631–3647. https://doi.org/10.1088/0031-9155/54/12/002
Salvador, R., Silva, S., Basser, P.J., Miranda, P.C., 2011. Determining which mechanisms lead to activation in the motor cortex: A modeling study of transcranial magnetic stimulation using realistic stimulus waveforms and sulcal geometry. Clinical Neurophysiology 122, 748–758. https://doi.org/10.1016/j.clinph.2010.09.022
Saturnino, G.B., Madsen, K.H., Thielscher, A., 2019a. Electric field simulations for transcranial brain stimulation using FEM: an efficient implementation and error analysis. J. Neural Eng. 16, 066032. https://doi.org/10.1088/1741-2552/ab41ba
Saturnino, G.B., Puonti, O., Nielsen, J.D., Antonenko, D., Madsen, K.H., Thielscher, A., 2019b. SimNIBS 2.1: A Comprehensive Pipeline for Individualized Electric Field Modelling for Transcranial Brain Stimulation, in: Makarov, S., Horner, M., Noetscher, G. (Eds.), Brain and Human Body Modeling: Computational Human Modeling at EMBC 2018. Springer International Publishing, Cham, pp. 3–25. https://doi.org/10.1007/978-3-030-21293-3_1
Sauseng, P., Klimesch, W., 2008. What does phase information of oscillatory brain activity tell us about cognitive processes? Neuroscience & Biobehavioral Reviews 32, 1001–1013. https://doi.org/10.1016/j.neubiorev.2008.03.014
Schroeder, C.E., Lakatos, P., 2009. Low-frequency neuronal oscillations as instruments of sensory selection. Trends in Neurosciences 32, 9–18. https://doi.org/10.1016/j.tins.2008.09.012
Schulz, H., Übelacker, T., Keil, J., Müller, N., Weisz, N., 2014. Now I am Ready—Now I am not: The Influence of Pre-TMS Oscillations and Corticomuscular Coherence on Motor-Evoked Potentials. Cereb Cortex 24, 1708–1719. https://doi.org/10.1093/cercor/bht024
Seo, H., Jun, S.C., 2019. Relation between the electric field and activation of cortical neurons in transcranial electrical stimulation. Brain Stimulation 12, 275–289. https://doi.org/10.1016/j.brs.2018.11.004
Shirinpour, S., Alekseichuk, I., Mantell, K., Opitz, A., 2020a. Experimental evaluation of methods for real-time EEG phase-specific transcranial magnetic stimulation. J. Neural Eng. 17, 046002. https://doi.org/10.1088/1741-2552/ab9dba
Shirinpour, S., Alekseichuk, I., Mantell, K., Opitz, A., 2019. Experimental Evaluation of Methods for Real-Time EEG Phase-Specific Transcranial Magnetic Stimulation. bioRxiv 860874. https://doi.org/10.1101/860874
Shirinpour, S., Hananeia, N., Rosado, J., Galanis, C., Vlachos, A., Jedlicka, P., Queisser, G., Opitz, A., 2020b. Multi-scale Modeling Toolbox for Single Neuron and Subcellular Activity under (repetitive) Transcranial Magnetic Stimulation. bioRxiv 2020.09.23.310219. https://doi.org/10.1101/2020.09.23.310219

Shoop, R.D., Chang, K.T., Ellisman, M.H., Berg, D.K., 2001. Synaptically Driven Calcium Transients via Nicotinic Receptors on Somatic Spines. J. Neurosci. 21, 771–781. https://doi.org/10.1523/JNEUROSCI.21-03-00771.2001

Silvanto, J., Muggleton, N.G., 2008. New light through old windows: Moving beyond the “virtual lesion” approach to transcranial magnetic stimulation. NeuroImage 39, 549–552. https://doi.org/10.1016/j.neuroimage.2007.09.008

Sockeel, S., Schwartz, D., Pélégrini-Issac, M., Benali, H., 2016. Large-Scale Functional Networks Identified from Resting-State EEG Using Spatial ICA. PLOS ONE 11, e0146845. https://doi.org/10.1371/journal.pone.0146845

Stepniewski, M., Breit, M., Hoffer, M., Queisser, G., 2019. NeuroBox: computational mathematics in multiscale neuroscience. Comput. Visual Sci. 20, 111–124. https://doi.org/10.1007/s00791-019-00314-0

Stinear, C.M., 2017. Prediction of motor recovery after stroke: advances in biomarkers. The Lancet Neurology 16, 826–836. https://doi.org/10.1016/S1474-4422(17)30283-1

Stutzmann, G.E., Smith, I., Caccamo, A., Oddo, S., LaFerla, F.M., Parker, I., 2006. Enhanced Ryanodine Receptor Recruitment Contributes to Ca2+ Disruptions in Young, Adult, and Aged Alzheimer’s Disease Mice. J. Neurosci. 26, 5180–5189. https://doi.org/10.1523/JNEUROSCI.0739-06.2006

Tang, A., Thickbroom, G., Rodger, J., 2015. Repetitive Transcranial Magnetic Stimulation of the Brain: Mechanisms from Animal and Experimental Models. The Neuroscientist. https://doi.org/10.1177/1073858415618897

Thielscher, A., Kammer, T., 2004. Electric field properties of two commercial figure-8 coils in TMS: calculation of focality and efficiency. Clinical Neurophysiology 115, 1697–1708. https://doi.org/10.1016/j.clinph.2004.02.019

Thielscher, A., Kammer, T., 2002. Linking Physics with Physiology in TMS: A Sphere Field Model to Determine the Cortical Stimulation Site in TMS. NeuroImage 17, 1117–1130. https://doi.org/10.1006/nimg.2002.1282

Thielscher, A., Opitz, A., Windhoff, M., 2011. Impact of the gyral geometry on the electric field induced by transcranial magnetic stimulation. NeuroImage 54, 234–243. https://doi.org/10.1016/j.neuroimage.2010.07.061

Thut, G., Bergmann, T.O., Fröhlich, F., Soekadar, S.R., Brittain, J.-S., Valero-Cabré, A., Sack, A.T., Miniussi, C., Antal, A., Siebner, H.R., Ziemann, U., Herrmann, C.S., 2017. Guiding transcranial brain stimulation by EEG/MEG to interact with ongoing brain activity and associated functions: A position paper. Clinical Neurophysiology 128, 843–857. https://doi.org/10.1016/j.clinph.2017.01.003

Thut, G., Miniussi, C., Gross, J., 2012. The Functional Importance of Rhythmic Activity in the Brain. Current Biology 22, R658–R663. https://doi.org/10.1016/j.cub.2012.06.061

Tokay, T., Holl, N., Kirschstein, T., Zschorlich, V., Köhling, R., 2009. High-frequency magnetic stimulation induces long-term potentiation in rat hippocampal slices. Neuroscience Letters 461, 150–154. https://doi.org/10.1016/j.neulet.2009.06.032

Tremblay, S., Rogasch, N.C., Premoli, I., Blumberger, D.M., Casarotto, S., Chen, R., Di Lazzaro, V., Farzan, F., Ferrarelli, F., Fitzgerald, P.B., Hui, J., Ilmoniemi, R.J., Kimiskidis, V.K., Kugiumtzis, D., Lioumis, P., Pascual-Leone, A., Pellicciari, M.C., Rajji, T., Thut, G., Zomorrodi, R., Ziemann, U., Daskalakis, Z.J., 2019. Clinical utility and prospective of TMS–EEG. Clinical Neurophysiology 130, 802–844. https://doi.org/10.1016/j.clinph.2019.01.001

Valero-Cabré, A., Amengual, J.L., Stengel, C., Pascual-Leone, A., Coubard, O.A., 2017. Transcranial magnetic stimulation in basic and clinical neuroscience: A comprehensive review of fundamental principles and novel insights. Neuroscience & Biobehavioral Reviews 83, 381–404. https://doi.org/10.1016/j.neubiorev.2017.10.006

Vlachos, A., Müller-Dahlhaus, F., Rosskopp, J., Lenz, M., Ziemann, U., Deller, T., 2012. Repetitive Magnetic Stimulation Induces Functional and Structural Plasticity of Excitatory Postsynapses in Mouse Organotypic Hippocampal Slice Cultures. J. Neurosci. 32, 17514–17523. https://doi.org/10.1523/JNEUROSCI.0409-12.2012

Vogel, A., Reiter, S., Rupp, M., Nägel, A., Wittum, G., 2013. UG 4: A novel flexible software system for simulating PDE based models on high performance computers. Comput. Visual Sci. 16, 165–179. https://doi.org/10.1007/s00791-014-0232-9

Vöröslakos, M., Takeuchi, Y., Brinyiczki, K., Zombori, T., Oliva, A., Fernández-Ruiz, A., Kozák, G., Kincses, Z.T., Iványi, B., Buzsáki, G., Berényi, A., 2018. Direct effects of transcranial electric stimulation on brain circuits in rats and humans. Nature Communications 9, 483. https://doi.org/10.1038/s41467-018-02928-3

Wagner, T.A., Zahn, M., Grodzinsky, A.J., Pascual-Leone, A., 2004. Three-dimensional head model Simulation of transcranial magnetic stimulation. IEEE Transactions on Biomedical Engineering 51, 1586–1598. https://doi.org/10.1109/TBME.2004.827925

Wang, B., Grill, W.M., Peterchev, A.V., 2018. Coupling Magnetically Induced Electric Fields to Neurons: Longitudinal and Transverse Activation. Biophysical Journal 115, 95–107. https://doi.org/10.1016/j.bpj.2018.06.004

Weiping Wang, Eisenberg, S.R., 1994. A three-dimensional finite element method for computing magnetically induced currents in tissues. IEEE Transactions on Magnetics 30, 5015–5023. https://doi.org/10.1109/20.334289

Weissman, J.D., Epstein, C.M., Davey, K.R., 1992. Magnetic brain stimulation and brain size: relevance to animal studies. Electroencephalography and Clinical Neurophysiology/Evoked Potentials Section 85, 215–219. https://doi.org/10.1016/0168-5597(92)90135-X

Windhoff, M., Opitz, A., Thielscher, A., 2013. Electric field calculations in brain stimulation based on finite elements: An optimized processing pipeline for the generation and usage of accurate individual head models. Human Brain Mapping 34, 923–935. https://doi.org/10.1002/hbm.21479

Ziemann, U., 2017. Thirty years of transcranial magnetic stimulation: where do we stand? Exp Brain Res 235, 973–984. https://doi.org/10.1007/s00221-016-4865-4

Zrenner, B., Zrenner, C., Gordon, P.C., Belardinelli, P., McDermott, E.J., Soekadar, S.R., Fallgatter, A.J., Ziemann, U., Müller-Dahlhaus, F., 2019. Brain oscillation-synchronized stimulation of the left dorsolateral prefrontal cortex in depression using real-time EEG-triggered TMS. Brain Stimulation. https://doi.org/10.1016/j.brs.2019.10.007

Zrenner, C., Belardinelli, P., Müller-Dahlhaus, F., Ziemann, U., 2016. Closed-Loop Neuroscience and Non-Invasive Brain Stimulation: A Tale of Two Loops. Front. Cell. Neurosci. 10. https://doi.org/10.3389/fncel.2016.00092

Zrenner, C., Desideri, D., Belardinelli, P., Ziemann, U., 2018. Real-time EEG-defined excitability states determine efficacy of TMS-induced plasticity in human motor cortex. Brain Stimulation 11, 374–389. https://doi.org/10.1016/j.brs.2017.11.016

Zwanzger, P., Herrmann, M.J., Baeken, Ch., 2016. “Torpedo” for the brain: perspectives in neurostimulation. J Neural Transm 123, 1119–1120. https://doi.org/10.1007/s00702-016-1613-7

Appendix

Table A.1 Beta band performance and computation times in silico

Algorithm	Region	Mean (°)	SD (°)	Accuracy	Median Time (ms)
AR	All	0.04	85.75	0.61	0.69
	PFC	0.78	85.29	0.62	0.69
	M1	0.57	84.65	0.62	0.69
	OC	-1.23	87.30	0.60	0.69
ETP	All	0.81	79.84	0.65	0.08
	PFC	1.26	79.98	0.65	0.09
	M1	0.27	79.31	0.65	0.08
	OC	0.92	80.24	0.64	0.08
FFT	All	2.17	95.06	0.56	0.83
	PFC	3.51	95.64	0.55	0.83
	M1	2.82	94.02	0.56	0.83
	OC	0.16	95.53	0.55	0.83

Table A.2 Beta band performance metrics *in vivo*

Algorithm	Region	Mean (°)	SD (°)	Accuracy
AR	All	-0.17	89.36	0.59
	PFC	-4.18	87.82	0.60
	M1	-3.93	90.34	0.58
	OC	7.59	89.92	0.59
ETP	All	-2.17	78.51	0.65
	PFC	-6.03	77.22	0.67
	M1	-2.80	80.25	0.64
	OC	2.33	78.05	0.66
FFT	All	-5.09	93.70	0.55
	PFC	-3.22	91.47	0.58
	M1	-9.46	95.17	0.54
	OC	-2.58	94.46	0.55

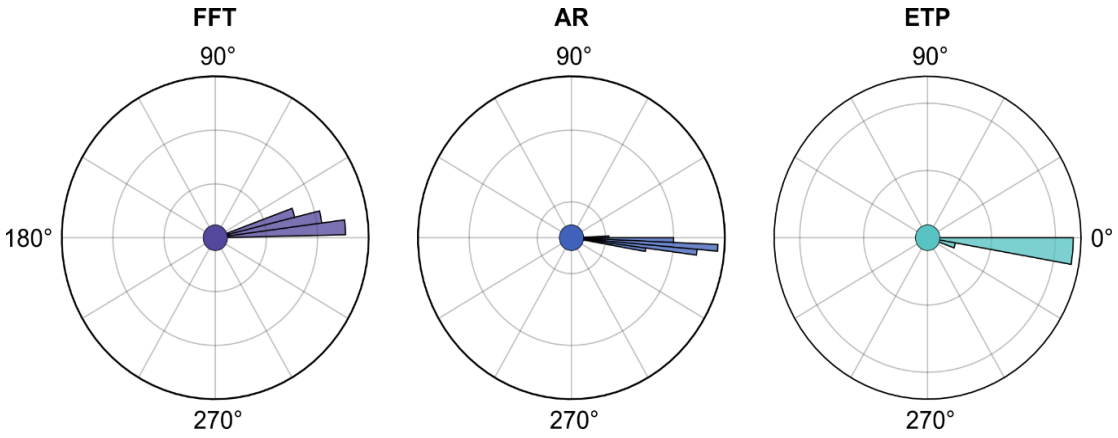

Figure A.1 System validation in the dummy head experiment.

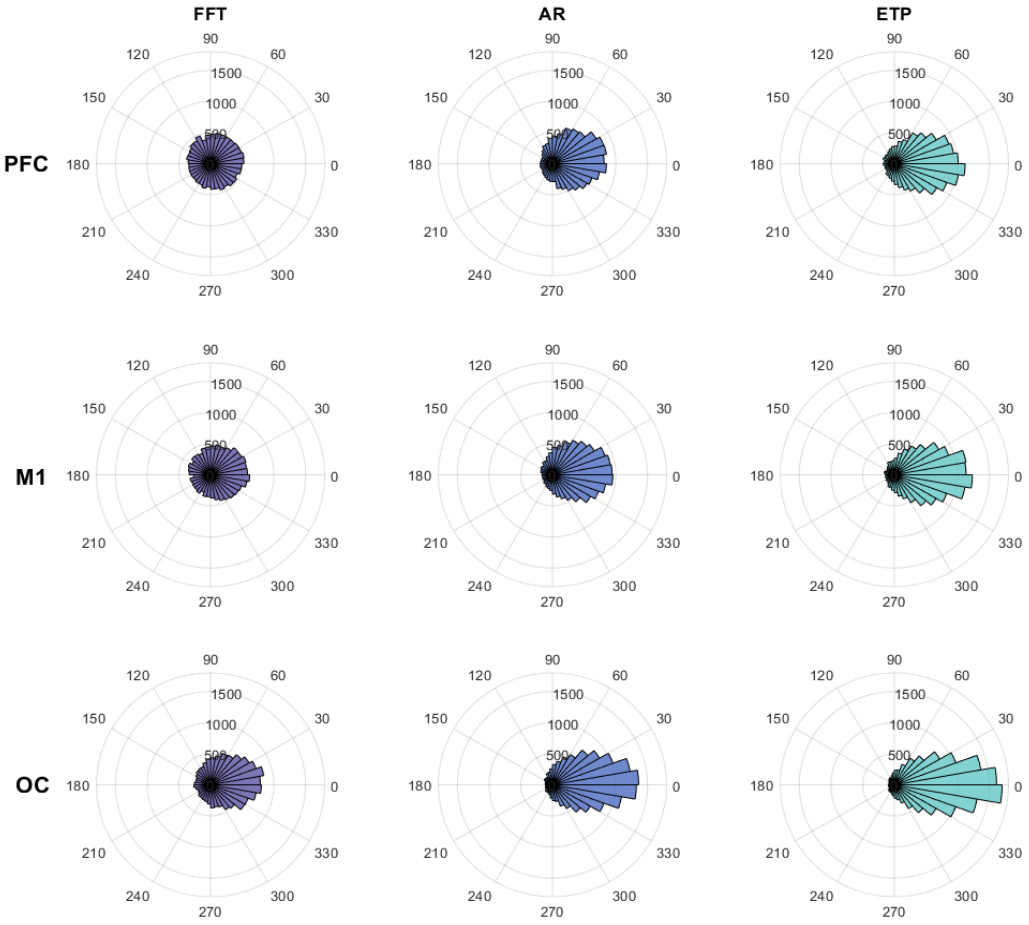

Figure A.2 Phase estimation results *in silico* for the alpha band across brain regions.

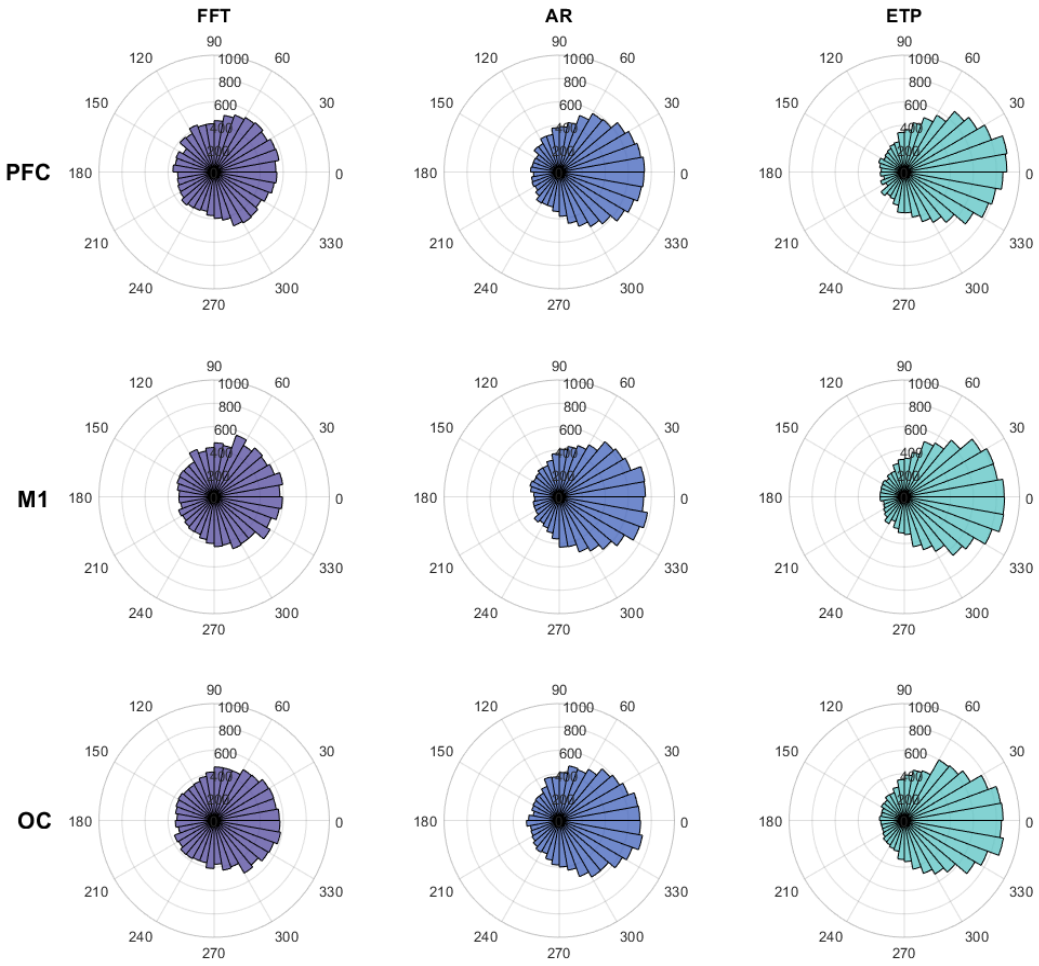

Figure A.3 Phase estimation results *in silico* for the beta band across brain regions.

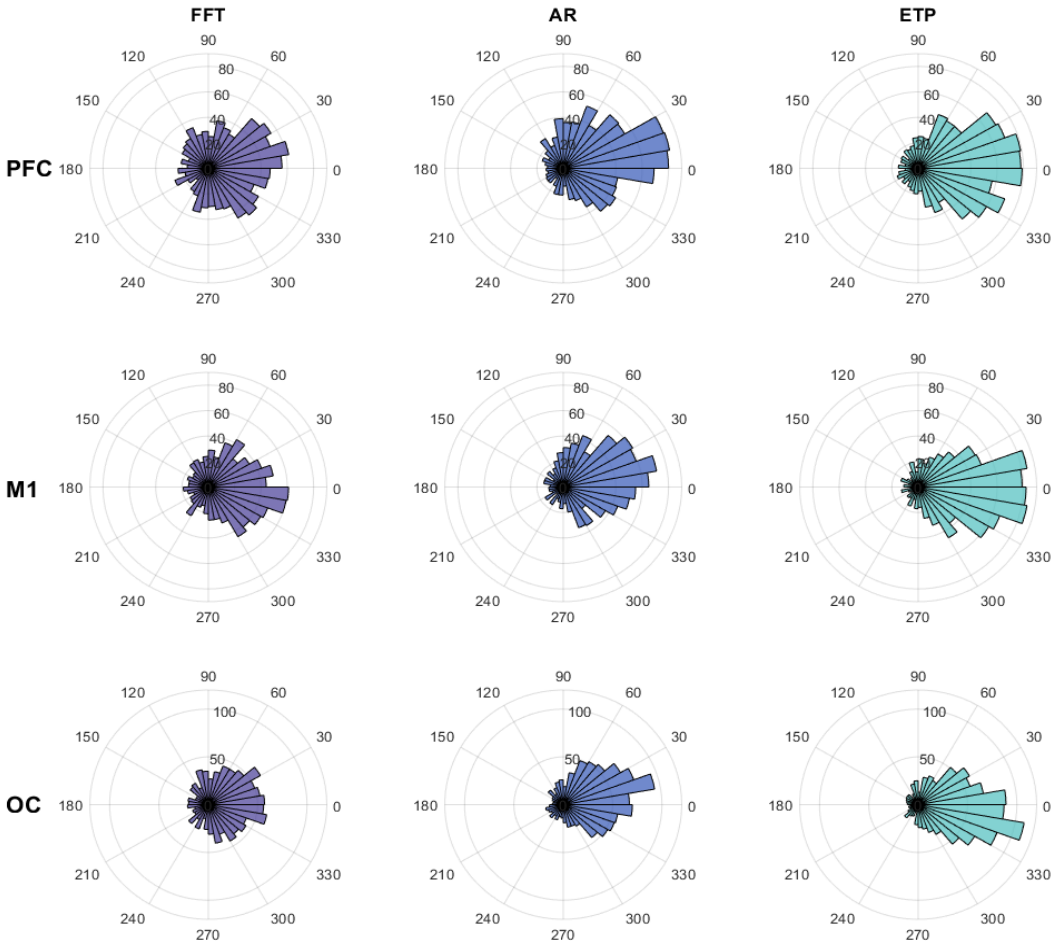

Figure A.4 Phase estimation results *in vivo* for the alpha band across brain regions.

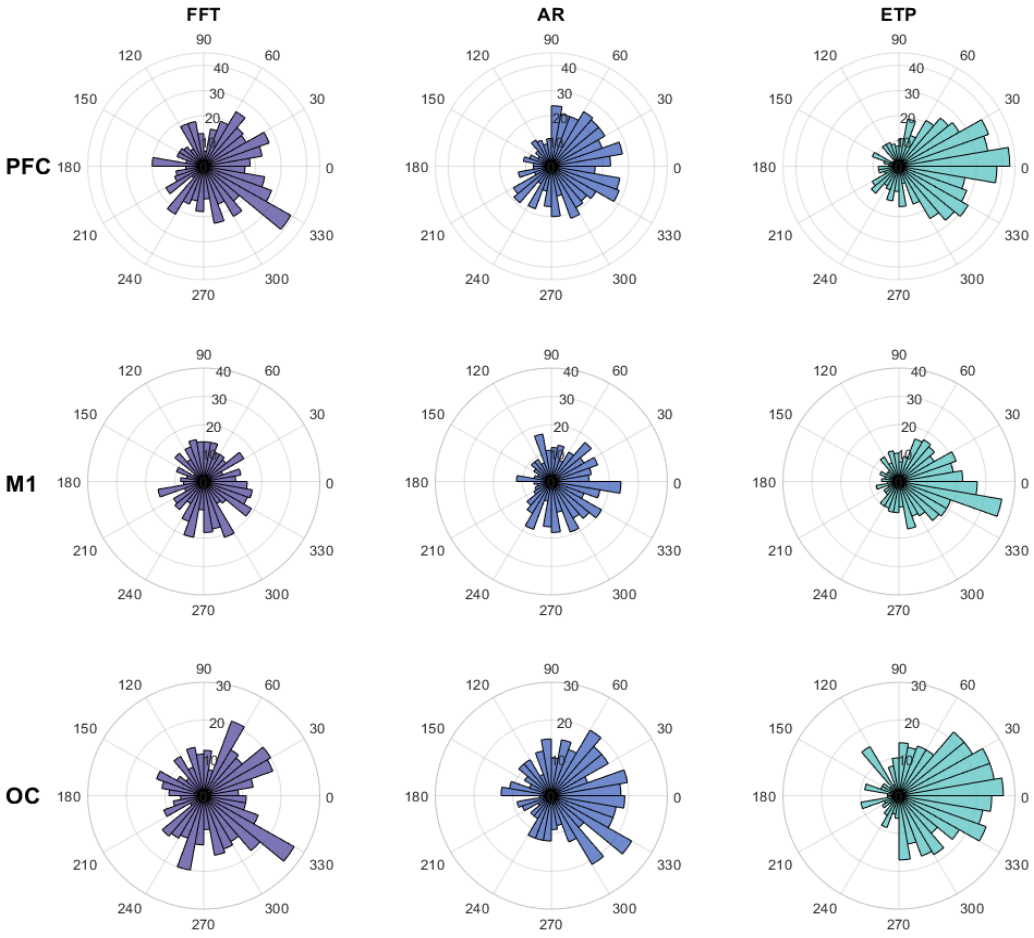

Figure A.5 Phase estimation results in vivo for the beta band across brain regions.